Defense Nuclear Agency
Alexandria, VA 22310-3398

DNA-TR-95-7

Evidence of Higher Pochhammer–Chree Propagation Modes in an Unsplit Hopkinson Bar

C. K. Binky Lee
Richard C. Crawford
Ken A. Mann
Logicon R/D Associates
P.O. Box 92500
Los Angeles, CA 90009

September 1996

Technical Report

DTIC QUALITY INSPECTED 3

19960910 112

DSWA

DISCLAIMER NOTICE
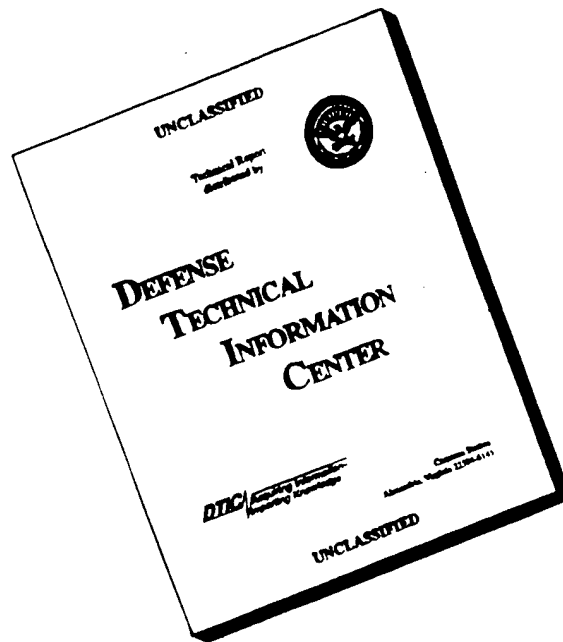
THIS DOCUMENT IS BEST QUALITY AVAILABLE. THE COPY FURNISHED TO DTIC CONTAINED A SIGNIFICANT NUMBER OF PAGES WHICH DO NOT REPRODUCE LEGIBLY.

DISTRIBUTION LIST UPDATE

This mailer is provided to enable DSWA to maintain current distribution lists for reports. (We would appreciate your providing the requested information.)

☐ Add the individual listed to your distribution list.

☐ Delete the cited organization/individual.

☐ Change of address.

NAME: _____

ORGANIZATION: _____

OLD ADDRESS	CURRENT ADDRESS
_____	_____
_____	_____
_____	_____

TELEPHONE NUMBER: (___) _____

DSWA PUBLICATION NUMBER/TITLE	CHANGES/DELETIONS/ADDITIONS, etc.)
	(Attach Sheet if more Space is Required)
_____	_____
_____	_____
_____	_____

DSWA OR OTHER GOVERNMENT CONTRACT NUMBER: _____

CERTIFICATION OF NEED-TO-KNOW BY GOVERNMENT SPONSOR (if other than DSWA):

SPONSORING ORGANIZATION: _____

CONTRACTING OFFICER OR REPRESENTATIVE: _____

SIGNATURE: _____

CUT HERE AND RETURN

DEFENSE SPECIAL WEAPONS AGENCY
ATTN: IMAS
6801 TELEGRAPH ROAD
ALEXANDRIA, VA   22310-3398

REPORT DOCUMENTATION PAGE	Form Approved OMB No. 0704-0188

1. AGENCY USE ONLY (Leave blank)	2. REPORT DATE 960901	3. REPORT TYPE AND DATES COVERED Technical 920601 – 940630

4. TITLE AND SUBTITLE
Evidence of Higher Pochhammer–Chree Propagation Modes in an Unsplit Hopkinson Bar

6. AUTHOR(S)
C. K. Binky Lee, Richard C. Crawford and Ken A. Mann

5. FUNDING NUMBERS
C - DNA 001-93-C-0138
PE - 62715H
PR - AB,CH
TA - KA, AA
WU - DH310900

7. PERFORMING ORGANIZATION NAME(S) AND ADDRESS(ES)
Logicon R/D Associates
P.O. Box 92500
Los Angeles, CA 90009

8. PERFORMING ORGANIZATION REPORT NUMBER
TR-211-4240-1703-001

9. SPONSORING/MONITORING AGENCY NAME(S) AND ADDRESS(ES)
Defense Special Weapons Agency
6801 Telegraph Road
Alexandria, VA 22310-3398
TDTR/Flohr

10. SPONSORING/MONITORING AGENCY REPORT NUMBER
DNA-TR-95-7

11. SUPPLEMENTARY NOTES
This work was sponsored by the Defense Special Weapons Agency under RDT&E RMC Code B4662D AB KA EA011 1110A 25904D and B1340D CH AA 32109 1110A 25904D.

12a. DISTRIBUTION/AVAILABILITY STATEMENT

Approved for public release; distribution is unlimited.

12b. DISTRIBUTION CODE

13. ABSTRACT (Maximum 200 words)
A discovery is made in the propagation modes of stress waves in a Hopkinson bar. Signatures of the first three modes of propagation, given by the Pochhammer–Chree solution a century ago, are derived from a set of recent experiments. The data suggests that at frequencies where multiple theoretical modes are possible, the mode with the faster group velocity dominates the propagation. The Gaussian Windowed Fourier Transform technique is used to obtain time-dependent Fourier coefficients from a measured signal. The transformed signal is displayed in a gray scale plot of the power spectra of the Fourier coefficients as a function of time and frequency. These plots show clear evidence of the theoretical modes, which have never been conclusively observed from measured data prior to this work. A new dispersion curve for stress wave propagation in bars is proposed based on the above results. The new dispersion curve, used in DISBAS code (A bar gage deconvolution technique that uses dispersed basis functions), gives a highly resolved stress wave; in particular, it reveals the detailed structure of the peak, which in this case consists of several 'peaklets'. These peaklets depict the distortions of the stress wave introduced by the water jacket and the mounting structure for the bar. The proposed dispersion relation, in conjunction with the DISBAS code, can be used to distinguish differences in the measured stress wave structure due to water jackets and mounting devices. Such differences are not discernible by previous deconvolution techniques due to inherent inaccuracies in those techniques as well as the lack of an accurately measured dispersion relation.

14. SUBJECT TERMS
Airblast
Bar Gage
Water-Jacket   Pochhammer-Chree Solution

15. NUMBER OF PAGES
76

16. PRICE CODE

17. SECURITY CLASSIFICATION OF REPORT UNCLASSIFIED	18. SECURITY CLASSIFICATION OF THIS PAGE UNCLASSIFIED	19. SECURITY CLASSIFICATION OF ABSTRACT UNCLASSIFIED	20. LIMITATION OF ABSTRACT SAR

i

CLASSIFIED BY:

N/A since Unclassified.

DECLASSIFY ON:

N/A since Unclassified.

SUMMARY

A discovery is made in the propagation modes of stress waves in a Hopkinson bar. Signatures of the first three modes of propagation, given by the Pochhammer-Chree solution a century ago, are derived from a set of recent experiments. The data suggest that at frequencies where multiple theoretical modes are possible, the mode with the faster group velocity dominates the propagation. The Gaussian Windowed Fourier Transform technique is used to obtain time-dependent Fourier coefficients from a measured signal. The transformed signal is displayed in a gray scale plot of the power spectra of the Fourier coefficients as a function of time and frequency. These plots show clear evidence of the theoretical modes, which have never been conclusively observed from measured data prior to this work. A new dispersion curve for stress wave propagation in bars is proposed based on the above results. The new dispersion curve, used in the DISBAS code (a bar gage deconvolution technique that uses dispersed basis functions), gives a highly resolved stress wave; in particular, it reveals the detailed structure of the peak, which in this case consists of several 'peaklets'. These peaklets depict the distortions of the stress wave introduced by the water jacket and the mounting structure for the bar. The proposed dispersion relation, in conjunction with the DISBAS code, can be used to distinguish differences in the measured stress wave structure due to water jackets and mounting devices. Such differences are not discernable by previous deconvolution techniques due to inherent inaccuracies in those techniques as well as the lack of an accurately measured dispersion relation.

PREFACE

TABLE OF CONTENTS

FIGURES

FIGURES(Continued)

SECTION 1

INTRODUCTION

For decades the Hopkinson pressure bar has been used for measurements of blast and shock waves generated by explosions. It is a very useful instrument for close-in blast measurements because it is difficult for other instruments to survive both the blast loading and the environment near the center of the explosion. Despite its popularity in the explosion community, basic experimental studies of the dispersion of waves in the bar are rare. Technically there are two reasons for the lack of incentive to pursue the dispersive characteristics of a bar. First, an accurate method for determining a dispersion curve (the phase or group velocity as a function of frequency) from a signal captured in the form of a time sequence is not available. Second, several theoretical investigations in the past century have concluded that the basic mode of propagation is the first Pochhammer-Chree (PC) mode (Pochhammer, 1876, and Chree, 1889). Moreover, because these theoretical investigations were performed by scientific authorities such as Rayleigh and Timoshenko (see for example Kolsky, 1963), it is very difficult for anyone to cast doubt on this result. Although some indirect evidence of higher modes has been reported (Curtis, 1954), the first PC mode is still the most commonly used dispersion curve for the deconvolution of bar signals. In this report, we will present a mathematical technique that derives the dispersion curve from a measured signal (Section 2). Section 3 presents experimental data in the form of time sequences and the dispersion curves derived from them. These dispersion curves will show that the first PC mode is not the only mode of propagation for stress waves in water-jacketed bars. Section 4 shows the the deconvolved signals from the DISBAS code (Lee and Crawford, 1992 and 1993) that uses the derived dispersion curves.

SECTION 2

METHOD OF ANALYSIS

In an earlier effort, we developed a rectangular-windowed Fourier series (RWFS) method (Lee and Crawford, 1993) to deconvolve dispersed stress or strain signals measured some distance away from the pressure end of a bar which is directly exposed to the blast from an explosion. We introduced the rectangular window to correctly account for the differences in times of arrival of the various frequency components in the blast. The resulting RWFS method accounts for both times of arrival as well as phase shifts of the various frequencies. This was demonstrated to be a more accurate deconvolution technique than the classical Gorham method (Gorham, 1983) which accounts for phase shifts only. Aside from the accuracy, RWFS can identify nondispersive components in the signal. This is a distinct advantage because most signals measured in field tests are 'corrupted' to various degrees by electrical noise or other nondispersive effects. An example was reported in Reference 4, in which RWFS gave a warning of possible nondispersive components in the data. We identified these nondispersive components by dividing the signal into small time segments and calculating the local Fourier coefficients in each segment.

Any segment can be viewed as the product of the signal and a rectangular window, and the Fourier coefficients of the segment can be calculated using RWFS. For a measured signal given as a time sequence, $\phi(t)$, of duration P, we can approximate the signal by

$$\phi(t) = W(t)\sum_{k=1} a_k \sin\omega_k t \qquad (2.1)$$

where $\omega_k = k\pi/P$, (Lee and Crawford, 1992), and the rectangular window function is given by

$$W(t) = \frac{1}{2J} + \sum_{n=1} \frac{1}{n\pi}\left[\sin\left(\frac{n\pi(T-t)}{JT}\right) + \sin\left(\frac{n\pi t}{JT}\right)\right] \qquad (2.2)$$

which is the Fourier expansion of a periodic rectangular window that is unity for the period T and zero for the period $(2J-1)T$. For this discussion, we will omit discussions of the time of arrival and the phase shift, which are given in References 4 and 5. We will concentrate on the window itself.

Suppose we choose a narrow window width $T \ll P$, and move this narrow window to t^*. We then compute the a_k in this interval by convolving $\phi(t)$ with each component of the series in Equation 2.1. The power spectrum obtained from the squares of the a_k gives the local frequency spectrum of the signal $\phi(t)$ at t^*, modified by the window function. In this way, every interval T in P contains a set of coefficients a_k that describes the frequency contents of that interval. If the signal is dispersive, the spectrum at each time interval will change according to the dispersion. In particular, the power associated with a given frequency component will peak at the time of arrival of that component. In other words, the locus of the times of arrival of these power peaks plotted in frequency-time space delineates the group

2

velocities of the frequency components in the signal. The difficulty with the rectangular window is that the amplitudes of the high frequency components of $\phi(t)$ in the interval t^* and $t^* + T$ are modified by those produced by the rectangular window.

For this work we used the Gaussian window, which has the advantage of being localized in both the time and frequency domains. Other window functions have been proposed (Daubechies, 1986 and 1990) in the context of wavelet transforms. In the present Gaussian window Fourier transform (GWFT), we compute the discrete transform of the product of the signal $\phi(t)$, and the translated Gaussian function $g(t-\tau)$ centered at the time τ, by the discrete version of

$$C(\omega,\tau) = \int_{-\infty}^{\infty} \phi(t)g(t-\tau)\exp(-i\omega t)\,dt \qquad (2.3)$$

which is, after noting that the signal $\phi(t)$ is zero for $t < 0$,

$$C_{mn} = \int_{0}^{\infty} \phi(t)g(t-n\Delta t)\exp(-im\omega_o t)\,dt \qquad (2.4)$$

where ω_o is the discretized frequency increment, and Δt is the time increment, which gives the information in Equation 2.3 in a uniformly spaced lattice. These coefficients are complex in general, and instead of displaying their real and imaginary parts, we display the power. Note that $C(\omega,\tau)$ is a continuous function of two variables and C_{mn} is a coefficient defined on a lattice. The window function in the present case is a Gaussian,

$$g(\tau) = \frac{1}{\sigma\sqrt{2\pi}}\exp\left(-\frac{1}{2}\left(\frac{\tau}{\sigma}\right)^2\right) \qquad (2.5)$$

where σ is the window width parameter. Equation 2.4 is solved by taking the Fast Fourier Transform (FFT) of the product $\phi(t) * g(t-n\Delta t)$ which is equivalent to choosing ω_o to be the fundamental frequency in the signal $\phi(t)$, and allowing the highest frequency to be the Nyquist frequency. The optimum window size is determined numerically. See Appendix A.

In order to test the method, we create a synthetic signal that has a linear rise time of 1 μs, and an exponential decay after the peak with a decay constant of 5 μs. The synthetic signal is dispersed three feet down a half inch diameter steel bar using the first PC mode. The dispersed signal from this pulse is analyzed by GWFT. The dispersion curve obtained by the method presented below agrees exactly with the first PC mode. This suggests that the GWFT technique can be used to derive dispersion curves from signals that are dispersive.

3

SECTION 3

DERIVATION OF A MEASURED DISPERSION CURVE

We apply the GWFT to a set of 1/8-inch diameter steel bar data. This set of data is collected from an explosion in a steel water tank 16 inches in diameter (Coleman and Petersen, 1993). The pressure end of the bar is connected to the tank wall at the level of the HE charge. The bottom of the tank and the water free surface are at least 8 inches away from the HE charge. The signal is collected by a strain gage attached to the bar three feet away from the pressure end, which is flush mounted to the tank. The sampling time interval is 0.1 microsecond, which is short enough to ensure that high frequency details are captured by the data acquisition system. The digitizer full scale is 4096:1 (12 bits). The resolution is at least 500 steps for the maximum voltage change.

A typical result of a pressure signal processed by GWFT is shown in Figure 3-1 in the form of a gray scale plot. The measured signal is shown vertically on the right hand side of the gray scale in Figure 3-2. The gray scale plot (a plot that divides black and white into various levels of gray to represent the magnitude of a quantity) represents the power of the C_{mn}. Note that we have chosen the convention that darker represents more power. Clearly, the power associated with the low frequency components is much higher than that with the high frequencies. In order to extract the dispersive properties of the bar, we have to concentrate on the times of arrival (ToAs) of the various frequencies, i.e., the arrival of the power associated with these frequencies. In the low frequency range ($\omega < \pi/4$ Mrad/s) the power, represented by the darkened region, arrives at approximately the same time independent of frequency. See the upper left corner of Figure 3-1. From this we conclude that there is no measurable dispersion in this low frequency range; the GWFT is simply reproducing the low frequency information in the incident shock at the pressure end of the bar. Notice that this entire nondispersive region is darker than the higher frequency region of the plot, i.e., most of the power is carried by the low frequencies. There are also white (light gray) spots embedded in the gray scale plot. These are very low power locations where the C_{mn} change sign. Some interesting gray scale plots of the C_{mn} are presented in Appendix C. Because of the nondispersive nature of the low frequency region, deconvolution will not 'reorganize' the gray pattern in this region.

The ToAs we derive in the low frequency region depend on the window width. For the present computation, a 10-µs window is used; its width is determined by performing a set of detailed numerical experiments (see Appendix A). The width of the Gaussian window is varied from 2 µs to 15 µs. In general, widening the window will sharpen the dark band in the frequency direction but cause more smearing in the time, and vice versa. The 10 µs window is considered a good compromise.

In the higher frequency range, $\omega > \pi/4$ Mrad/s, Figure 3-1 shows a high power region in the form of a dark band that curves toward the lower right of the figure. The level of light gray in the region above the dark band shows very little power arriving ahead of the band. This is evidence of dispersive behavior. The fact that there is very little power between the low frequency

4

nondispersive region and the dark band suggests that the incident signal carried most of the high frequency components in the front of the pulse. This in turn suggests that the incident signal at the pressure end of the bar is a shock because the usual compression waves do not carry high frequency components right at the wavefront. This is in agreement with our expectation that the explosion in the tank generates a water shock that impacts the pressure end of the bar.

At this point we compare the arrivals of the theoretical dispersion modes of Pochhammer and Chree with the measured ToAs of peak power. We convert the first PC mode for this 1/8-inch steel bar to a ToA curve and plot it as a solid line on the gray scale plot, as shown in Figure 3-2. Clearly, the dark band (the high power region) in Figure 3-2 agrees with the theoretical arrivals very well. In the low frequency range, the first PC mode shows a small dispersive effect. Considering the thickness of the dark band in the upper left corner of Figure 3-1, it is difficult to discern this small an amount of dispersion from the experimental data. From Equation 2.3, it is clear that even if the function $\phi(t)$ begins with a sharp rise, the Gaussian window will smear it. From the agreement between the dark band in the gray scale plot and the ToAs of the first PC mode, we conclude that the experimental dispersion curve derived from this water-jacketed 1/8-inch steel bar validate the theoretical first PC mode.

Next, we process a signal from a 1/2-inch bar in the same set of experiments. The difference between the 1/2-inch and the 1/8-inch bar is that for the same frequency range, the group velocity curve for the 1/2-inch bar extends far beyond the minimum of the first PC mode. This allows us to examine the dispersive behavior of the bar in regions where higher modes may exist. Figure 3-3 shows the GWFT gray scale plot, and Figure 3-4 shows the measured signal plotted on the gray scale. Again, as in Figure 3-1, we observe that there is a region ($\omega < \pi/4$ Mrad/s) where very little dispersion is shown. The interesting point about this plot is the existence of multiple peaks and valleys in the dark band at frequencies higher than $\pi/2$ Mrad/s. Near the first minimum, $\sim\pi/2$ Mrad/s, the dark band contains several abrupt jumps. At the second minimum, $\sim1.1\pi$ Mrad/s, there is a distinct change in slope in the dark band. These features are a combination of the spectral character of the incident shock and the dispersive character of the bar. Because we know from the 1/8-inch bar signal that the incident signal is a shock, the high frequencies are expected to impact the bar at ToA, and then propagate down the bar according to the dispersive character of the bar.

The abrupt jumps near the first minimum cannot be a characteristic of the dispersion in the bar. Mathematically, such behavior in the group velocity causes the hyperbolic system of equations to be ill-posed because, at the jumps, the characteristic velocity of propagation for that frequency component is multi-valued and can vary continuously over the full range of the jump. Physically this type of jump in the group velocity is not acceptable, either, because a wave at that frequency will have a group velocity that varies between the limits of the jump as it propagates down the bar. The acceptable explanation is that the jumps are results of the incident signal. The incident signal may not have all the high frequencies right at ToA; for example a pulse with multiple peaks may have the high frequencies delivered at slightly different times. The halfwidth of this pulse is ~ 25 μs, so structure within the pulse may lead to features of that duration in the gray scale plot. When these frequencies are dispersed down the bar, they may superpose to form the

observed jumps in the dark band.

These jumps occur at a very steep part of the dark band, where arrivals of slightly different frequencies occur at distinctly different times. After smearing by the Gaussian window, these will form a vertical band that may resemble an abrupt jump. If this occurs at a mildly sloped part of the dark band, it will simply thicken the band. Because the mildly sloped region of the dark band is essentially nondispersive, the arrival of the same frequency at different times will simply be interpreted as characteristic of the **incident** signal. Clearly, the present GWFT technique is not sufficiently accurate to resolve the very steep portions of the dispersion curve because of the smearing by the window.

On the other hand, the sudden change in slopes of the dark band at the valleys is mathematically and physically acceptable. This behavior suggests multimode propagation because, in general, for a single mode the slope of the group velocity changes smoothly with frequency. Mathematically, the hyperbolic problem should be separated into regions, each region governed by a well-behaved function for the group velocity. A simple way to explain the observed slope changes is that the dark band is a superposition of several modes governing wave propagation in this bar. This is a natural consequence of the set of nonunique solutions, from a mathematical point of view (see Whitham, 1974). Because the set of theoretical modes governing wave propagation in this bar is known, it is logical to try to match the observed modes by linear combinations of the theoretical Pochhammer-Chree modes.

Figure 3-5 shows a plot of the first four PC modes in both phase and group velocities. The roughness in the group velocity curves is the result of taking numerical derivatives of the theoretical phase velocity curves. Because the group velocity is the physical quantity directly derivable from the measured signal, we will concentrate on the group velocity curves. We observe that as the scaled frequency increases, more and more modes can potentially be involved in the propagation. Conventional bar gage deconvolution methods simply use the first PC mode to avoid the complexity introduced by the higher modes. The results shown in Figure 3-3, however, suggest simply using the first mode is inadequate for this 1/2-inch bar signal. The group velocity curves are converted to a set of ToA curves as shown in Figure 3-6. Figure 3-7 shows the overlay of these modes on the gray scale plot. We observe that away from the valleys, the curvature of the first three modes matches the dark band almost exactly. In the high frequency region where multiple arrival from various modes is possible, the gray scale shows high power (darkened band) only for the earliest arriving mode. There is little power associated with the later arriving modes. This suggests that we can combine these modes using one single criterion, namely, that the mode with the faster group velocity dominates the propagation. The resulting ToA curve will be single-valued. Thus we are led to eliminate the late-arriving modes from this curve and overlay the resulting single-valued curve onto the gray scale plot of Figure 3-3, as shown in Figure 3-8. The agreement between this theoretical combined-mode curve and the dark band is very good except near the first minimum of the first mode. This is strong evidence of the first three PC modes in the signal.

In the interest of determining an experimental dispersion curve for the 1/2-inch steel bar, which

is a commonly used bar material and size, we selected the time of peak power at each frequency. This defines a curve that lies in the middle the dark band. The ToAs of the high frequency components can be well approximated by the time of peak power. At frequencies below $\pi/4$ Mrad/s, the time of peak power is not a good approximation for the ToA. At these low frequencies, an adjustment to the time of peak power is applied for each frequency to establish the dispersion curve (see Appendix B). The resulting group velocity, computed from $C_g(\omega)=D/T(\omega)$, where $T(\omega)$ is the ToA for the frequency ω, together with the theoretical combined-mode curve, is shown in Figure 3-9. The jumps in the dark band in Figure 3-3 are obvious in the measured group velocity. Even though we understand that these jumps cannot be a part of the group velocity, we include them because leaving them out would lead to some undefined regions in the group velocity curve which would make calculation of the phase velocity impossible.

To derive the corresponding phase velocity curve, which is needed as an input to the DISBAS code, recall the phase velocity C_p, and the group velocity C_g, are related by (Kolsky, 1963)

$$C_g(\omega) \;=\; C_p(\omega) \;-\; \lambda\, \frac{dC_p(\omega)}{d\lambda} \tag{3.1}$$

where the wavelength, λ, is related to the frequency by $\lambda = C_p/\omega$. The inverse of the group velocity definition is

$$C_p(\omega) \;=\; \lambda \int_\lambda^\infty \frac{C_g(\omega)}{l^2}\, dl \tag{3.2}$$

which must be solved iteratively because of the implicit presence of C_p in the integrand (through ω). An iterative solution starting with $C_p(0) = C_0$ and using $C_p(\omega-\Delta\omega)$ as the first approximation of $C_p(\omega)$ is adequate. For the present three-mode problem, we break down the integral in Equation 3.2 into three integrals as follows.

$$C_p(\omega) \;=\; \begin{cases} \lambda \displaystyle\int_\lambda^\infty \frac{C_g(\omega)}{l^2}\, dl & \text{for } \lambda_1 \leq \lambda < \infty \\[2ex] \lambda \displaystyle\int_\lambda^{\lambda_1} \frac{C_g(\omega)}{l^2}\, dl + C_2 & \text{for } \lambda_2 \leq \lambda \leq \lambda_1 \\[2ex] \lambda \displaystyle\int_\lambda^{\lambda_2} \frac{C_g(\omega)}{l^2}\, dl + C_3 & \text{for } \lambda_3 \leq \lambda \leq \lambda_2 \end{cases} \tag{3.3}$$

We choose to shift from one mode to the next mode at the frequencies where the theoretical group velocity curves from the consecutive modes cross, and at those frequencies we use the theoretical phase velocity to restart the integration of the observed group velocity curve. The

7

numerical values are $\lambda_1 = 0.0237$ m, $\lambda_2 = 0.01304$ m, $\lambda_3 = 0.008227$ m, $C_2 = 7166.46$ m/s, $C_3 = 7027.46$ m/s, and $C_0 = 5285.00$ m/s for this bar. The resulting phase and group velocity curves derived from the measured signal through the use of the GWFT are shown in Figure 3-9, which contains also the theoretical combined-mode curves. The exact location of the first transition cannot be defined by the data due to the abrupt jumps. On the other hand, the assumption that the propagation is dominated by the fastest mode defines exactly the locations of these transitions. Because we used the theoretically defined transition points to derive the phase velocity curve, this curve should be considered semi-empirical as opposed to the measured group velocity curve, which is based solely on experimental data.

The error associated with the experimentally determined ToA is probably comparable to the size of the Gaussian window. A rigorous analysis of how this error is propagated into the phase velocity would be extremely difficult due to the systematic nature of several other contributing uncertainties. We perform a Monte Carlo simulation of the error, presented in Appendix B. The results, which although not rigorous should be of the correct order, are shown on Figure 3-10.
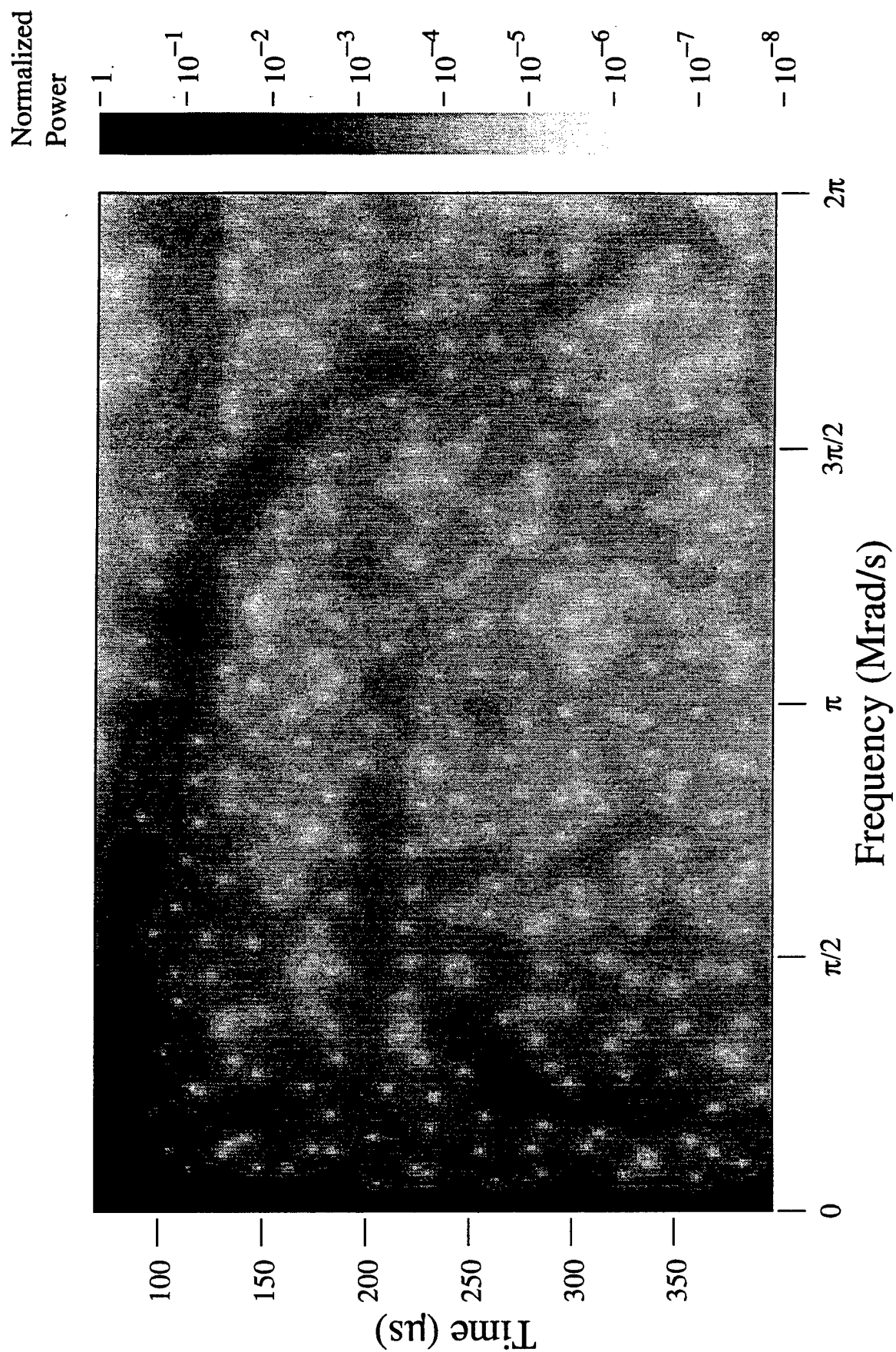
Figure 3-1. Water tank 1/8-inch bar signal WT2BAR3.C3 processed by GWFT with a 10-μs Gaussian window.
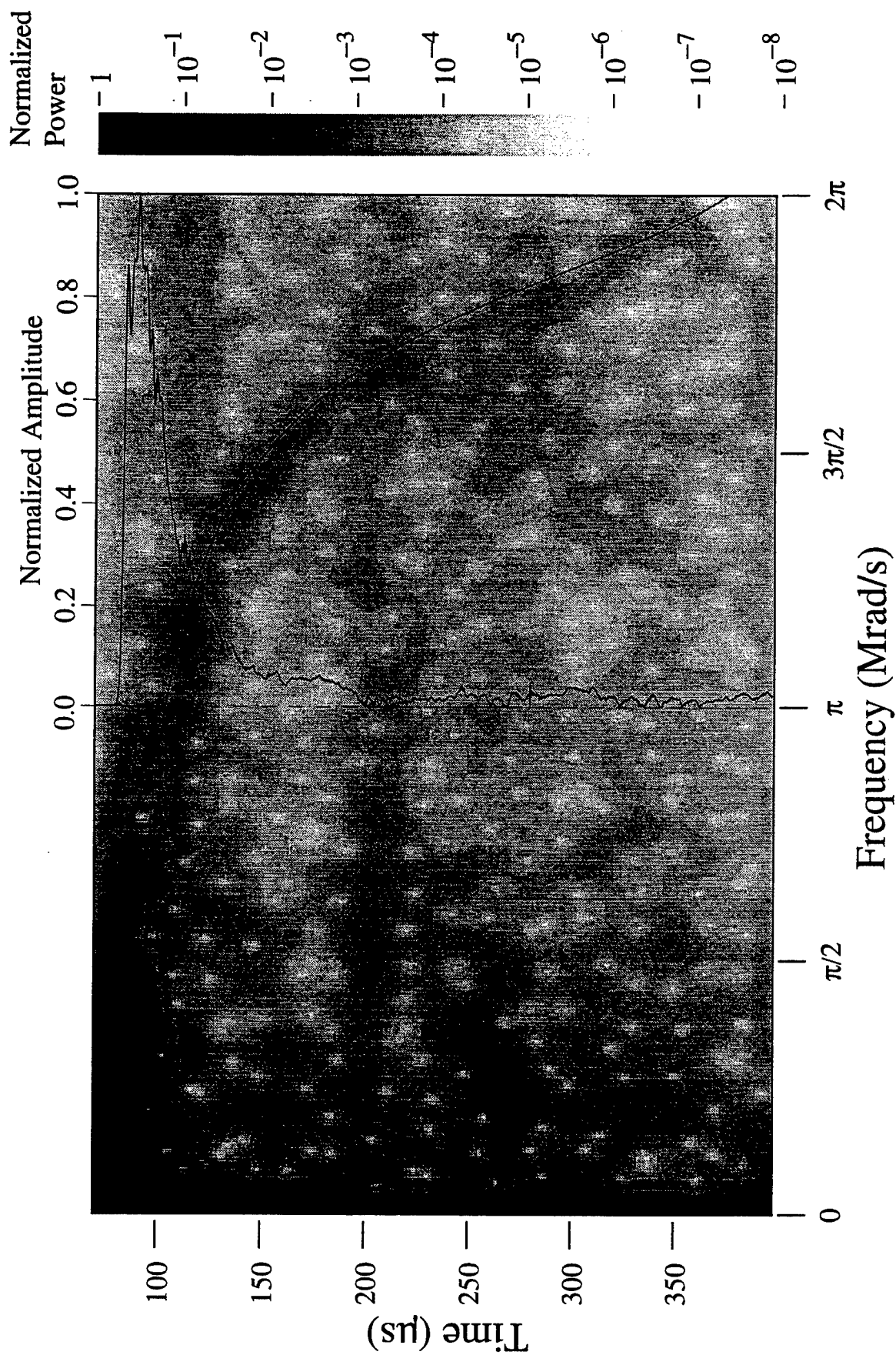
Figure 3-2. 1/8-inch bar signal: the ToAs from the first PC mode plotted on Figure 3-1.

10
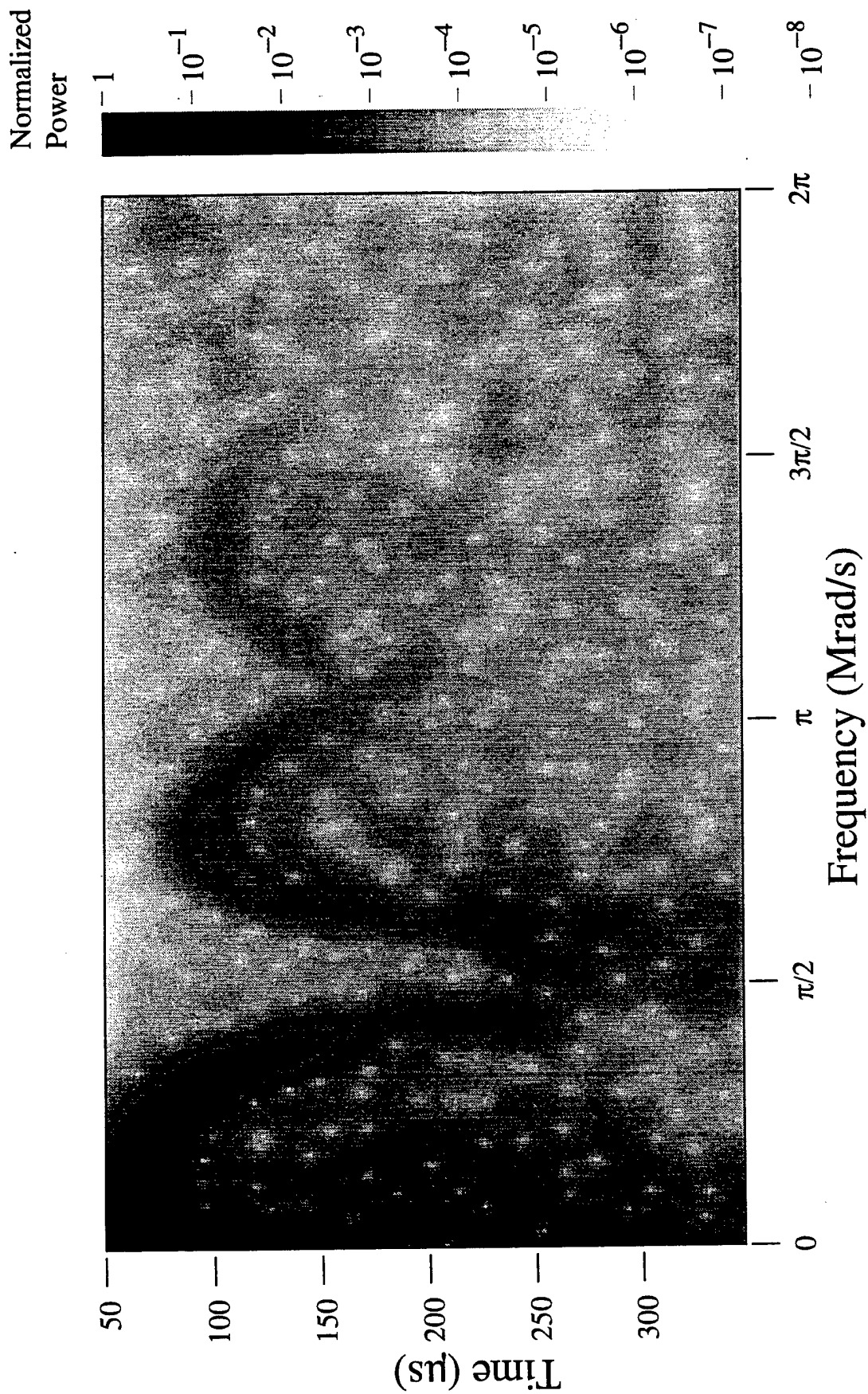
Figure 3-3.   Water tank 1/2-inch bar signal WT2BAR2a processed by GWFT with a 10-μs Gaussian window.
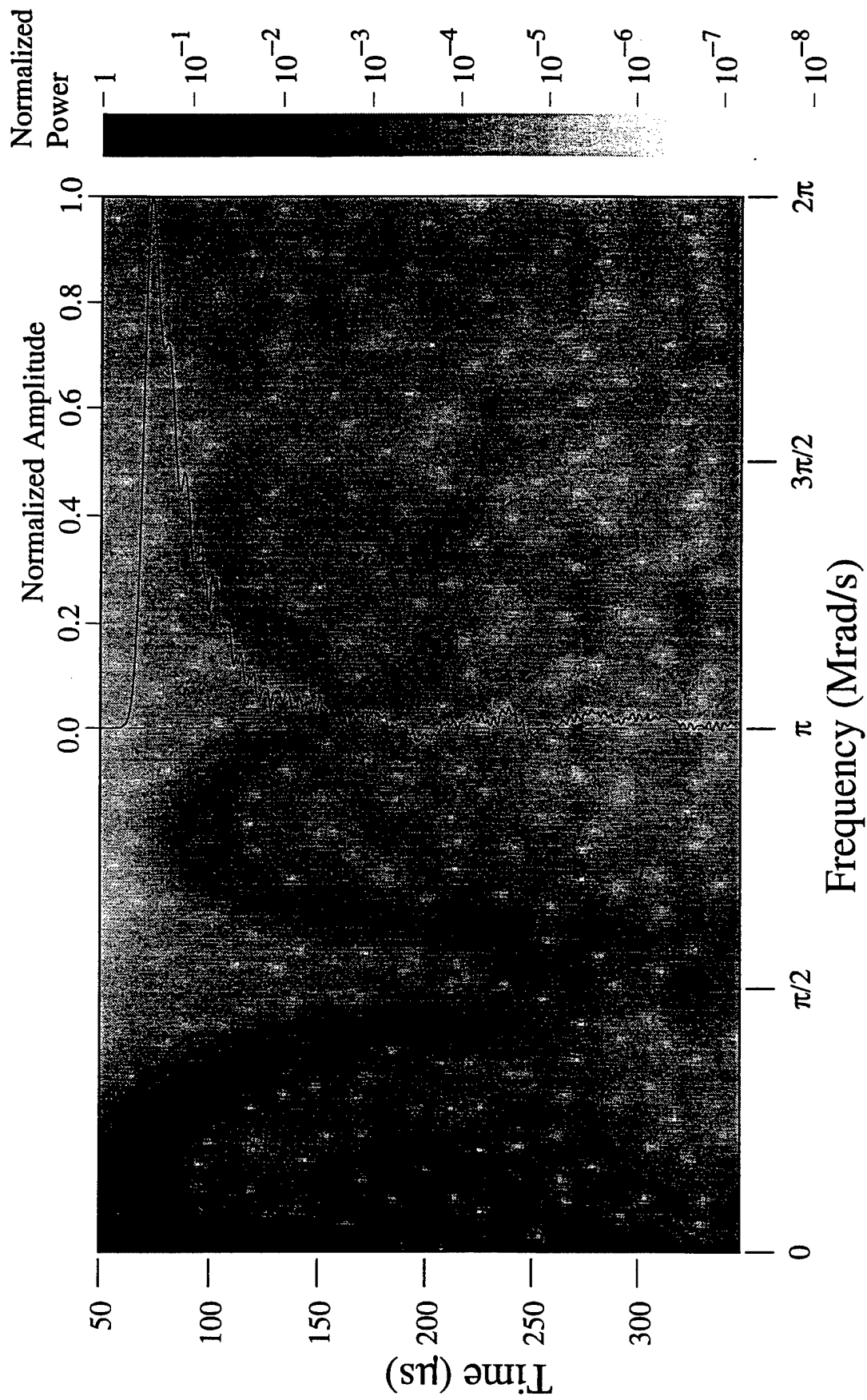
Figure 3-4.   1/2-inch bar record: raw signal and gray scale image.

12
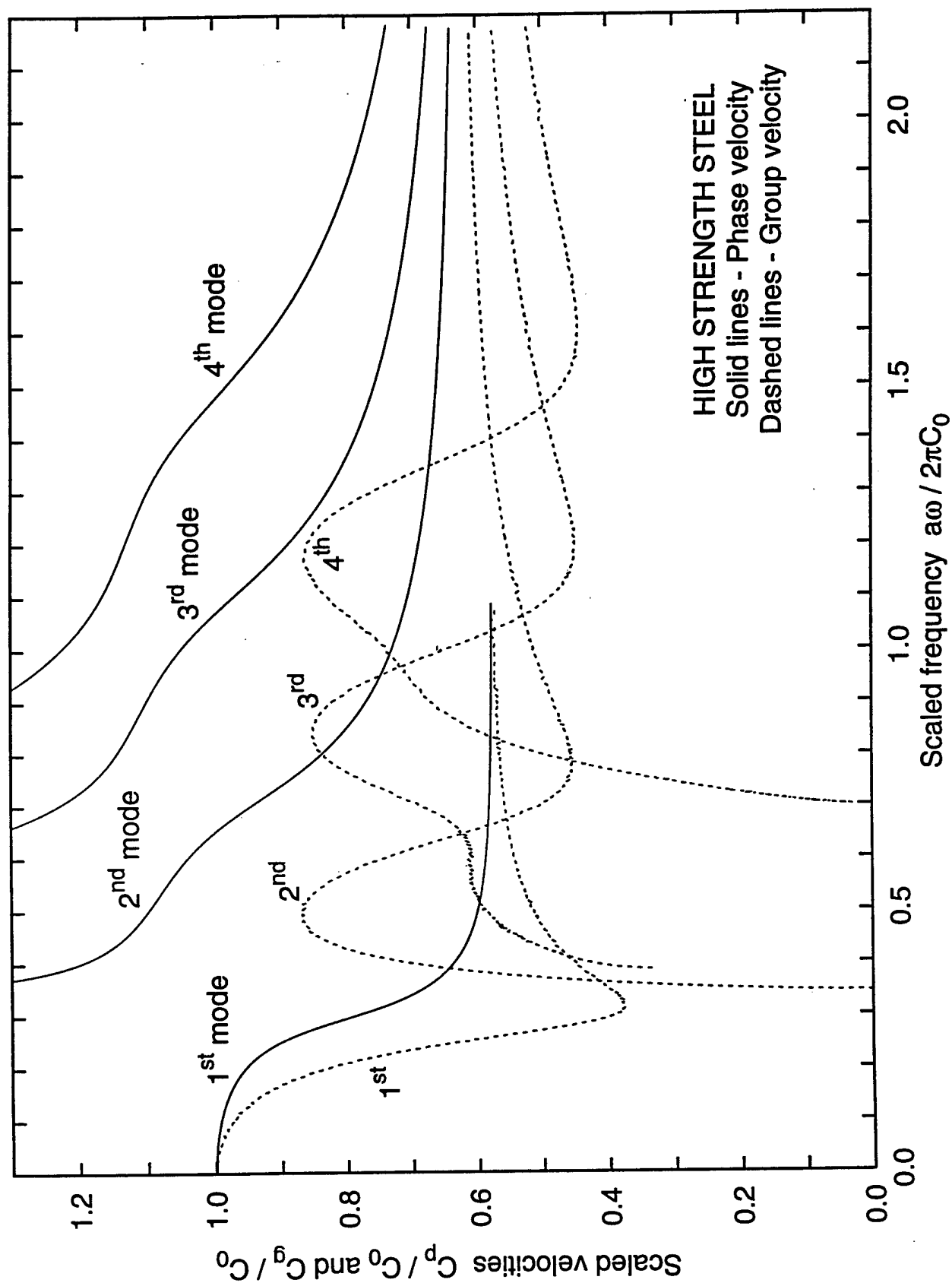
Figure 3-5. The first four Pochhammer-Chree modes for High Strength Steel.

13
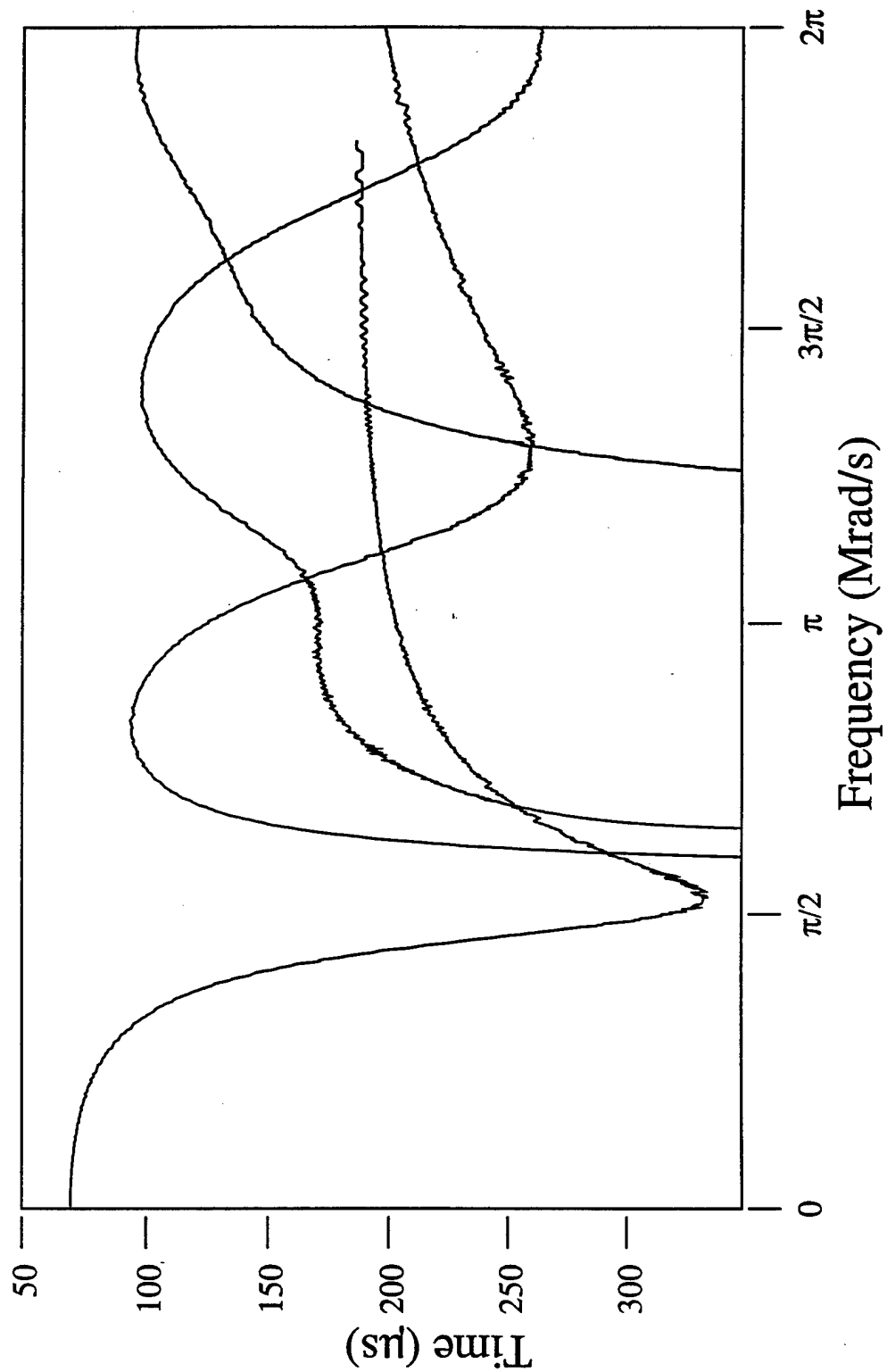
Figure 3-6. The group velocities for the first four Pochhammer-Chree modes converted to arrival times for the 1/2-inch bar.

14
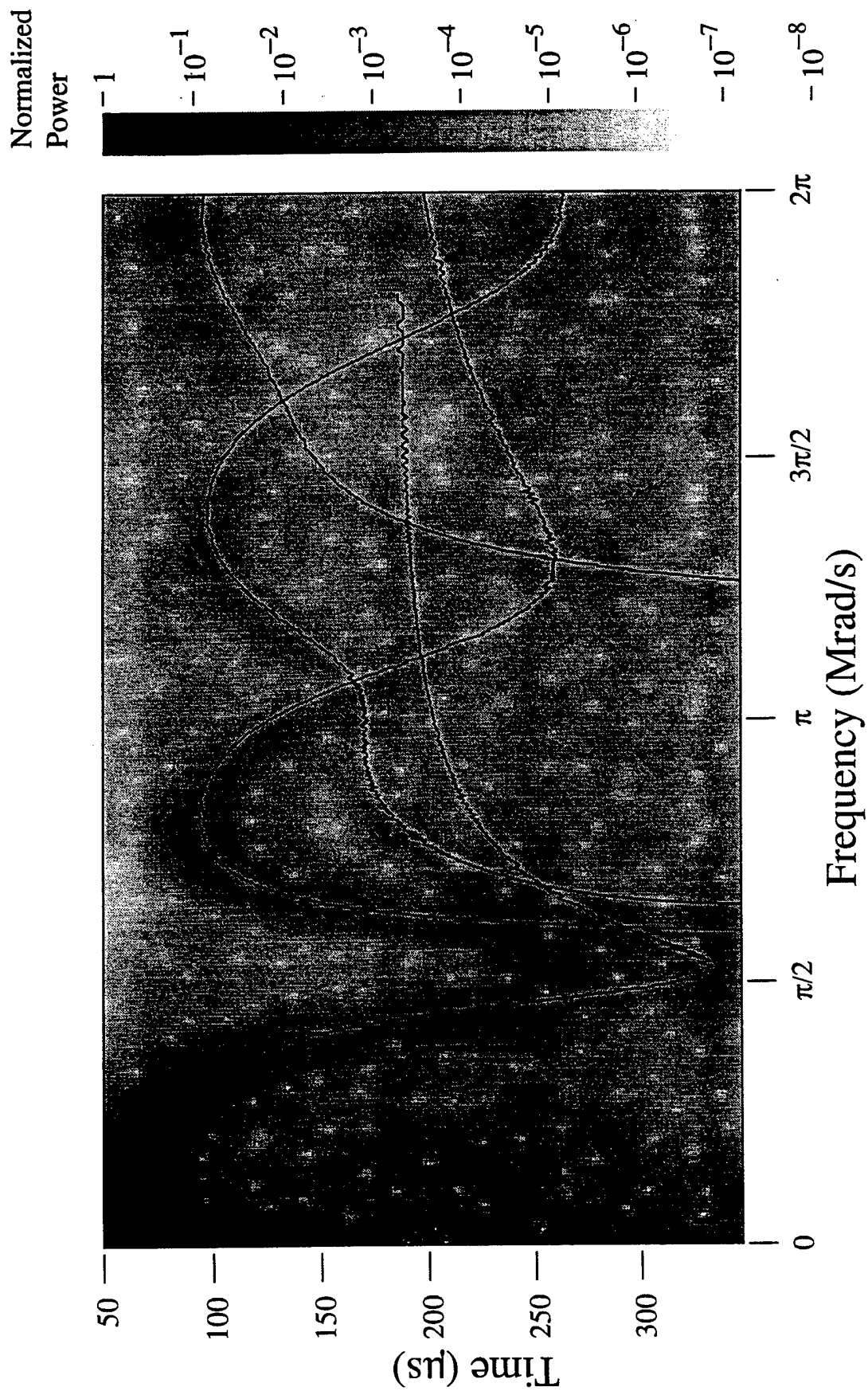
Figure 3-7. The ToA curves for the first four PC modes plotted on the gray scale image of the 1/2-inch bar record.

15
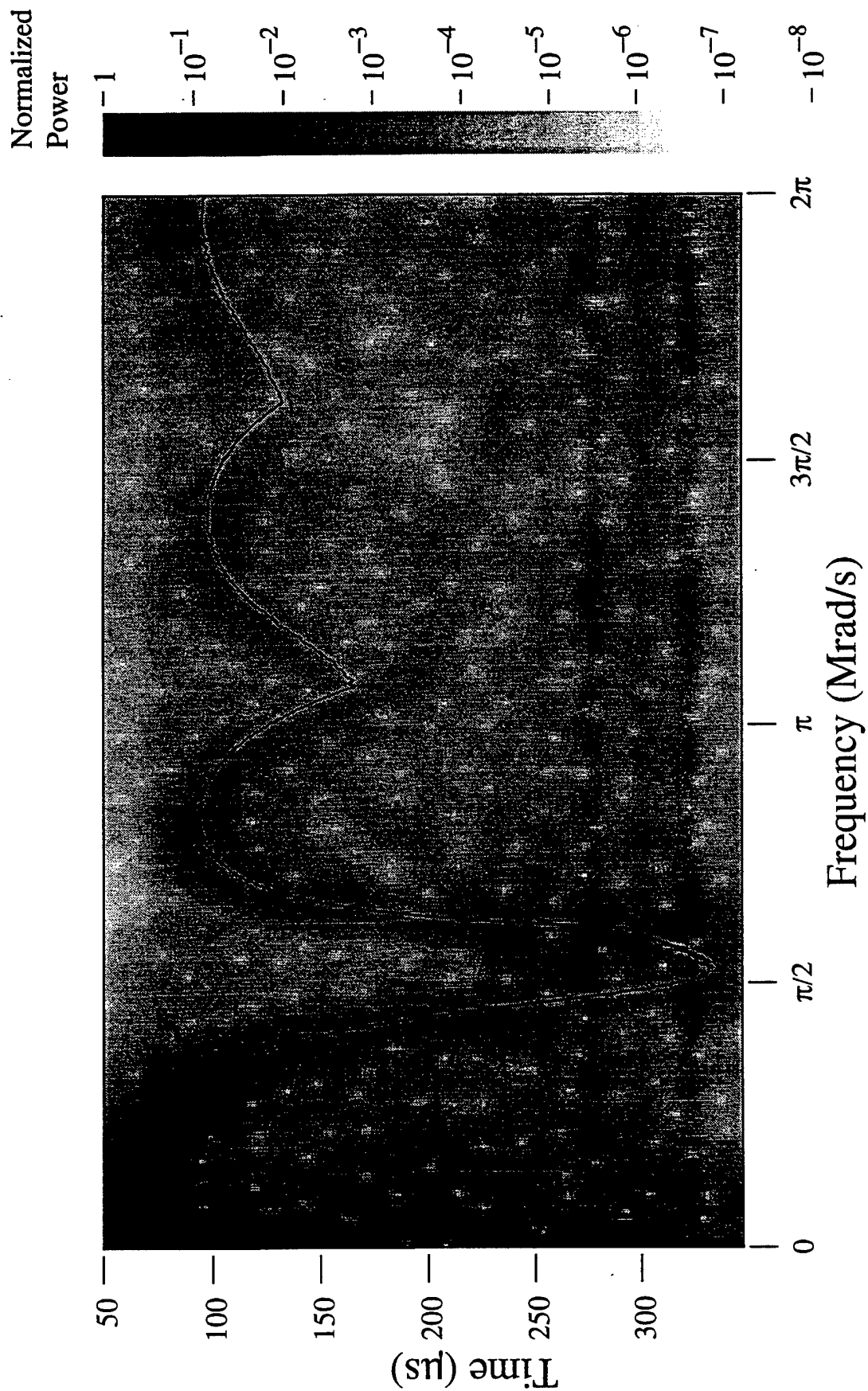
Figure 3-8.   The ToA curves with only the arrival of the fastest PC mode plotted on the gray scale image of the 1/2-inch bar record.
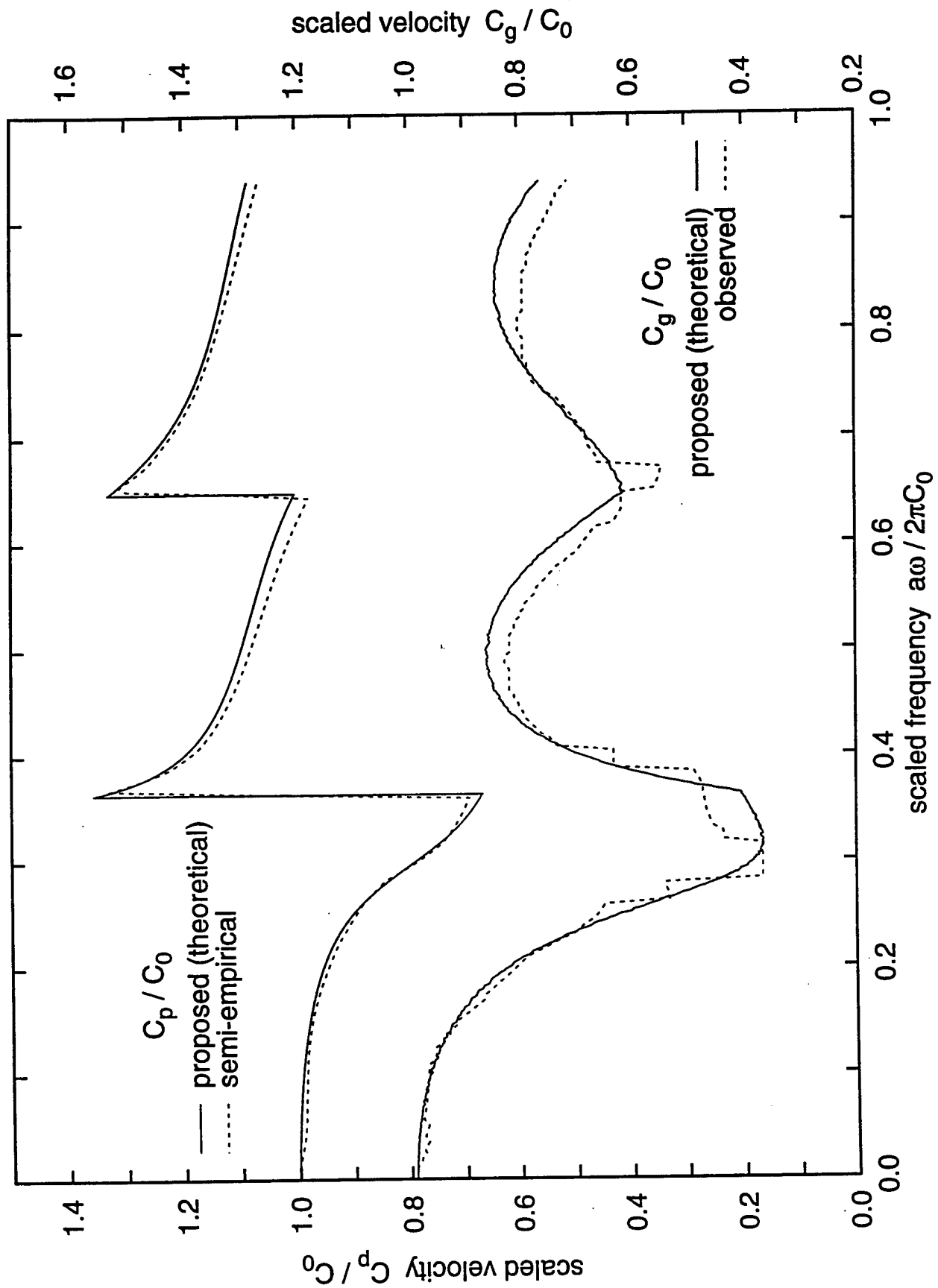
Figure 3-9. The proposed combined-mode dispersion curves and the semi-empirical dispersion curves derived from the 1/2-inch bar record.
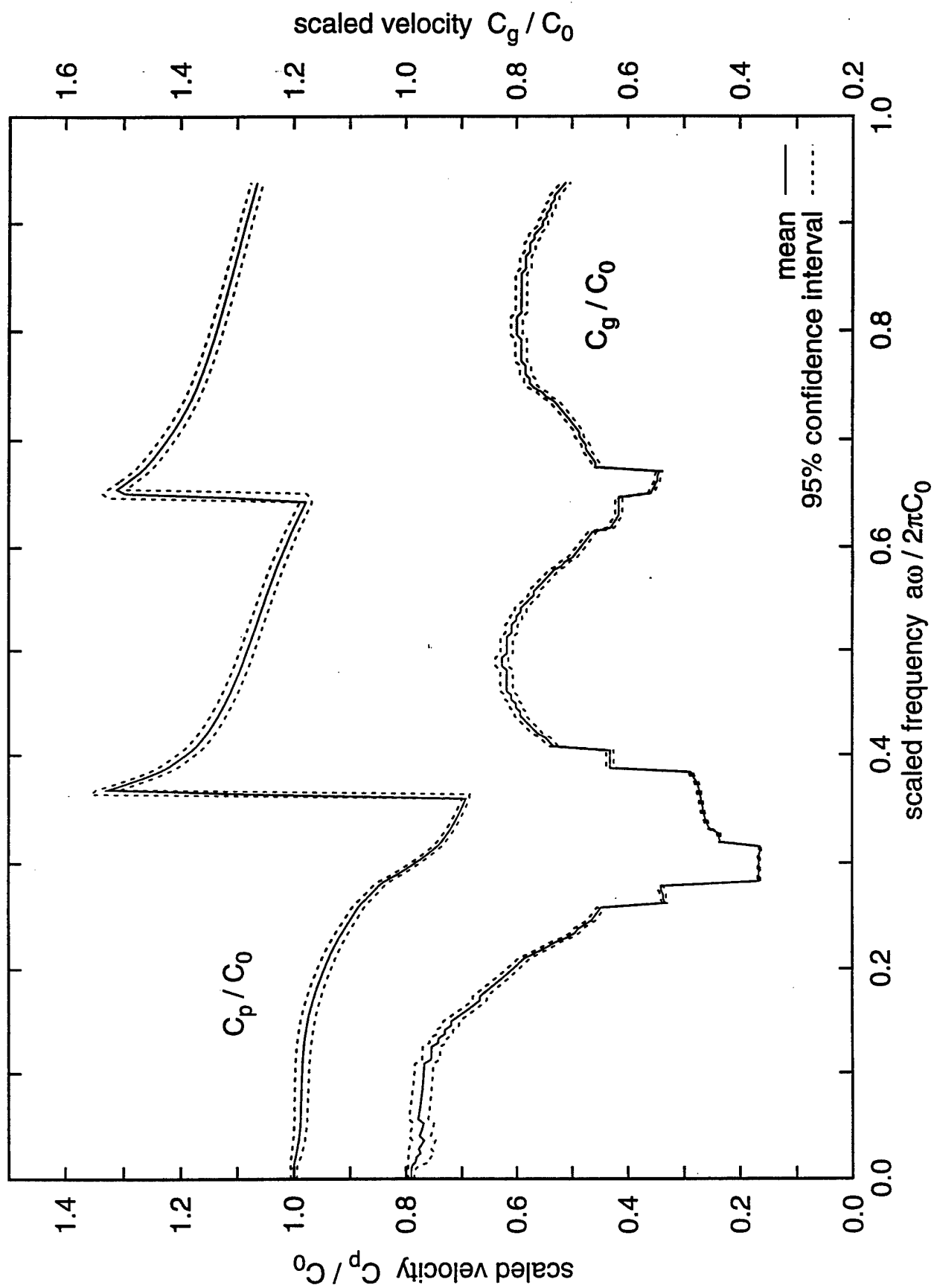
Figure 3-10. The mean and the 95% confidence band for the semi-empirical dispersion curves derived from the 1/2-inch bar record.

SECTION 4

DECONVOLVED SIGNALS AND DISCUSSION

From the gray scale plot in Figure 3-1, it is clear that a significant amount of energy carried by high frequency components arrives after the bulk of the low-frequency energy. This suggests that for a 1/8-inch bar, if the sampling time interval is 0.1μs or less, deconvolution of the measured signal will improve the peak of the raw signal, and by removing the high frequencies from the latter part of the raw signal, the accuracy of the entire signal is improved. GWFT can thus be used to determine whether a signal can be improved by deconvolution. Referring back to Figure 3-1, if the dark band does not extend beyond ~3π/4 Mrad/s, which is the case for sampling intervals of ~1 μs, performing deconvolution will not improve the signal at all.

The 1/8-inch signal is deconvolved by the RWFS method, using the semi-empirical dispersion curve in the DISBAS code. (DISBAS stands for dispersed basis functions (Lee and Crawford, 1993)) The undispersed signal is then analyzed by GWFT (the computer code is called GIFT-- we chose the i from the word 'window'). The gray scale for the undispersed pulse and the undispersed signal are shown in Figure 4-1. Comparing the pulses by themselves, the difference between the dispersed and the undispersed signals is very small-- a few percent in the peak. Note that the patterns in the low frequency region are unchanged by the deconvolution. But the frequency spectra shown in the gray scales are very different. That shown in Figure 4-1 is a shock--the high frequencies associated with the shock arrive at the shock front. The dispersed wave spectrum shown in Figure 3-1 is **not** a shock spectrum--the high frequency components do not appear at the front. To see more clearly the difference between these two cases, the Fourier coefficients at the front of the measured and deconvolved signals in Figure 3-2 and Figure 4-1 are plotted in Figure 4-2. These are the numerical values of the C_{mn} 2 μs after ToA of the raw signal. The difference is obvious. In general, no dispersed signal is a good approximation to a shock. The high frequency power in the dispersed pulse is less than the deconvolved pulse.

We deconvolve the 1/2-inch bar signal using the DISBAS code with the semi-empirical dispersion curve. The undispersed signal shows two distinct peaks (Figure 4-3) of approximately the same magnitude. The width of the first peak, measured from the bottom of the valley in between the two peaks, is slightly smaller than the second peak, which shows a 'kink' on the descent from the first peak and another one on the rise to the second peak. Figure 4-4 shows the front of three deconvolved signals from this measured pulse, one using the theoretical combined-mode, another using the semi-empirical dispersion curve, and a third one using the first PC mode. Figure 4-5 shows the complete deconvolved signal using the semi-empirical combined-mode curve. The semi-empirical curve gives the sharpest shock front for the deconvolved signal. The theoretical combined-mode curve gives a step on the rise to the second peak but a more gradual rise to the peak. Recall from Figure 3-9 the group velocities of the second and third modes in the semi-empirical dispersion curve are slightly slower than those given by the theoretical combined-modes. This means that the frequencies associated with the second and the third modes will be 'pushed' further toward the front upon deconvolution. Although the first PC mode is able to give the double peak structure, the deconvolved signal shows a gradual rise as well as

a lack of structure in the peaks. Figure 4-6 shows a comparison of the first 50 μs of the deconvolved pulse using DISBAS with the combined-mode curve and that using Gorham's method with the first PC mode. Aside from the Gibbs oscillations typical of Gorham's results, the definition of the peaks is not as sharp and there is no step to the second peak. The deconvolved signal obtained from the semi-empirical dispersion curve is more accurate because the dispersion of the high frequency components are included in the deconvolution as defined by the measured signal.

Because this signal and the 1/8-inch bar signal are obtained under identical experimental conditions, the deconvolved signal from the 1/8-inch bar should give the same double peak structure. Figure 4-1 shows the deconvolved signal for the 1/8-inch bar. The deconvolved signal shows multiple peaks. It appears that each peak in the raw signal is turned into a double peak, and the combined width of the two peaks is almost the same as the deconvolved 1/2-inch signal. We examined several other 1/8-inch bar records from this experiment. All of them show multiple peaks.

The agreement between the deconvolved signals from the 1/8-inch and the 1/2-inch bars is only approximate. Because the initial loading shock wave has to be the same (due to spherical symmetry) for these signals, the difference in the nature of these peaks has to be the result of differences in the bar geometry. Figure 4-7 shows the two adaptors used for the 1/8-inch and the 1/2-inch bars. The sizes of the two adaptors are the same; in particular, the surface exposed to the shock has the same total area (the sum of the bar area and the adaptor area). When a shock impacts the bar-adaptor structure, the first signal transmitted to the sensing element is directly through the bar itself. A second signal coming from the adaptor also squeezes the end of the bar, but part of this signal has to pass through the water jacket before reaching the side of the bar. The total impulse delivered to the bar-adaptor structure is the same for both bars, but the portions of the impulse coming directly through the bars themselves are different. This is because the 1/8-inch bar occupies 1/80th of the area exposed to the shock but the 1/2-inch bar occupies 1/5 of the area. The accuracy offered by the combination of the GWFT, DISBAS, and the new combined-mode dispersion curve can be used to estimate detailed effects of the armor and the water jacket. These effects will be examined by a separate 2D continuum mechanics code. As long as bars of different diameter adaptors are used, the deconvolved signals cannot be expected to agree exactly even if the experiment were ideal.

Finally, we present a bar signal recorded in a recent underground test. The signal and its gray scale are shown in Figure 4-8. The bar used is a 3/8-inch diameter tungsten carbide bar. The sampling time is 0.1 μs. The gray scale plot shows a very distinct band at $3\pi/4$ Mrad/s that appears to correspond to another phenomenon specific to the underground test. The combined-mode dispersion curve for tungsten carbide is shown in Figure 4-9. Figure 4-10 shows the deconvolved signal using DISBAS and the theoretical combined-mode dispersion curve. For this signal there is a distinct reverberation in the latter part of the deconvolved pulse (after 120 μs).
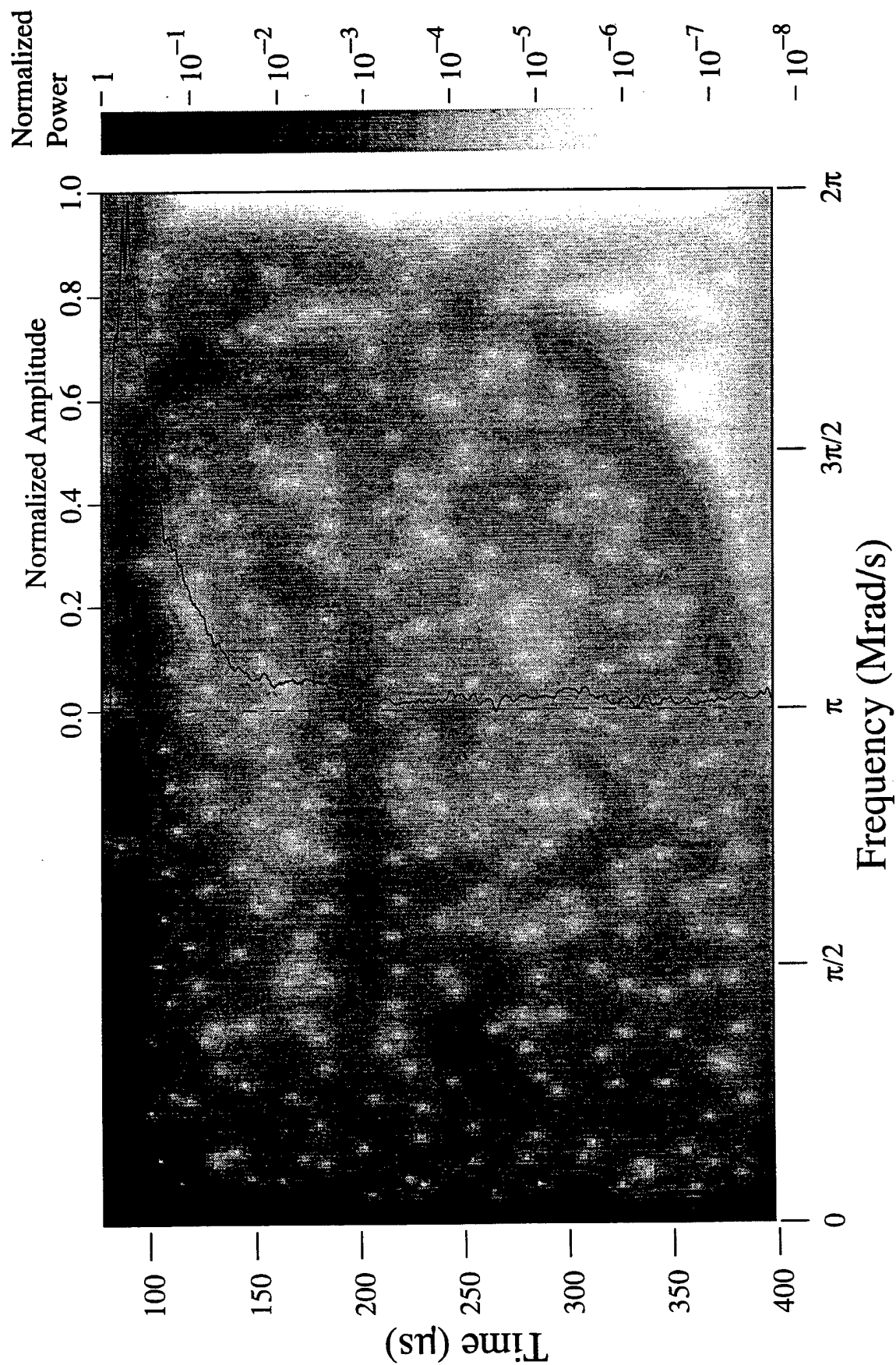
Figure 4-1. The deconvolved 1/8-inch bar signal (Figure 3-1) using the theoretical combined-mode dispersion curve (Figure 3-9).
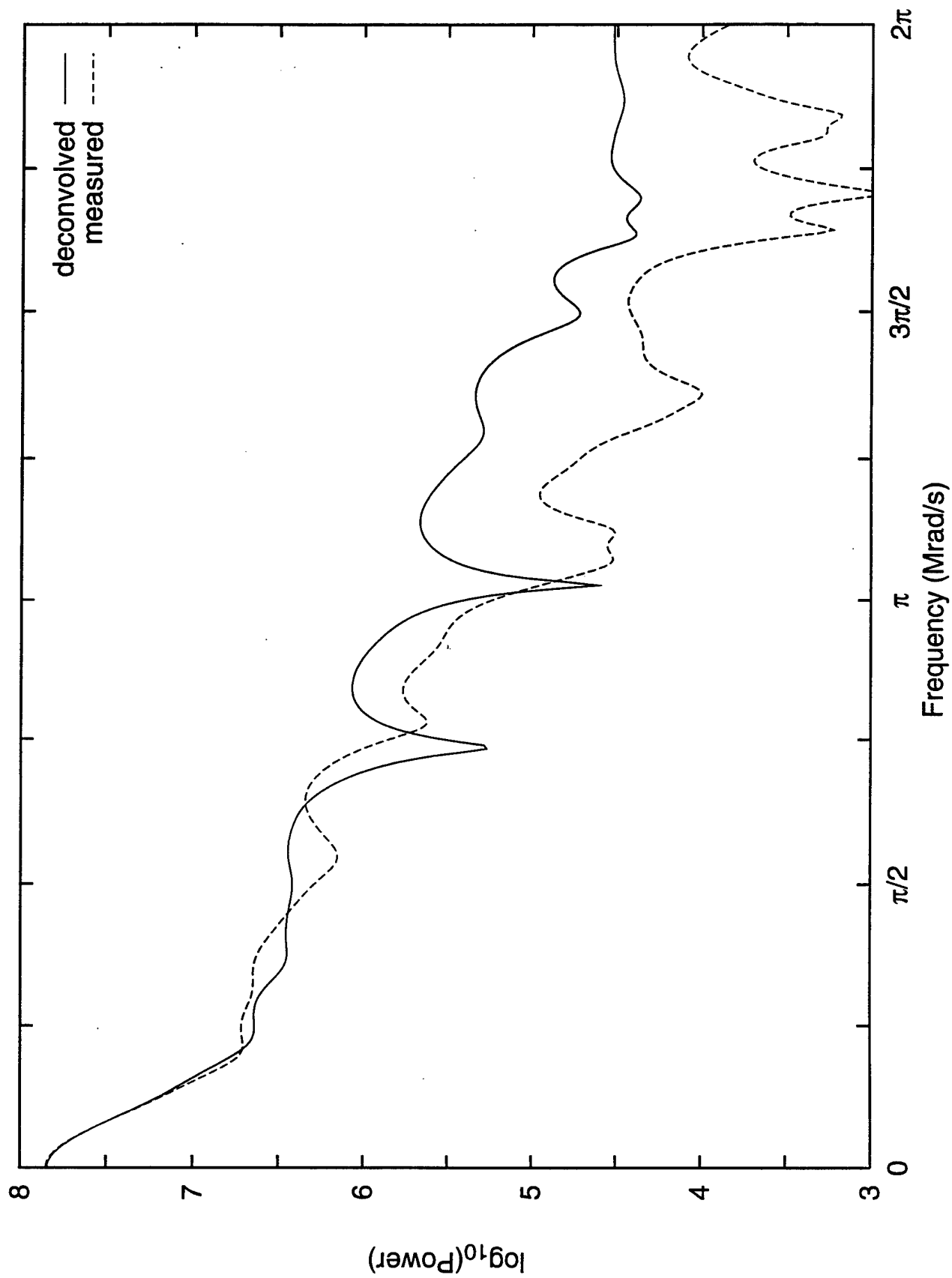
Figure 4-2. Frequency spectrum taken at ToA of the raw and deconvolved 1/8-inch bar signal.
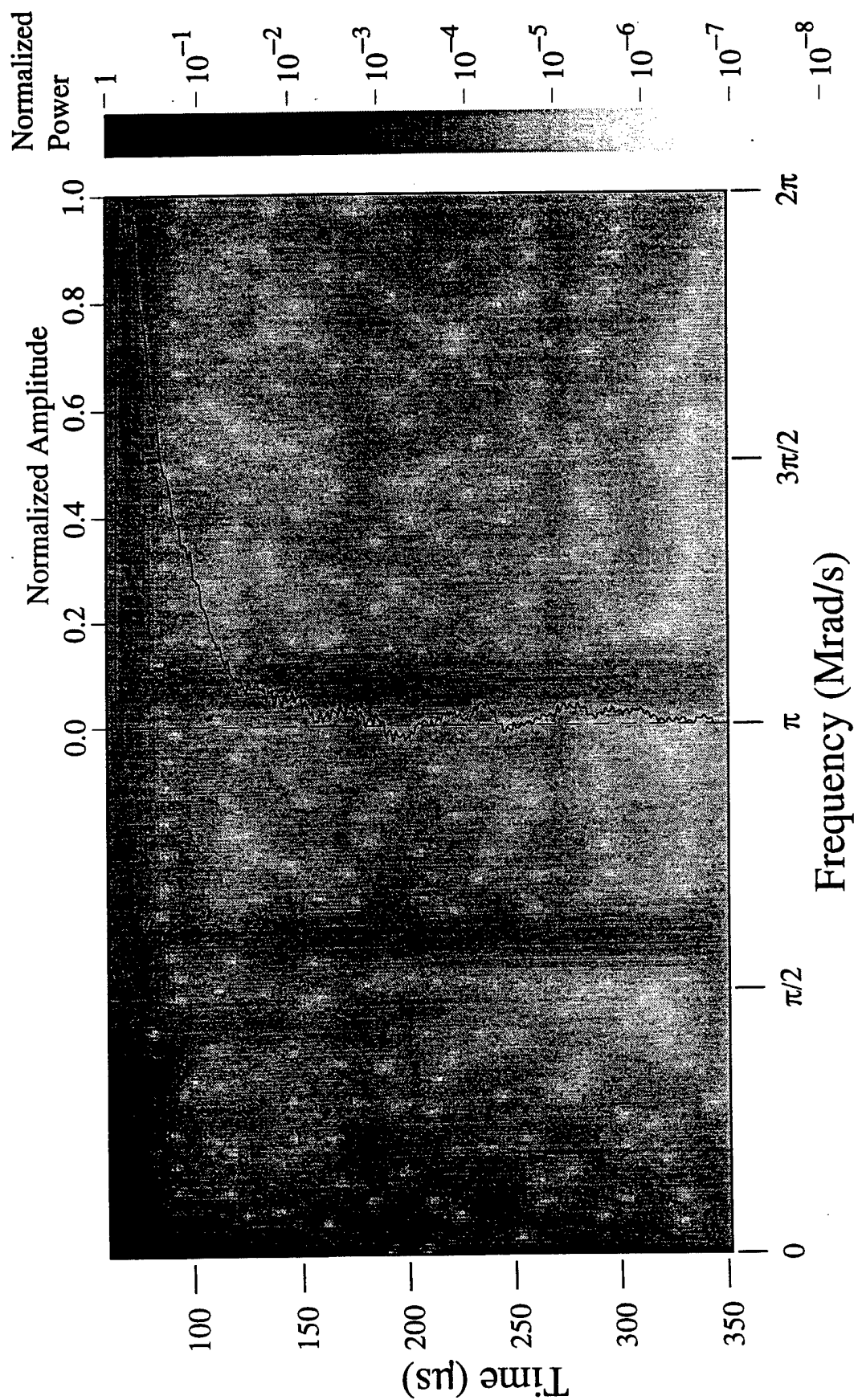
Figure 4-3. The deconvolved 1/2-inch bar signal (Figure 3-3) using the semi-empirical combined-mode dispersion curve (Figure 3-10).
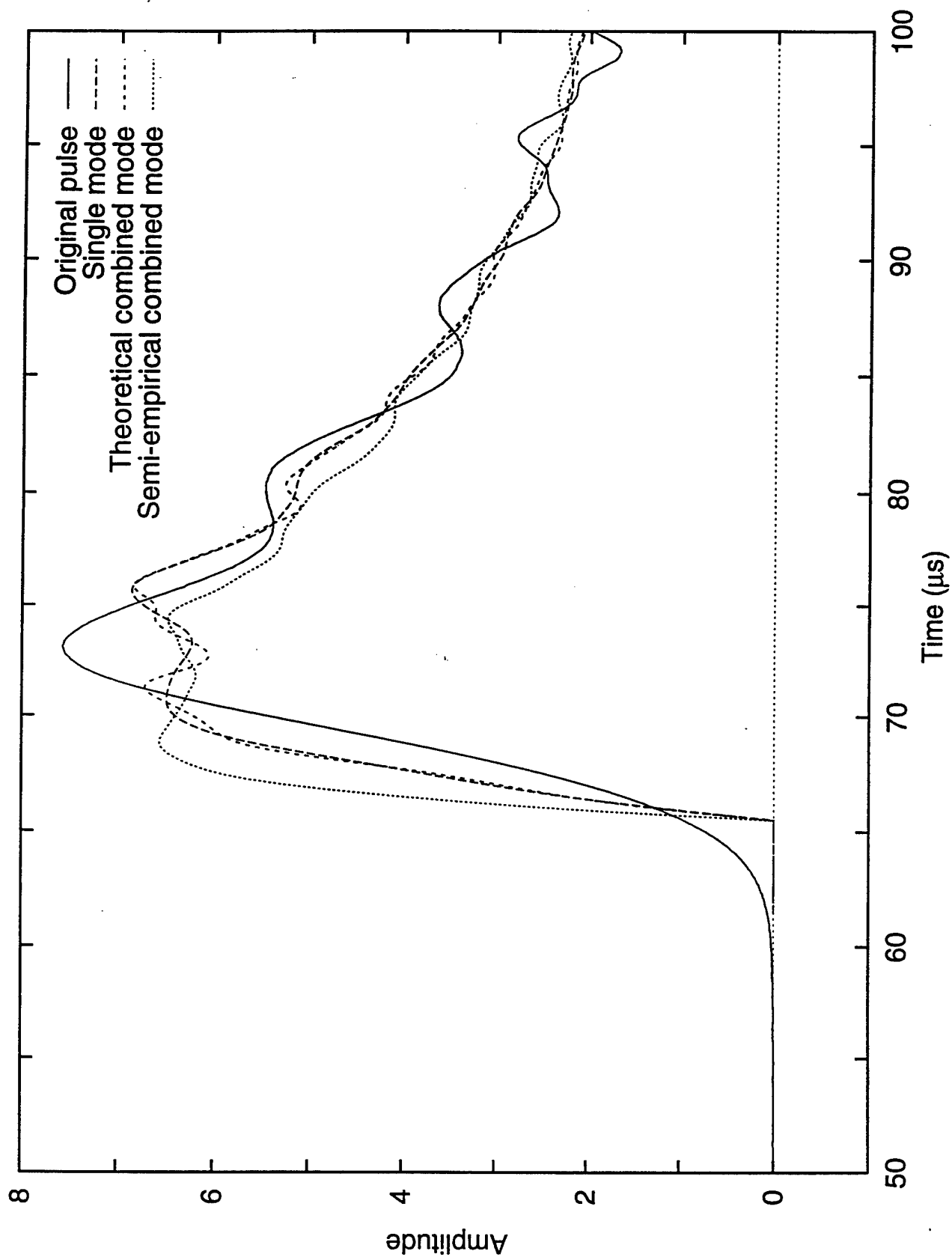
Figure 4-4.   The front of the deconvolved 1/2-inch bar pulse using the theoretical combined-mode, first PC mode, and the semi-empirical curves.

24
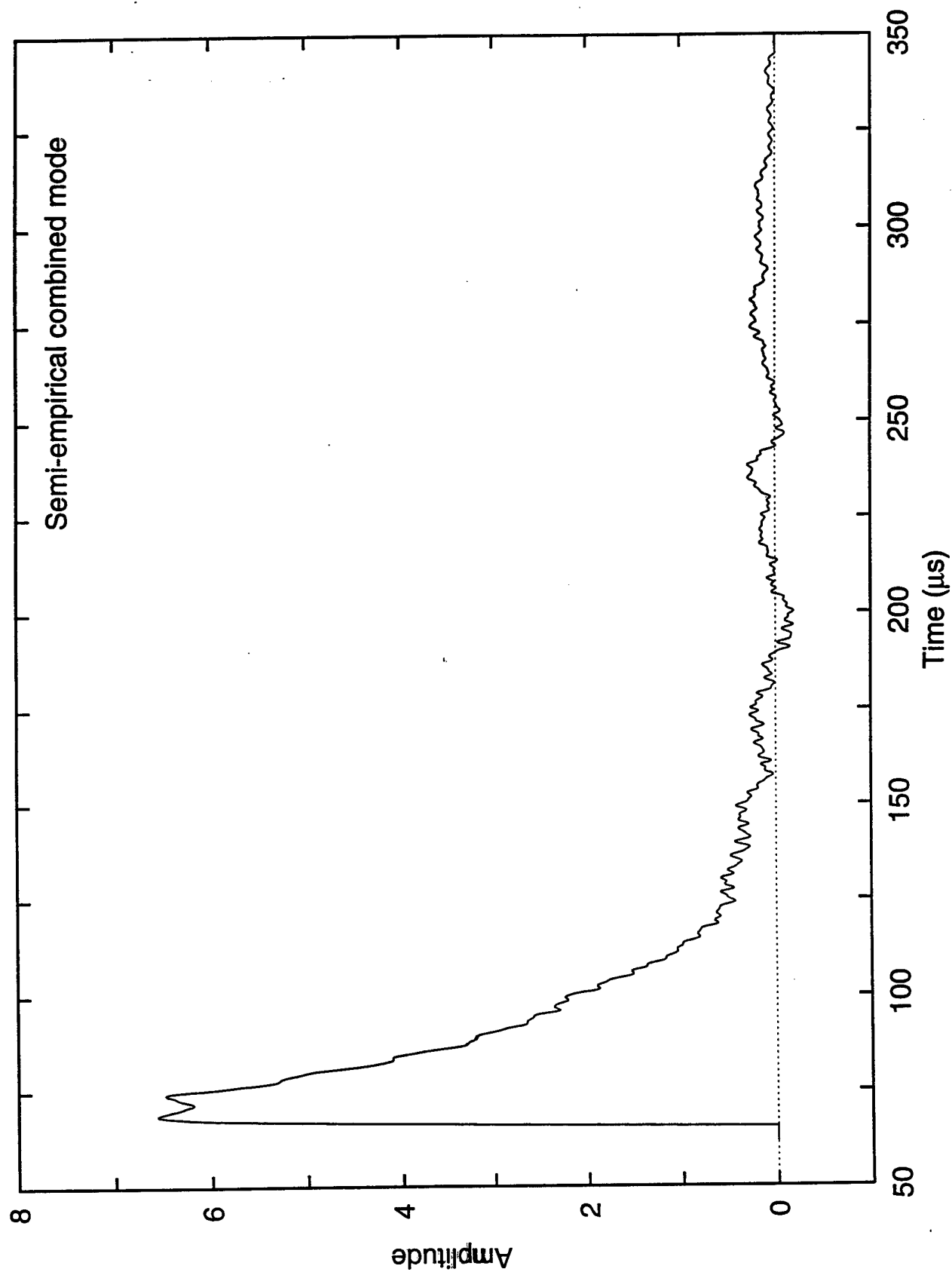
Figure 4-5.   The deconvolved signal of the 1/2-inch bar using the semi-empirical combined-mode curve.
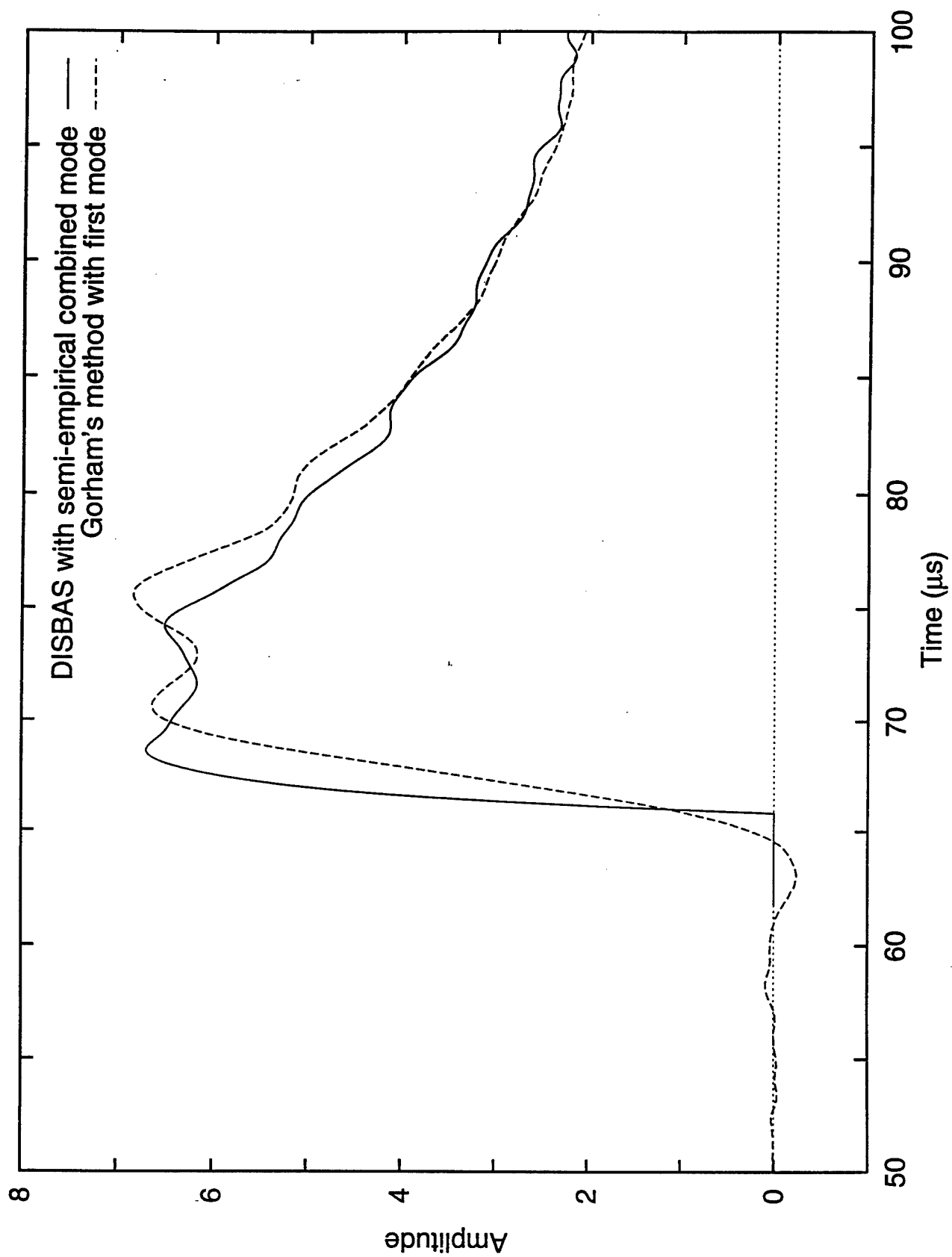
Figure 4-6.   The front of the deconvolved 1/2-inch bar pulse using DISBAS with the semi-empirical combined-mode curve and Gorham's method with the first PC mode.
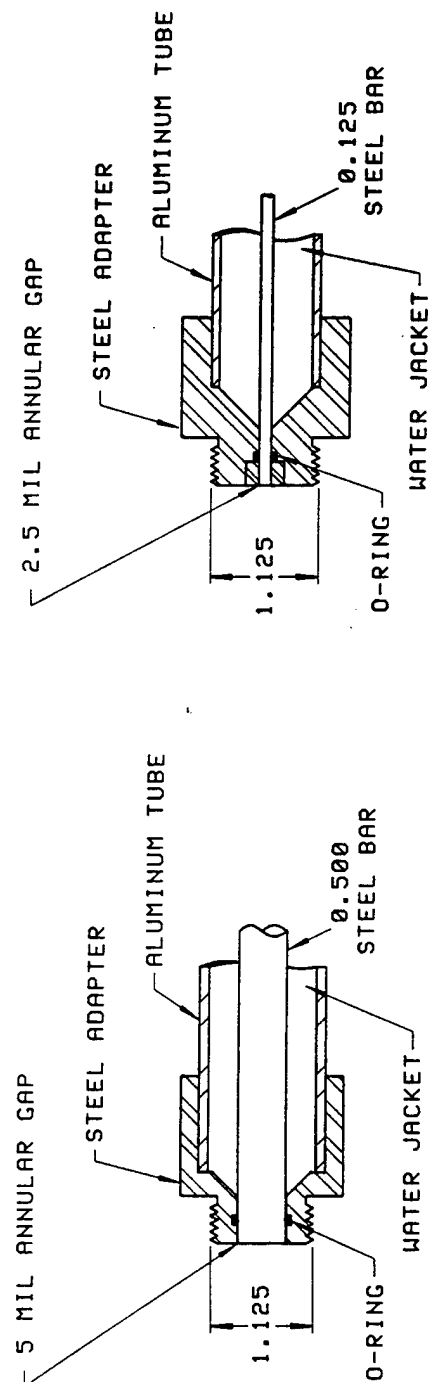
Figure 4-7. The adaptor designs for the 1/8-inch and the 1/2-inch diameter bars.

27
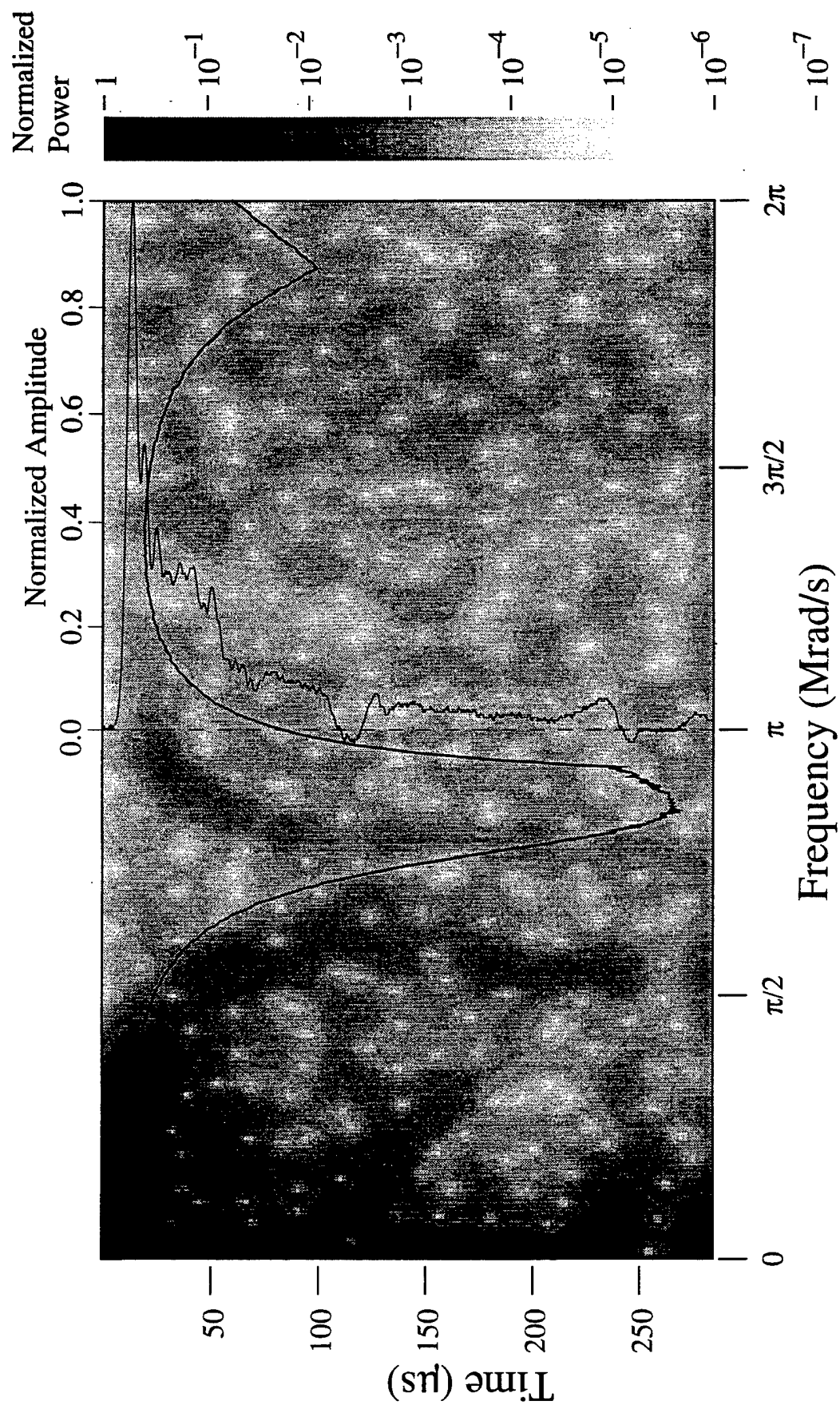
Figure 4-8. A quartz gage signal from a recent underground test using a 3/8-inch tungsten carbide bar.

28
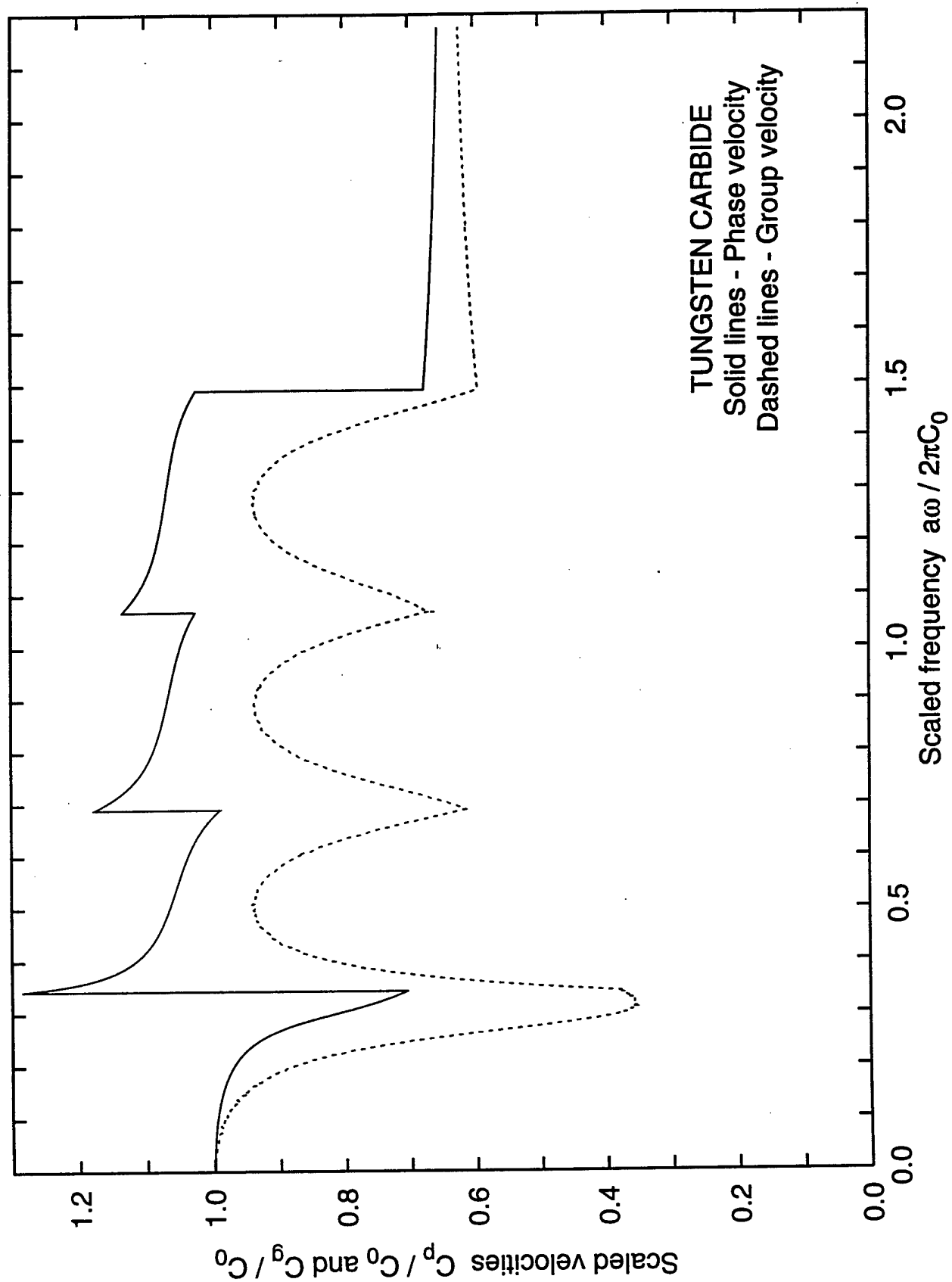
Figure 4-9.　The combined-mode dispersion curves for a tungsten carbide bar.
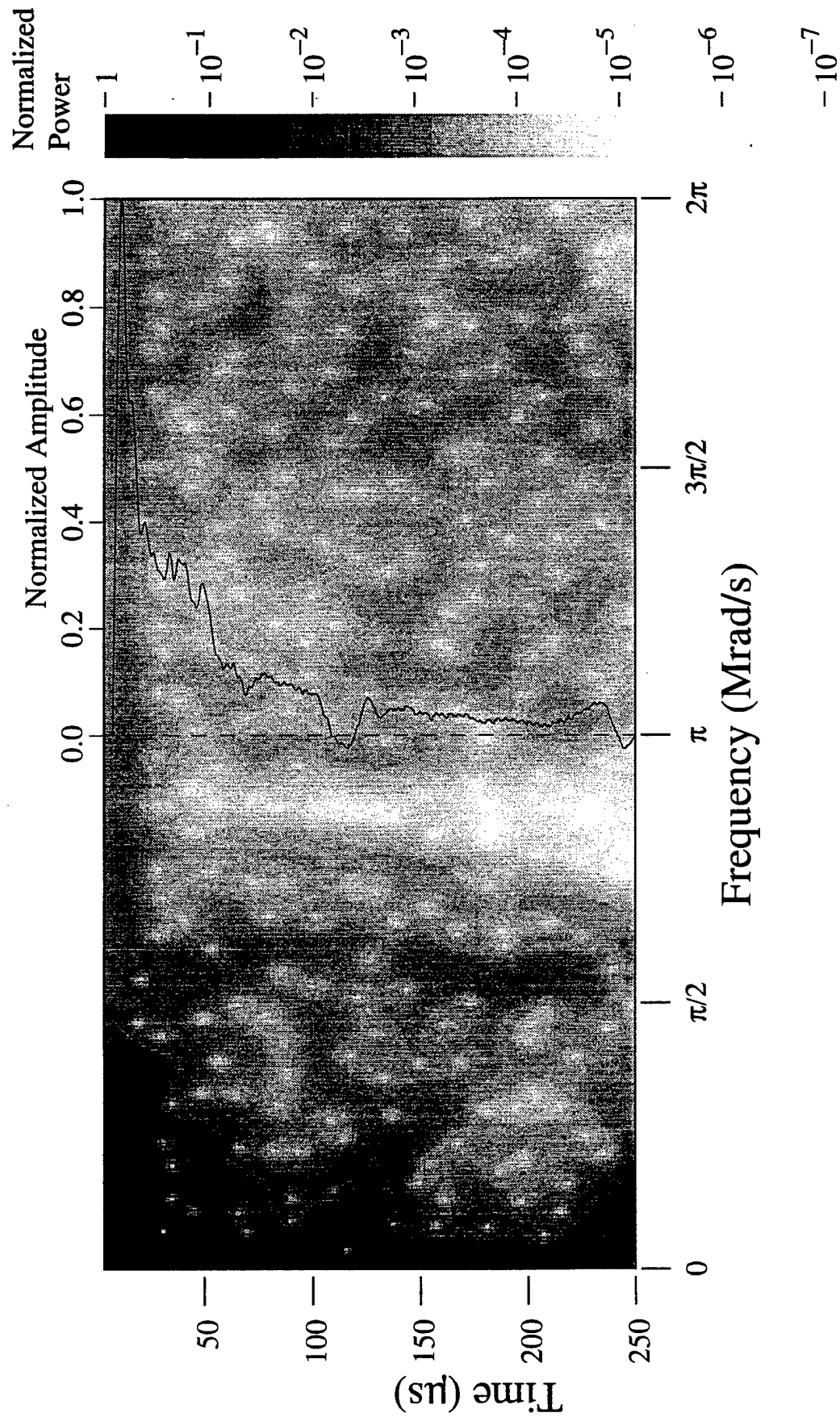
Figure 4-10.   The deconvolved signal from the 3/8-inch tungsten carbide bar.

SECTION 5

CONCLUSIONS AND RECOMMENDATIONS

We presented a mathematical technique GWFT (GIFT code) that is capable of deriving the dispersion modes from a bar signal. The character of the derived signatures agrees with the first three modes of Pochhammer and Chree. These signatures further suggest that, in frequency regions where multiple modes exist, the faster mode dominates. This information allows the construction of a dispersion curve from the signal. Using this method, we analyzed a set of 1/2-inch steel bar data taken from a set of water tank explosion experiments. We found that the 1/2-inch water-jacketed bars have a dispersion curve that can be represented by the combination of three PC modes. In regions where multiple modes exist, the faster mode is used. In this way, we created a theoretical combined-mode group velocity dispersion curve, and constructed the corresponding phase velocity curve from that. We also constructed a group velocity curve solely from the measured signal; and then constructed a semi-empirical phase velocity curve from that. Although the deconvolved signals from the semi-empirical curve gave a sharper shock and more structure at the peaks, we recommend using the combined-mode curve for deconvolution in general. After all, a detailed signal that allows the derivation of a highly accurate experimental dispersion curve is not easily obtained. It is definitely not a standard practice among experimenters in the field of explosive effects research. Moreover, because the semi-empirical curve contains some peculiar characteristics that pertain to this particular set of water tank experiments, the derived dispersion curve is strictly applicable only to this set of data. We used the semi-empirical curve to deconvolve the signals presented in this report because we wanted to demonstrate for the first time that an adequate dispersion curve can be derived from the signal for deconvolution purposes. We presented two new combined-mode dispersion curves, one for a high strength steel bar and the other for a tungsten carbide bar. The combined-mode dispersion curve gives better resolved peaks for the water tank data upon deconvolution using the RWFS technique (DISBAS code). The procedure of (a) using GIFT to derive the general character of the dispersion curve from the data, (b) modifying the theoretical PC modes to reflect the results of (a), and (c) performing the deconvolution using DISBAS, is the most accurate way to deconvolve a dispersed signal.

For blast and shock measurements, the best approximation to a shock is the deconvolved signal, not the raw signal, regardless of the size and speed of the bar. The 1/8-inch steel bar case was expected to show little difference in the spectra of the peaks in the deconvolved signal and the raw signal, but the peak from the raw signal lacks the high frequencies that distinguish a shock from a compression wave.

The deconvolved signals from the 1/8-inch bar and the 1/2-inch bar agree only in impulse and half-width. They differ significantly in the detailed structure of the peak, which contains a number of peaklets in both deconvolved signals. The degree to which the raw 1/8-inch bar signal represents the deconvolved 1/2-inch bar record needs to be reexamined based on the differences in the respective bar-adaptor geometries. The detailed nature of the shock interaction with the bar-adaptor system must be studied. This requires more sophisticated 2D code calculations.

31

When such a code is available, it will allow the analyst to examine the effects of the armor as well as the water jacket design prior to an experiment.

We presented GIFT results of a bar gage record from a recent underground test. We caution that while the water tank data presented represent typical signals, this underground test signal is the only signal with such resolution in both time and frequency. The gray scale plot shows distinct features that are specific to the underground test. Deconvolutions using the combined-mode curve were performed using the DISBAS code. The result shows features in the tail of the deconvolved signals that resemble wave reverberations. The RWFS technique is shown to be useful not only at better defining peaks and wave fronts but, by accurately removing the high frequency components from the tail of the raw signal, giving highly resolved undispersed information at the tail of the signal also.

We recommend: (1) GWFT be incorporated into the bar gage design process prior to any blast and shock experiment, (2) GWFT be used to extract the character of the dispersion from the raw signal and (3) the theoretical Pochhammer-Chree dispersion relation modified by the results of (2) be used by DISBAS to obtain the most accurate deconvolution.

The combined modes should be understood from a basic elastic wave propagation viewpoint which requires a 2D small strain code with advanced numerics that controls and minimizes numerical diffusive and dispersive errors.

SECTION 6

REFERENCES

Brigham O B 1974 The Fast Fourier Transform (Englewood Cliffs: Prentice-Hall)
Coleman P and Petersen C Private Communications July 1993
Curtis C W 1954 J. Appl. Phys. **25** 928
Daubechies I, Grossmann A and Meyer Y 1986 J. Math. Phys. **27** 1271-1283
Daubechies I 1990 IEEE Trans. Inform. Theory **36** 961-1005
Gorham D A 1983 J. Phys. E: Sci. Instrum. **16** 477-9
Kolsky H 1963 Stress Waves in Solids (New York: Dover)
Lee C K B and Crawford R C 1992 A new method for analyzing dispersed bar gage data
    Report RDA-TR-2-2261-2301-001 Logicon RDA Los Angeles (UNCLASSIFIED)
Lee C K B and Crawford R C 1993 Meas. Sci. Technol. **4** 931-937
    Meyer S L 1975 Data Analysis for Scientists and Engineers (New York: Wiley)
Pochhammer L 1876 J. reine. angew. Math. **81** 324 and Chree C 1889 Trans. Camb. Phil.
    Soc. **14** 250
Whitham G B 1974 Linear and Nonlinear Waves (New York: Wiley)

APPENDIX A

THE EFFECT OF WINDOW WIDTH ON GWFT

In this appendix, we present a numerical study of the effect of varying the Gaussian window width. The objective of this study is to estimate an optimum window size for the data from the water tank experiments. Here we will refer to the gray scale plot of the power of the coefficients C_{mn} as the image because the main objective of this study is to learn how to sharpen the dark band.

Before we sharpen the image, it is useful to reiterate the procedure for how these images (gray scale plots) are obtained, and deduce certain properties of the image from the mathematical formulation. Consider again Equations 2.3, 2.4, and 2.5. We compute the Fourier coefficients for the signal $\phi(t)$, at the time τ and the frequency ω by the discrete form of

$$C(\omega,\tau) = \int_0^\infty \phi(t)g(t-\tau)\exp(-i\omega t)dt \tag{A.1}$$

which is

$$C_{mn} = \int_0^\infty \phi(t)g(t-n\Delta t)\exp(-i\omega_o t)dt \tag{A.2}$$

The window function is a translated Gaussian,

$$g(t-\tau) = \frac{1}{\sigma\sqrt{2\pi}}\exp\left(-\frac{1}{2}\left(\frac{t-\tau}{\sigma}\right)^2\right) \tag{A.3}$$

where σ is the window width parameter, and τ is the translation. The translated Gaussian function has the transform

$$G(\omega) = \exp(-\omega^2\sigma^2/2 - i\omega\tau) \tag{A.4}$$

or, in discrete form,

$$G_{mn} = \exp(-m^2\omega_o^2\sigma^2/2 - imn\omega_o\Delta t) \tag{A.5}$$

Comparing Equations A.3 and A.4 it is seen that σ has the opposite effect on g and G. A small σ sharpens g but widens G. In our application, the integral in Equation A.2 is expected to be strongly affected by the choice of the window parameter in the Gaussian. We therefore expect features in the image to display such an effect of the time window.

We choose to look at the white spots as indicators of the resolution. They arise in the following

manner. Both the real and imaginary components of the C_{mn} are highly oscillatory in both time and frequency, and the phase relationship between the two at any given time and frequency is also quite variable. At the white spot locations both components are near zero, so the power is low. The C_{mn} are computed on a discrete grid whereas the true positions of zero power are not; some fall closer to grid points than others, so the white spots are not equally white.

In this study, we start with a narrow time window. Figure A-1 shows the result. The dark gray region in Figure 3-3, which stretches out to a frequency of ~π/4 Mrad/s is now extended to ~ π/2 Mrad/s. Note that the white spots that resemble diamonds in Figure 3-3 are now stretched into short, light gray streaks with smaller thickness. The frequency information is definitely smeared by this window. But the time resolution is excellent--particularly at the front of the pulse where the gray scale sharply darkens to maximum power. The rate of darkening in the time direction follows the rapid power rise of the pulse almost exactly. The narrow window makes the Gaussian very localized in time, but with poor frequency resolution.

As the time window widens, Figure A-2, and A-3, the boundary of the darker low frequency region moves to the left. At the same time, the light gray streaks begin to shrink to the shape of small ellipses. Further increases in the time window improve the resolution of the image in the high frequency region. By about Figure A-3 the dark band has taken the shape of the the semi-empirical dispersion curve. It is also clear that the dark region at the upper left of the figure is smearing more and more in the time dimension. This is to be expected as the window widens. Because there is very little dispersion in the low frequency region and the dispersive behavior in this region is well understood [1,2,3], we concentrate this study on optimizing the resolution of the dark band in the high frequency region and give up the accuracy in the low frequency region.

As the time window widens further, Figure A-5 through A-8, the diamonds begin to turn into vertical ellipses. The ToA part of the signal, where the power sharply rises, is further smeared. The boundary between the low frequency dark region and the lighter high frequency region, however, has stopped moving to the left. Numerically this means that the frequency location of this boundary has converged. By convergence we mean further increases in the time window width will not move the boundary to a lower frequency. At the first maximum, the power is so smeared that it would be difficult to determine the arrival of those frequencies to within 25 μs. On the other hand, the vertical part of the dark band is becoming more narrow. Recall the abrupt jumps in the dark band near the first minimum. The width of the dark band in this region is much better resolved by a time window of 14 μs [Figure A-8].

We use the halfwidth (computed where the power is two orders of magnitude above its minimum) of the white spots as a measure of the resolution. Note that the general character of the half width of the white spots is insensitive to the exact magnitude of the power where the half width is computed as long as the chosen magnitude is neither too low (where it will be affected by noise), nor too high (where it is affected by the oscillations near the peaks). As we widen the time window, the halfwidths of the white spots in the time direction widens. As we reduce the window, the halfwidths decrease until they reach the sampling interval of the data.

The opposite behavior occurs in the frequency direction. As the time window is increased, the halfwidth in the frequency direction decreases until it reaches the Nyquist frequency of the data.

Figure A-9 shows the average of the whitest spots. For this data set the frequency resolution is as good as possible (the Nyquist frequency) for window widths greater than about 10 µs. The time resolution decreases with decreasing window size until the data sampling rate (0.1 µs) is reached. Thus 10 µs is the optimum window.. Wider windows sacrifice the time resolution; narrower windows sacrifice frequency resolution.

We could have used other means of estimating the resolution of the white spots, such as computing the derivatives of $C(\omega,\tau)$ with respect to frequency and time in the vicinity of the spots, but we do not feel that the choice of optimum window size would have been substantially different.

In terms of numerical convergence, we learn from this study that as long as we define the region and the direction (time or frequency) that convergence is desired, it can be achieved. For the horizontal features, such as peaks and plateaus, reducing the time window will improve those aspects of the image, but a limit exists where the dark band cannot be further reduced regardless of how small the window is reduced. Widening the time window improves the image of the steep part of the dark band, namely, near the first minimum. Again, at some large window width, further widening will not change the width of the band. Judging from this behavior, we conclude that an optimum value for the window width exists. Of course, in theory a more defined dispersion curve can be derived by varying the window size for different portions of the dark band. This would require a significant effort, and the improvement in the accuracy of the dispersion curve is not expected to be large. Finally, we would like to point out that an acceptable optimum that gives reasonable resolution in both directions to allow the derivation of a dispersion curve may not exist for all dispersed signals.

Figure A-1.   Numerical study: 2-μs Gaussian window.

Figure A-2. Numerical study: 4-μs Gaussian window.

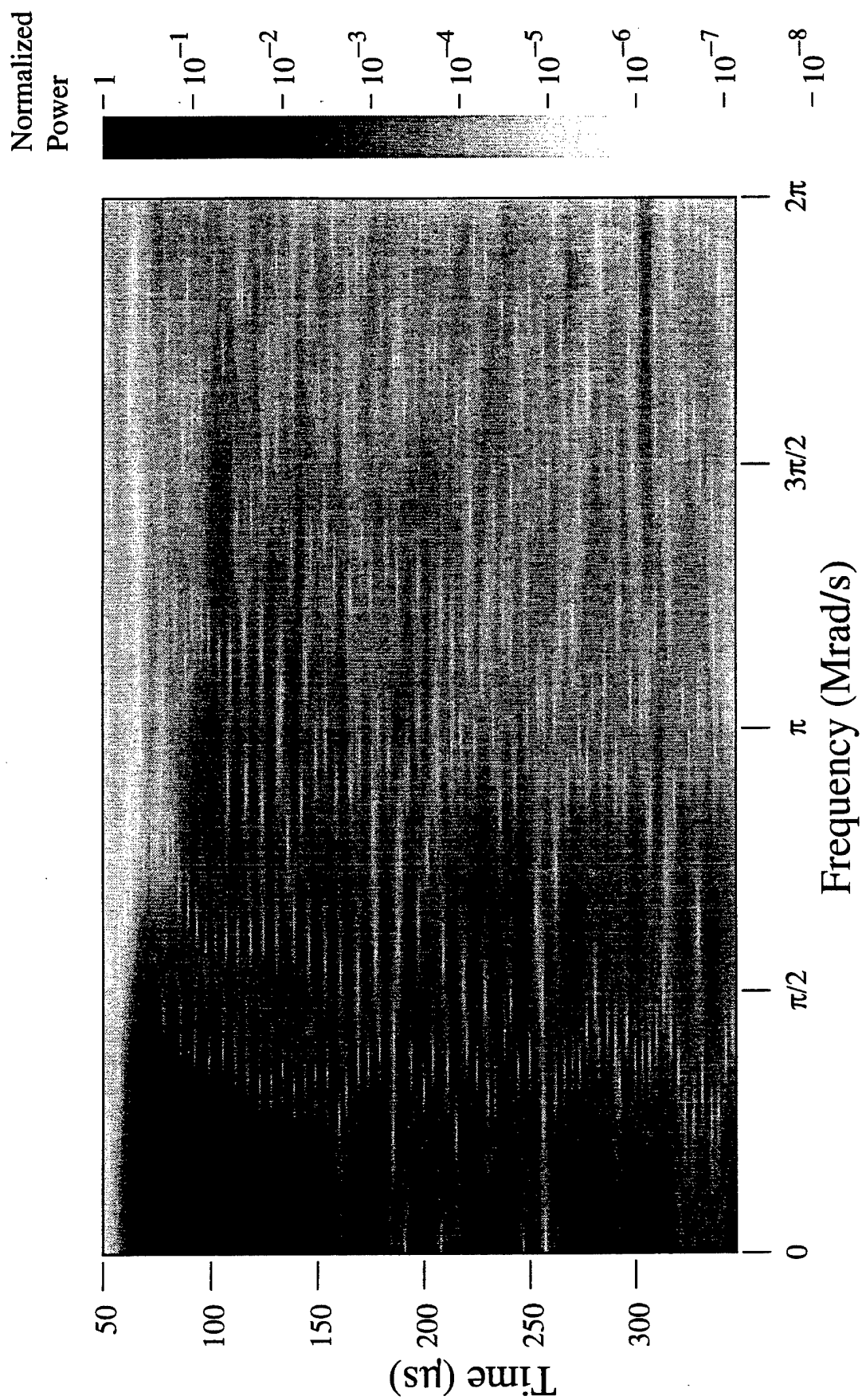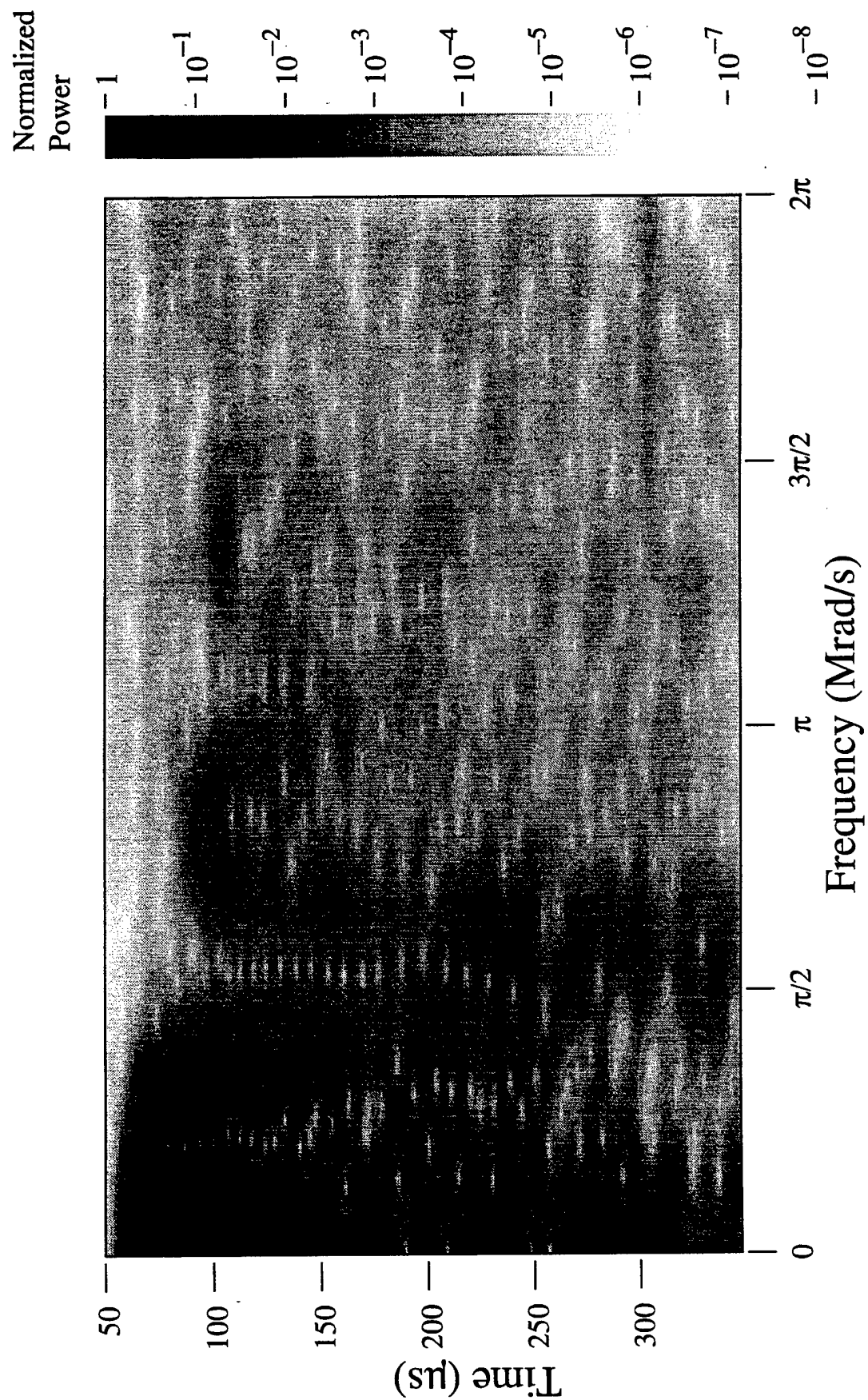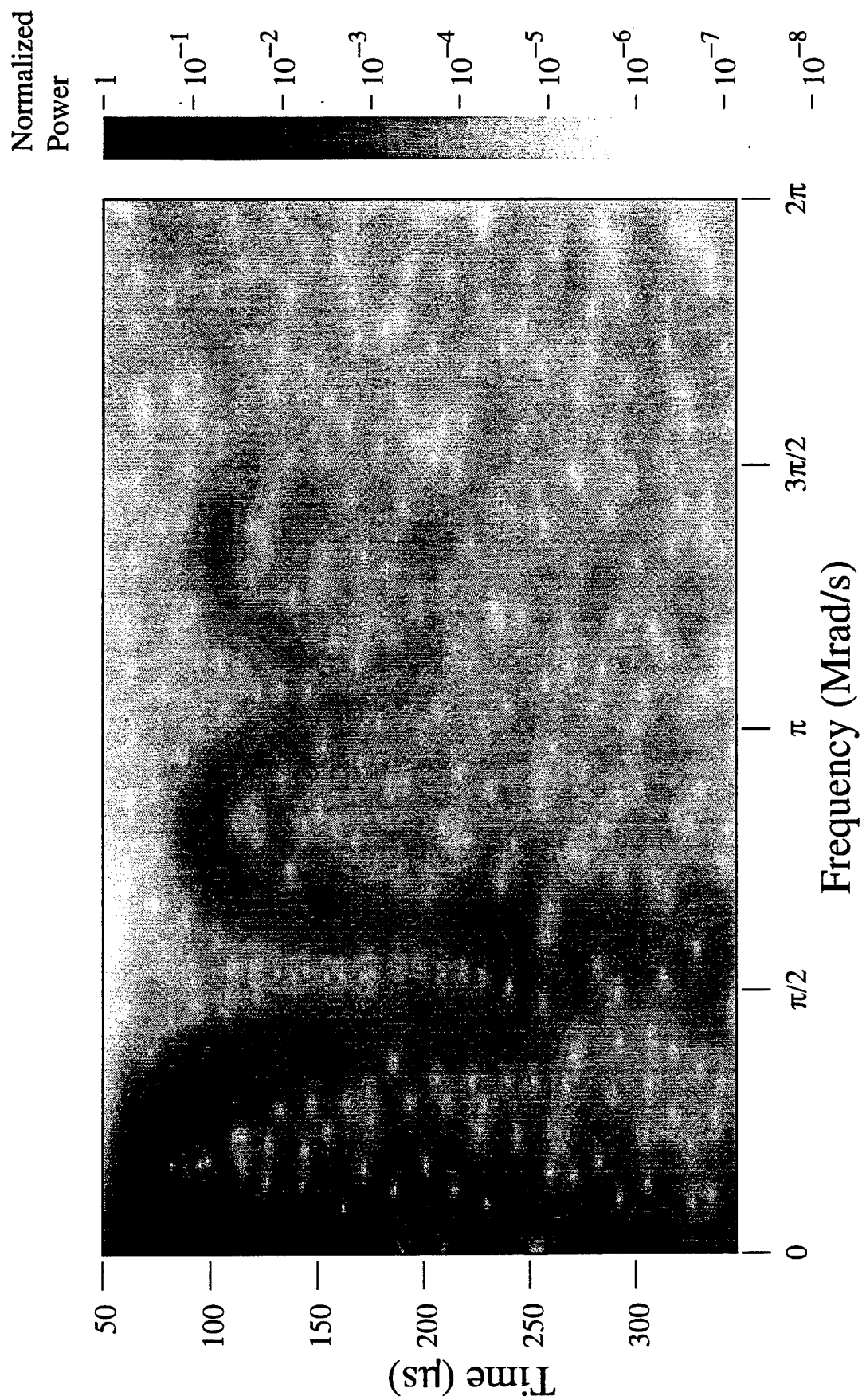Figure A-3.   Numerical study: 6-μs Gaussian window.

Figure A-4.   Numerical study: 8-μs Gaussian window.

Figure A-5.   Numerical study: 9-μs Gaussian window.
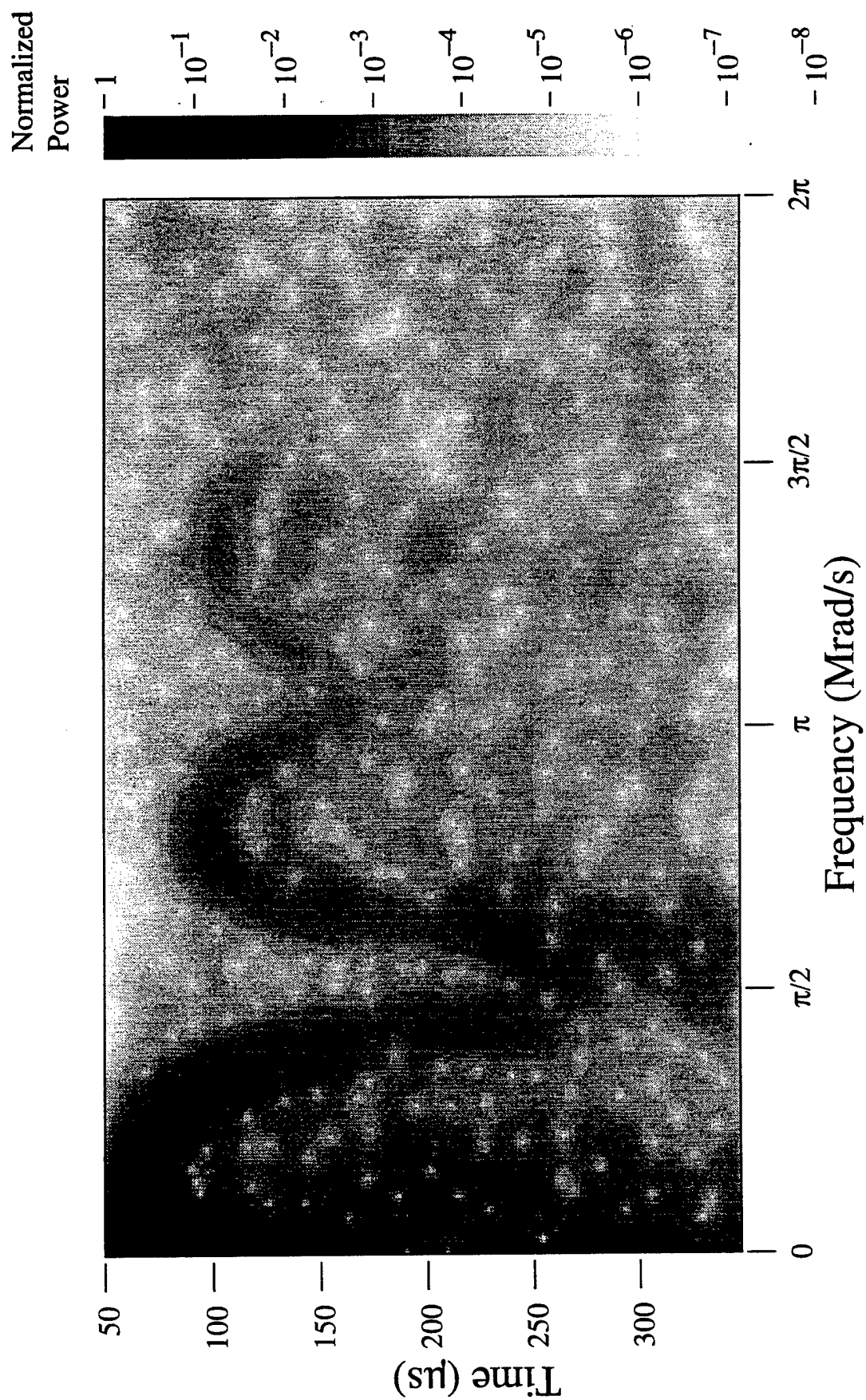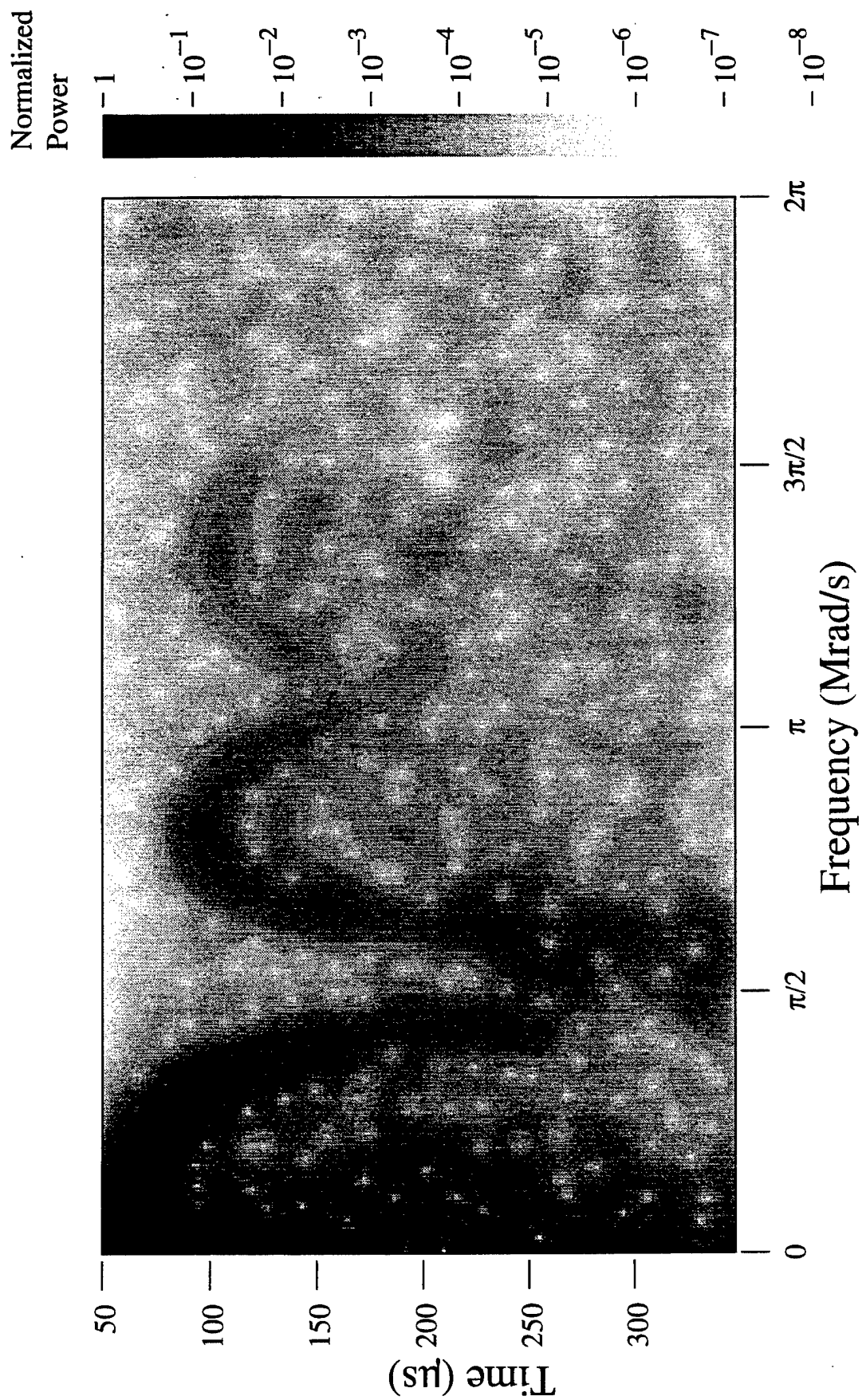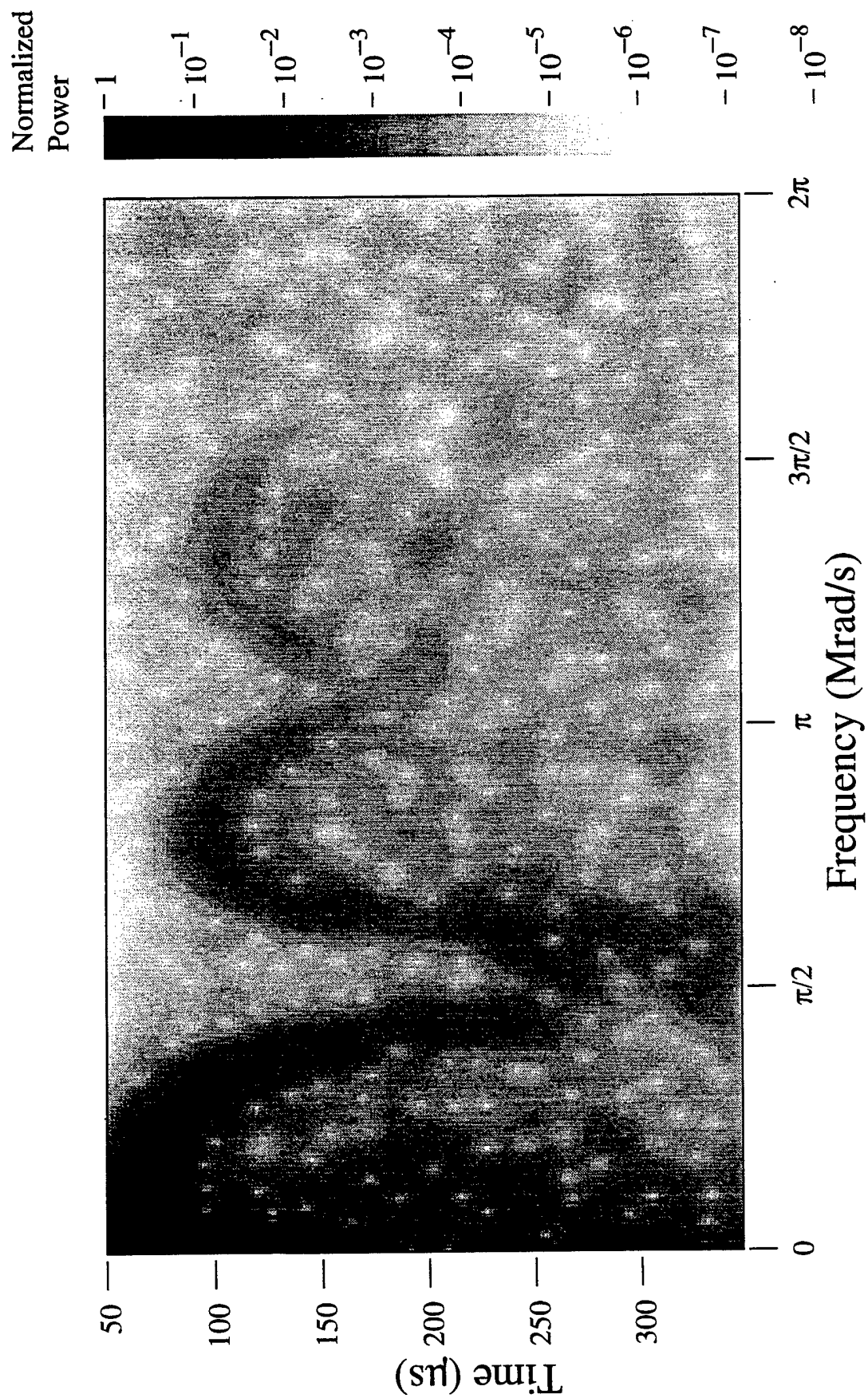
Figure A-6.   Numerical study: 10-μs Gaussian window.

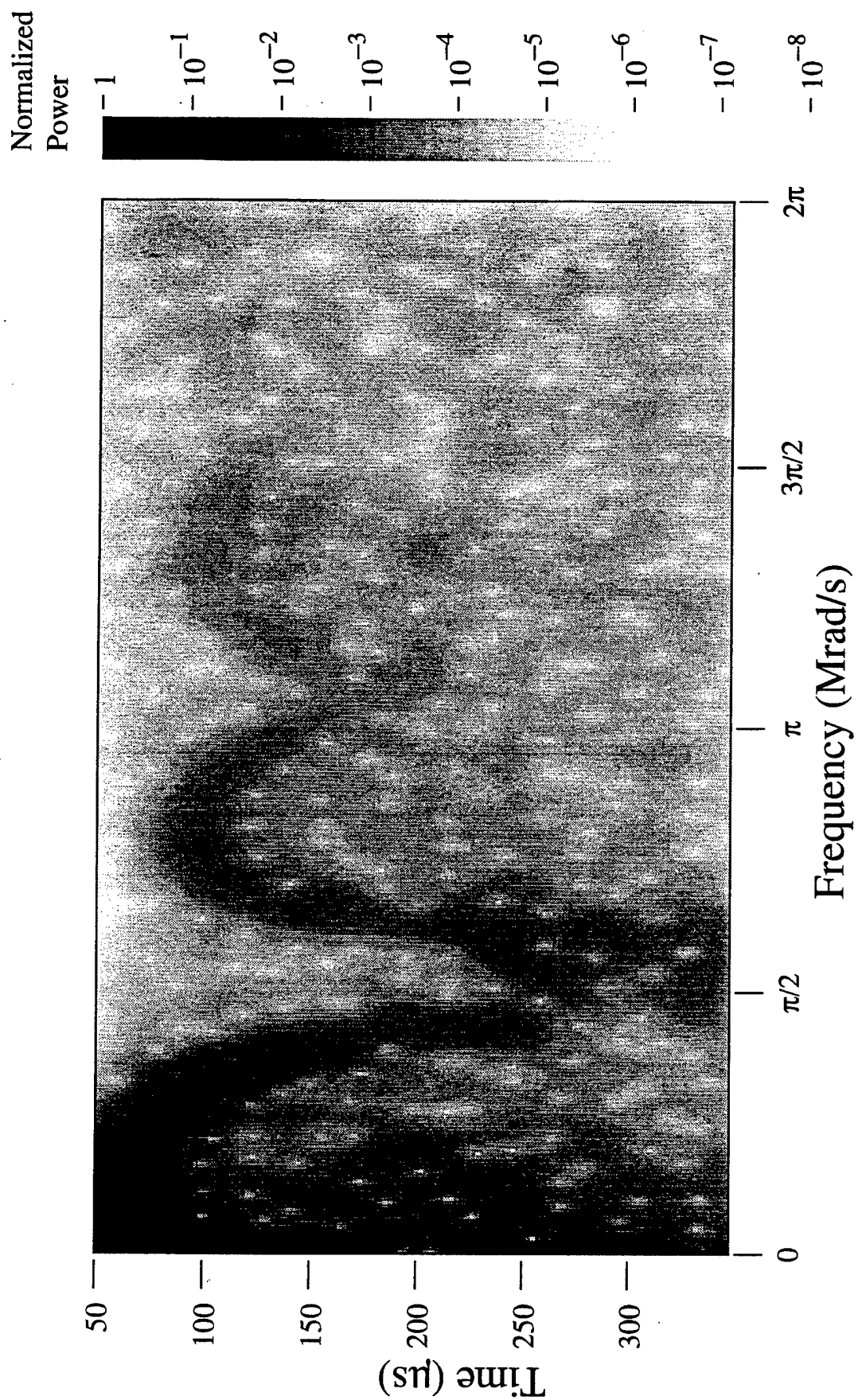Figure A-7.   Numerical study: 12-μs Gaussian window.
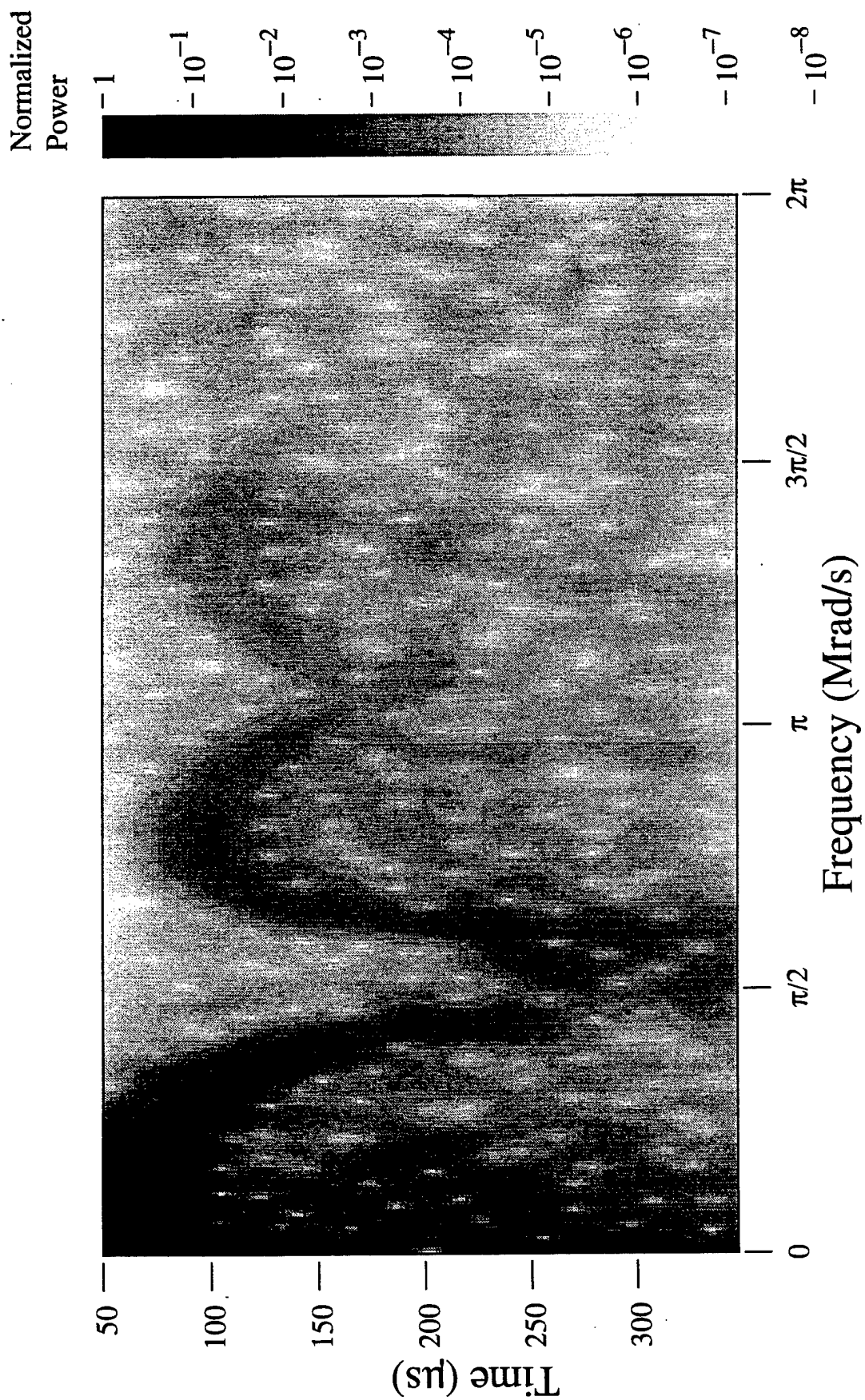
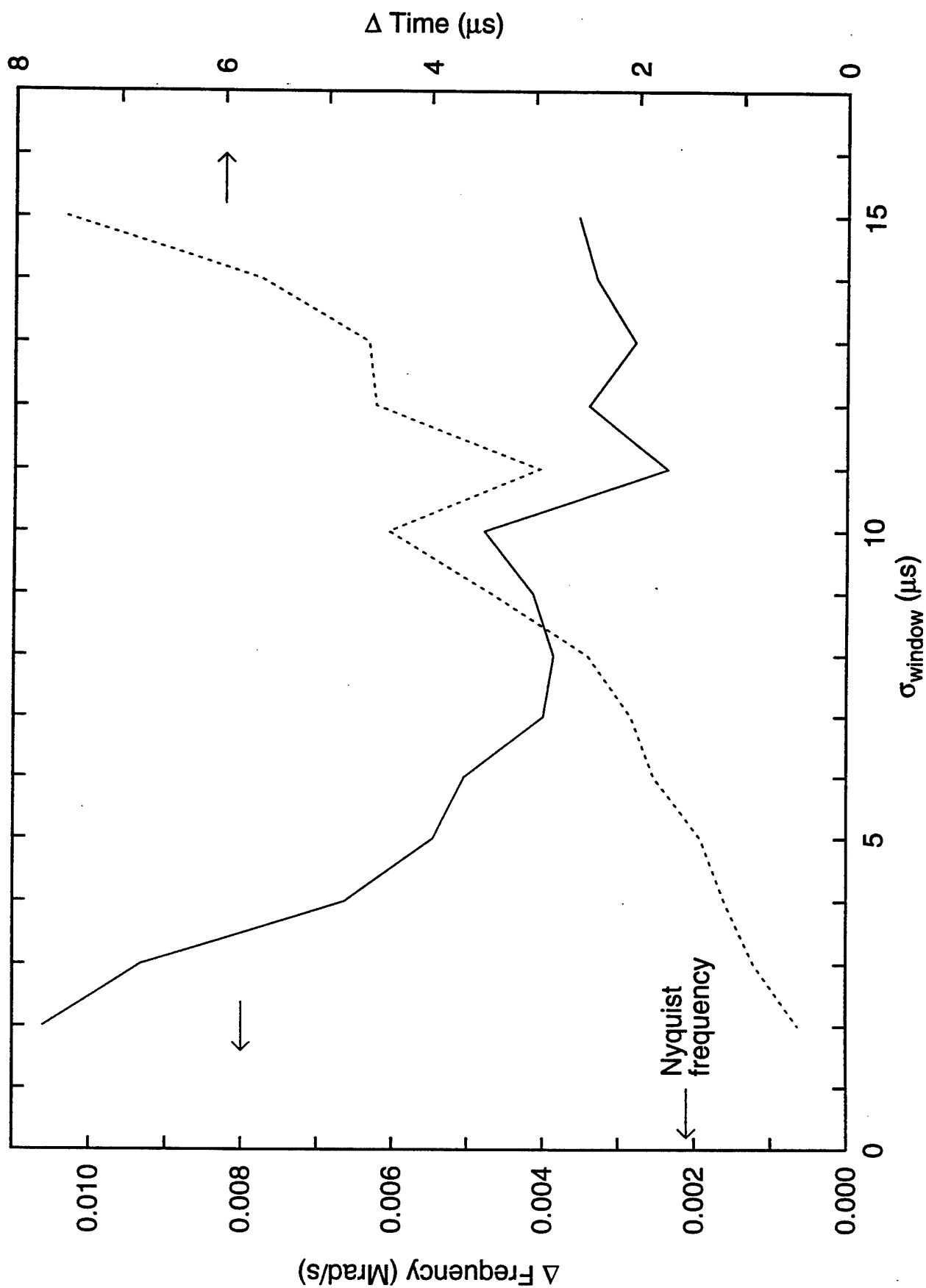Figure A-8.   Numerical study: 14-μs Gaussian window.

Figure A-9.   Gaussian window optimization using halfwidths of white spots.

APPENDIX B

THE ERRORS IN THE SEMI-EMPIRICAL DISPERSION CURVES

In this appendix, we will present the details of (1) how we check the gray scale results by analytical methods in the limit of small time and low frequency, and (2) how we estimate the error in the 'measured' group velocity curve and the corresponding semi-empirical phase velocity curve. The first is triggered by an artifact of the GWFT at low frequencies. But, until this artifact is understood analytically, it raises doubt in the numerical results as well as our interpretation of them. The second has to do with the treatment of errors from the experimental data and other sources.

Before we examine the artifact of the GWFT in the low frequency region, it is useful to review our definition of the ToA of a signal, or any time sequence involving a sharp rise in the front of the signal. The ToA of the signal, in a plot of amplitude versus time, is determined by first locating the point of steepest slope in the early rise of the signal. Then a tangent is drawn from that location to intercept the zero amplitude line. The time of intercept is taken to be the ToA for the signal. The time between the ToA and the peak of the signal is called the risetime. The time at the peak is called the ToA of peak power. The method for the ToA is a standard procedure that we apply to all the pulses that we analyze, using DISBAS or GIFT. It avoids the problems with determining exact arrival times when a small 'toe' appears in front of the sharp rise. [The origin of the small toe is unclear, but it is observed in many measured pulses, and it has been determined to be not electrical in origin (Coleman and Petersen, 1993).]

For a dispersed pulse, the ToA of the pulse is the ToA for the lowest frequencies, i.e. it is the time corresponding to zero phase for those frequencies. It is the ToA that must be used in determining the dispersion curve, **not** the ToA of peak power. We need a method to convert the time of peak power to ToA. In other words, we need an estimate of the risetime, therefore the ToA, for each time sequence. Recall the function $C(\omega,\tau)$. For each frequency ω there is a time-dependent function $C_\omega(\tau)$, where the subscript indicates fixed frequency. The ToA and the risetime for this function are determined the same way as for the signal itself. If the time sequence is a sine wave, the risetime is a quarter of the period of the sine wave. Therefore, depending on the character of the time sequence, we either apply a risetime correction or a quarter-cycle correction. Obviously we can use the theoretical first PC mode to 'fill in' the data in this region. We do not choose to do so because we want to derive the dispersion curve for group velocity assuming no prior knowledge of the theoretical PC modes.

First, we present a rationale that leads to the risetime correction. The need for this correction is depicted in Figure B-1. As can be seen, the times of peak power at the lowest frequencies are later than those at slightly higher frequencies. This behavior is not visible in Figure 3-3, but very obvious in the expanded scale of Figure B-1. Although it is a small difference, ~ 10 μs, it is big enough to be concerned with because one might erroneously interpret the delayed ToAs as the **physical** dispersion curve. Recall in Section 3 we choose to use the peak power arrival times to define the dispersion curve (based on $T(\omega) = D/C_g(\omega)$, where $T(\omega)$ is the ToA of peak power, D

is the distance from the pressure end of the bar to the measurement point, and $C_g(\omega)$ is the group velocity. If these peak power times were used directly as the ToAs, the derived dispersion curve would possess the nonphysical feature of decreasing dispersion with increasing frequency.

We demonstrate in Appendix A that narrowing the time window leads to better time resolution. The time delay in peak power arrival for the 2-μs window in Figure A-1 is uniform compared to that shown in Figure B-1. The improved time resolution removes the frequency dependence in the time delay of peak power ToA, but does not remove the risetime between the ToAs and the times of peak power. The frequency-dependent peak power times calculated with the 2-μs window almost coincide with that of the raw signal. Furthermore, when the procedure for deriving the ToA from these time sequences is applied, the resulting ToAs for the $C_\omega(\tau)$ in this low frequency region agree with that of the raw signal to within the size of the window. For this reason, we call this time delay an "artifact" of the GWFT method. However the improved time resolution is accompanying by poor frequency resolution. Thus we choose the optimum 10-μs window, and are left with the necessity of removing the artifact of frequency-dependent risetimes. It is important to understand the nature of the image in this region based on this choice. To further understand the nature of the image in this region, we performed the following theoretical exploration.

In theory, using the time of peak power arrival should work well at high frequencies, but at low frequencies the time of peak power arrival can be much larger than the time of arrival of the frequency component; the discrepancy can be of the order of a quarter of the period of that component. Recall Equation A.1,

$$C(\omega,\tau) = \int_{-\infty}^{\infty} \phi(t)g(t-\tau)\exp(-i\omega t)\,dt \qquad \text{(B.1)}$$

which can be written as

$$C(\omega,\tau) = \int_{0}^{\infty} \phi(t)g(t-\tau)\exp(-i\omega t)\,dt \qquad \text{(B.2)}$$

because $\phi(t) = 0$ for $t < 0$. For a given low frequency ε_ω, we are interested in the early time part of the function $C(\varepsilon_\omega,\tau)$ where for dispersed signals, the low frequencies are at the front of the pulse. For this analysis the function $\phi(t)$ is approximated by a step and a ramp. Because the Gaussian decreases rapidly as t increases, we will neglect the contribution to the integral at large times. In the case of a step with for $t > 0$ and zero otherwise, the integral $C(\omega,\tau)$, is

$$C(\varepsilon_\omega, \tau) = K \int_0^\infty g(t-\tau) \exp(-i\varepsilon_\omega t) \, dt \qquad (B.3)$$

where we have replaced the frequency ω by ε_ω representing a small value, or low frequency. Upon substituting $s=t-\tau$,

$$C(\varepsilon_\omega, \tau) = K \exp(-i\varepsilon_\omega \tau) \int_{-\tau}^\infty g(s) \exp(-i\varepsilon - \varepsilon_\omega s) \, ds$$

$$= K \exp(-i\varepsilon_\omega \tau) \left[\int_{-\tau}^0 g(s) \exp(-i\varepsilon_\omega s) \, ds + F(\varepsilon_\omega) \right] \qquad (B.4)$$

where

$$F(\varepsilon_\omega) = \frac{1}{2}\exp(-\varepsilon_\omega^2 \sigma^2/2) + iH(\varepsilon_\omega) \qquad (B.5)$$

and

$$H(\varepsilon_\omega) = \frac{1}{\sqrt{2\pi}} \sum_{k=1}^\infty \frac{(-\varepsilon_\omega^2 \sigma^2)^k}{(2k-1)!!} \qquad (B.6)$$

and !! means factorial for every other integer (in this case odd integers are included). Inside the brackets in Equation B.4 there are two terms, a time-independent term and a transient term which starts from zero at $\tau=0$ and increases to $F^*(\varepsilon_\omega)$. The transient term contains both real and imaginary parts that are both oscillatory, meaning that when we take the product of $C(\varepsilon_\omega, \tau)$ and its complex conjugate to obtain the power, the resulting expression will also be oscillatory. The observation we make in Appendix A that the function $C(\omega, \tau)$ is strongly affected by the Gaussian function is substantiated by this idealized step signal if we recognize the real part of the second term in the bracket is simply half of the transform of a Gaussian function $g(t)$. Assuming the measured signal $\phi(t)$ can be approximated by a summation of positive and negative steps with time delays, this equation suggests that the GWFT of the signal is controlled by the Gaussian function and its transform. This is true except where the transient term dominates. [Note: This may be the reason why the white spots tend to avoid the high power regions. See Figure C-7 in Appendix C.] Recall from Equation A.4, the transform of the translated Gaussian $g(t-\tau)$ is

$$G(\varepsilon_\omega) = \exp(-i\varepsilon_\omega \tau)\exp(-\varepsilon_\omega^2 \sigma^2/2) \qquad (B.7)$$

Note that the translation $(t-\tau)$ in the function $g(t-\tau)$ added an oscillatory multiplier to the transform of the Gaussian. At very early times, the transient term in Equation B.4 can be

approximated by $g(\varepsilon_\tau/2)\exp(-i\varepsilon_\omega\varepsilon_\tau/2)*\varepsilon_\tau/2$ which contains a τ-dependent oscillatory part with frequency ε_ω with a Gaussian multiplier. If the Gaussian window is narrow compared to $2/\varepsilon_\omega$, the Gaussian will give the function a first peak. If the step function has a delay, the Gaussian-produced peak will delay with it. If the window is wide compared to $2/\varepsilon_\omega$, the first peak in C will be due to the oscillatory part. In any case, the Gaussian guarantees that the time function at each frequency begins with a zero value in both the real and the imaginary parts. To the extent that a measured signal can be approximated by a sum of steps with delays, this Gaussian multiplier assures that the front of the pulse will be reproduced to the resolution of the width of the window. This effect is in agreement with the image using the 2-μs window in Figure A-1. The frequency-dependent time delay in the arrival of peak power at very low frequencies is definitely a function of the window width until the width is sufficiently small to make the ToA's uniform. For a given σ, however, the delay is largest at the fundamental frequency, but decreases with increasing frequency.

We arrive at essentially the same behavior when a ramp is used for the signal $\phi(t)$ in Equation A.2. For $\phi(t)=At$ (for $t>0$, zero otherwise), we obtain the following

$$
\begin{aligned}
C(\omega,\tau) &= A \exp(-i\omega\tau) \int_{-\tau}^{\infty} (s+\tau)\, g(s)\, \exp(-i\omega s)\, ds \\
&= A \exp(-i\omega\tau) \int_{-\tau}^{\infty} s\, g(s)\, \exp(-i\omega s)\, ds \qquad\qquad \text{(B.8)} \\
&\quad + A \tau \exp(-i\omega\tau) \int_{-\tau}^{\infty} g(s)\, \exp(-i\omega s)\, ds
\end{aligned}
$$

The last integral is identical to the integral in Equation B.3. The only difference is the coefficient in front of the integrals. The first integral can be integrated by parts giving

$$
C(\omega,\tau) = A g(\tau)\sigma^2 + A\exp(-i\omega\tau)(\tau+i\omega\sigma^2) \int_{-\tau}^{\infty} g(s)\exp(-i\omega s)\,ds \qquad \text{(B.9)}
$$

From this equation and Equation B.7, we expect the power of the function $C(\omega,\tau)$ for the ramp to be oscillatory also. For any signal, as long as the front of the signal can be represented by a step or a ramp, the behavior will be similar. However, in order to quantify the time difference between ToA and time of peak power, these equations will have to be solved. As can be seen, these integrals cannot be easily evaluated even in this small-time low-frequency regime. Since we already derived the general trends of $C(\omega,\tau)$ from them, and these trends agree with the numerical solution given by the gray scale images, it is a lot easier to go directly to the numerical solution to make the adjustments based on the power plot of the measured signal.

We return to Figure B-1. As can be seen, the time delay is larger at low frequencies but smaller at slightly higher frequencies. Apparently, the time to peak power at low frequencies is strongly

B-4

affected by the peak in the measured signal. From Figure 3-4, the raw signal has a rise time of ~ 10 µs. The peak power arrival times given in Figure B-1 match that quite nicely. This fact is another indication that the front of the raw signal is dominated by low frequencies. At slightly higher frequencies, the time of peak power arrival is affected by the higher frequency oscillations, which tends to move the first peak to an earlier time. Although this behavior of the peak power arrivals does not agree entirely with the trend obtained from the step and the ramp signals (because those analytical functions do not contain a peak), the differences are understandable from the nature of the measured signal.

Figure B-2 shows the corrected ToA data. The theoretical arrival times in this figure are generated using a pulse time of arrival of 65.5 µs and a bar velocity of 0.5285 cm/µs. At the lowest frequencies, there is a tendency to overcorrect because the duration of a quarter of the period is very long. At these very low frequencies ($< \pi/8$ Mrad/s), we use the 2-µs window results (Figure A-1) to determine the ToA for a given frequency. As mentioned in the context of Equation B.7, for a very narrow window, the front of the pulse will be reproduced by the Gaussian; the arrivals of the peaks of the low frequency components, $C(\varepsilon_\omega, \tau)$, are synchronized. The procedure for determining the ToA of a given frequency is the same as that for the raw signal; but, in place of the raw signal we use the time sequence for each $m\omega_o$. The ToA of the synchronized low frequency components is 64.6 µs, which agrees with the ToA of the raw signal determined the same way (65.5 µs) to within 1 µs. Thus, wherever the quarter cycle correction overcorrects, we set the ToA equal to the ToA found from the 2-µs window for that frequency. The error introduced by the slightly earlier arrival (64.6 µs) is included in the error analysis to be discussed next. At slightly higher frequencies, the corrections are smaller, and they do not lead to ToAs earlier than the ToA of the pulse. As the frequency increases, the quarter-cycle correction decreases rapidly as expected. [If we are willing to use the theoretical first PC mode to correct the data, we will apply it to frequencies below $3\pi/16$ Mrad/s. From Figure B-2, at this frequency the peak power ToA curve overlays the one derived from the first PC mode.]

Next, we address several sources of error that can affect the derived phase and group velocity curves. These fall into three general categories: the properties of the bar, the accuracy of calculations based upon the theory, and the processed data.

There are three parameters characterizing the bar that enter the calculations: the diameter of the bar, the position of the sensor, and the bar velocity. Of these, the last is by far the least certain.

The theory enters the calculations through the frequencies where propagation changes abruptly from one mode to the next. [Recall that the abrupt change from one mode to the next is an assumption. The derived peak power curve does not clearly identify the frequencies where the changes occur, so we use the theoretical values.] As these transition points must be found numerically, there is some small uncertainty about exactly where they occur.

The processed data have three major sources of error: the time of peak power at each frequency, the assumed quarter-cycle correction at each frequency, and the pulse arrival time. Of all of these, none can truly be characterized as Gaussian in nature, and several are systematic. This

makes a formal error analysis difficult. We have chosen a Monte Carlo approach. Each error is treated as uniformly random over some fixed range. The phase velocity is then computed many times, each with an independently selected set of parameters. The computed phase velocities from each sample are saved for later statistical analysis. With several error sources entering the problem in non-linear ways, the resultant phase velocity at each frequency appears to obey a Gaussian probability distribution, an outcome expected from the Central Limit Theorem (see Meyer, 1975).

We ignore the uncertainty in the time of peak power that occurs at those frequencies where there are multiple peaks of nearly equal power. This is most severe at frequencies near the bottom of the valleys. We also ignore errors in the bar dimensions, as these are usually well controlled experimentally, and they should be small compared to the error in the bar velocity.

We select the bar velocity from the range 0.5240 to 0.5300 cm/μs, the arrival time from 62 to 66 μs, the error in each time of peak power from -1 to 1 μs, the scaled frequency of the break between modes 1 and 2 from 0.3630 to 0.3638, and between modes 2 and 3 from 0.6470 to 0.6482. We include the effects of the uncertainty in the delay by using a fraction of the $\pi/2$ correction, chosen from 0.5 to 1.0 independently at each frequency.

The results are shown in Figure B-3. The error in the group velocity is small at zero frequency, because there $C_g = C_o$ and thus has only one source of error, and grows quickly as the uncertainty in the quarter-cycle correction predominates. As the frequency increases, the quarter-cycle correction error diminishes, and by about scaled frequency 0.2 the error is dominated by the errors in the arrival time and the peak power time.

The phase velocity is found from the integral of the group velocity weighted by the inverse square of the wavelength (see Equation 3.2). Thus the phase velocity is smoother than the group velocity -- much smoother near the mode transitions. [Of course, the raggedness in the group velocity curve near the mode breaks is not lost; it will return when the phase velocity is used to remove dispersion, as that process implicitly uses the derivative of the phase velocity.] On the average the relative width of the 95% confidence band is about ±1.15%, which translates to a standard deviation of 0.6%.

Given the arbitrariness with which we assigned numerical values (and the uniform probability density function) to the various errors, the calculated uncertainty band cannot be considered definitive. However, we do feel that the values chosen for the calculation are reasonable, and the resulting 95% confidence band should be representative of a more rigorous analysis.

The behavior of the phase velocity in the low-frequency regime has been well-established by previous research (Kolsky, 1963). Thus the crudity of our quarter-cycle correction should not lead to any loss of confidence in this part of the dispersion curve. The precision of our windowed transform analysis is better at higher frequencies where the character of the dispersion has not been previously determined empirically.
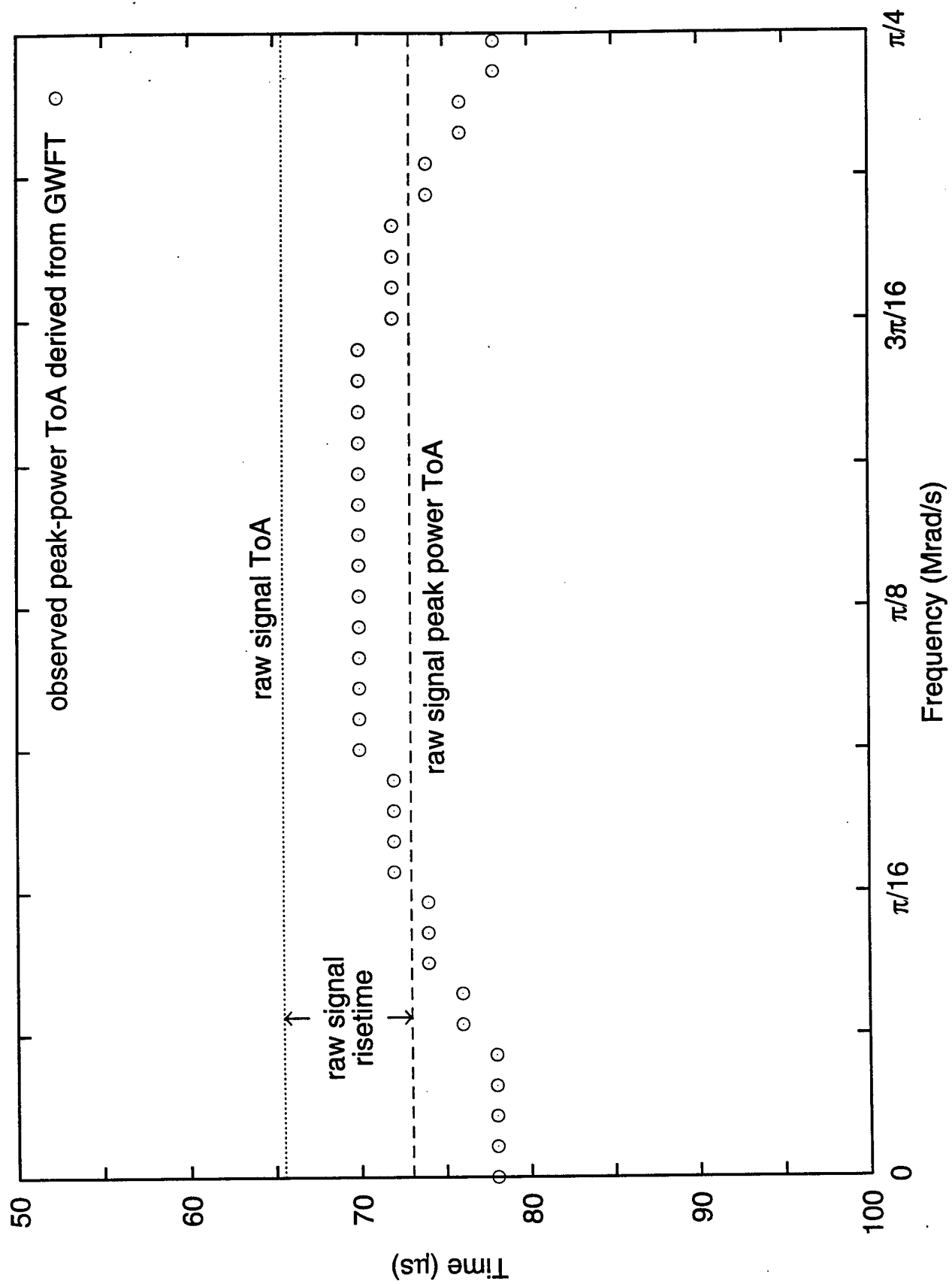
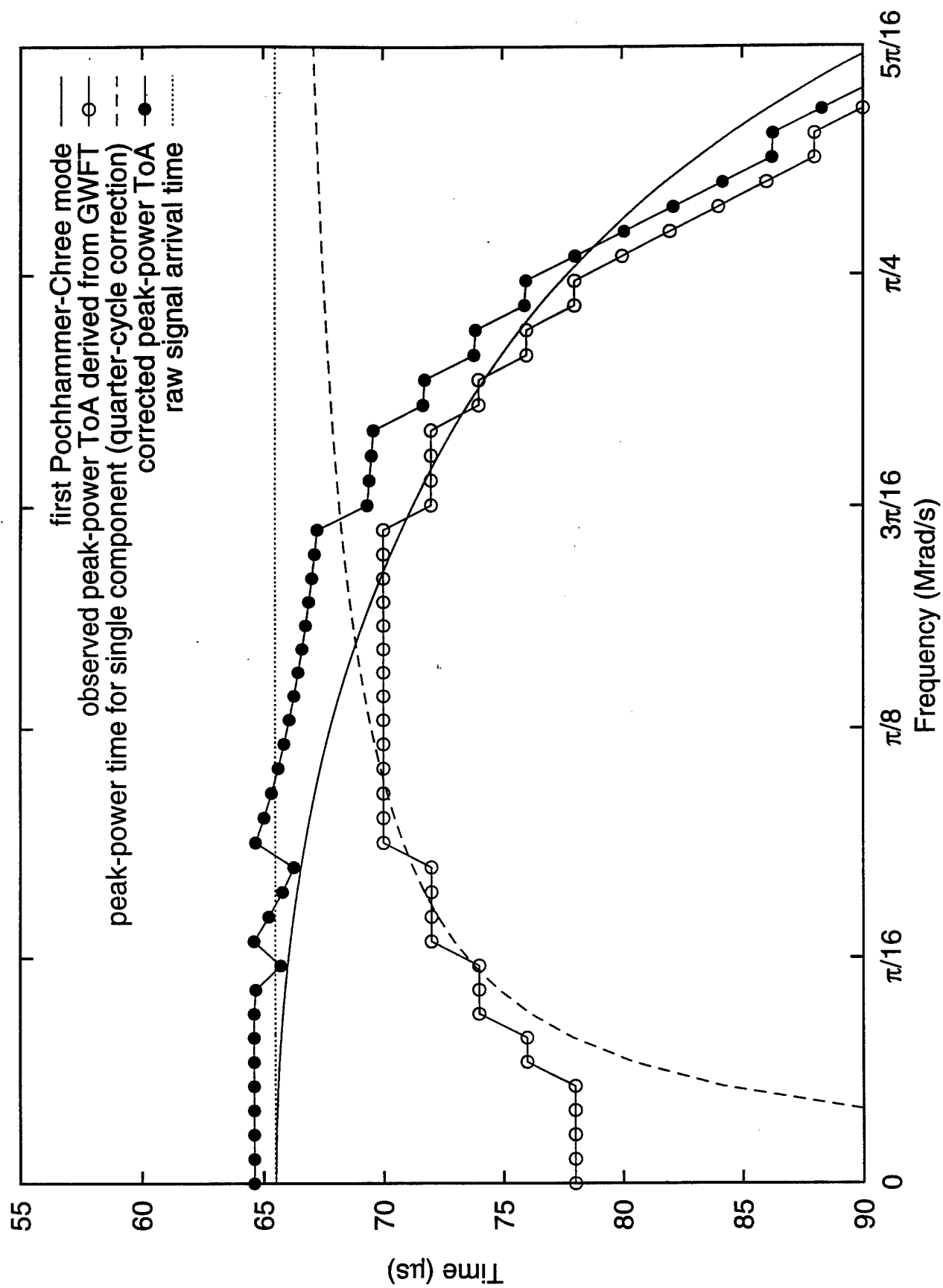Figure B-1.   Peak power arrival times for the low frequency components.

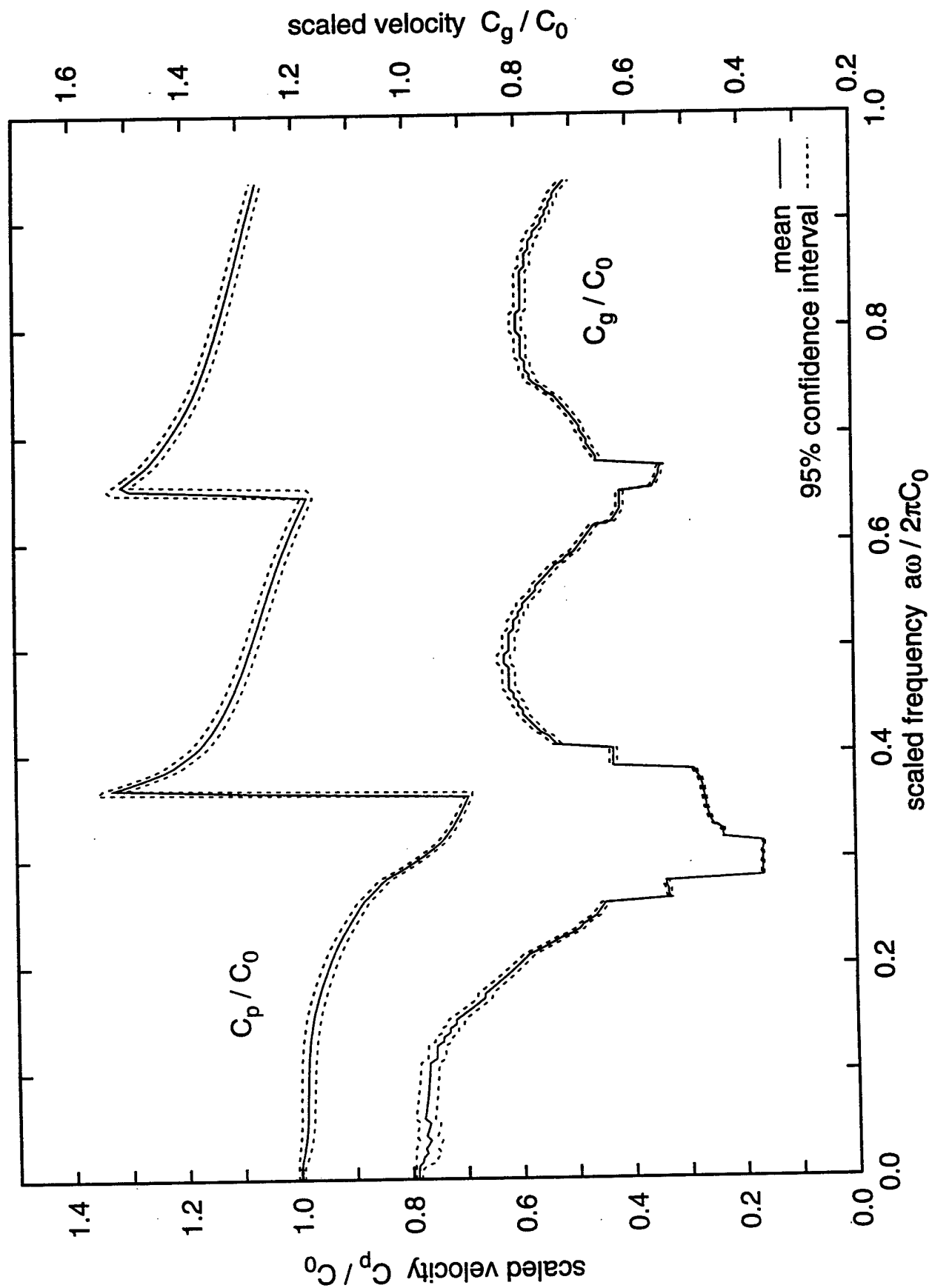Figure B-2.   Adjusted arrival times for the low frequency components.

Figure B-3.   The semi-empirical dispersion curves and their 95% confidence bands.

APPENDIX C

AN EXPLORATION OF OTHER WAYS TO REPRESENT THE IMAGE

Throughout this report, we have adopted one way of presenting the C_{mn} -- the gray scale plot of the power. The plot of the power is the conventional way to display complex quantities such as the C_{mn}, but there are other ways of displaying the ToA curve. We have explored other avenues, which we discuss here. The motivations for this exploration are: (1) to gain further understanding of the dispersive phenomena involved, (2) to produce comparable results to contrast with those already obtained, (3) to gain more confidence in the validity of the numerical solution, and (4) to explore ways of deriving a more accurate dispersion curve.

Figure C-1 and C-2 are gray scale images of the real and imaginary parts of the C_{mn}. Although the images are somewhat confused by oscillations, the signature of the ToA curve is discernible. This means that we do not have to use the power to derive the signature of the dispersion modes. In the text and the appendices we have mentioned the white (or light gray) spots on the gray scale plot on Figure 3-3. They have been used as an indicator for the resolution in Appendix A, which led to the choice of the optimum window. Figure C-3 shows the location of the white (or light gray) spots on Figure 3-3, shown in black on this figure. The region where the ToA curve lies is not clearly visible. In fact, these black dots appear to have a uniform density across the plot. This means that using them as an indicator for the resolution will not over- or underemphasize any particular region in the plot. We can make the ToA curve more apparent by enlarging the spots, which can be thought of as approximating the density of the spots. In Figure C-4 and C-5 each spot has been replaced by a rectangle of constant size and grayness. In regions where the spot density is high several rectangles overlap, resulting in dark patches. Similarly in Figure C-6 and C-7 each spot has been replaced by a two-dimensional Gaussian. Again overlapping regions produce dark areas indicative of higher spot density. The smaller Gaussians (Figure C-7) produce a plot that shows clearly that the spots tend to avoid the region containing the ToA curve. Figure C-8 and C-9 show the local total variation (LTV) in the real and imaginary parts of the C_{mn}. The LTV is defined as the sum of the absolute value of the difference between values at points adjacent in each direction. The size of the local region used in constructing the figures is the same as the large rectangles of Figure C-5. The plots are smoothly varying because each point has been replaced by the LTV of the region surrounding the point. If one were interested in obtaining an image without the confusion of the white spots, an LTV plot would be suitable.

Each of these approaches brings out the ToA curve to one degree or another, but our first impression is that none of them leads to any interpretation of the data other than that reached from the gray scale plots of the power. The fact that all these approaches produce essentially the same image suggests that the observed ToA curve from these images is essentially independent of the method used to extract it, which in turn suggests that the ToA curve is an intrinsic physical property of the measured signal. This finding increases our confidence in the results and the interpretations presented in the text.
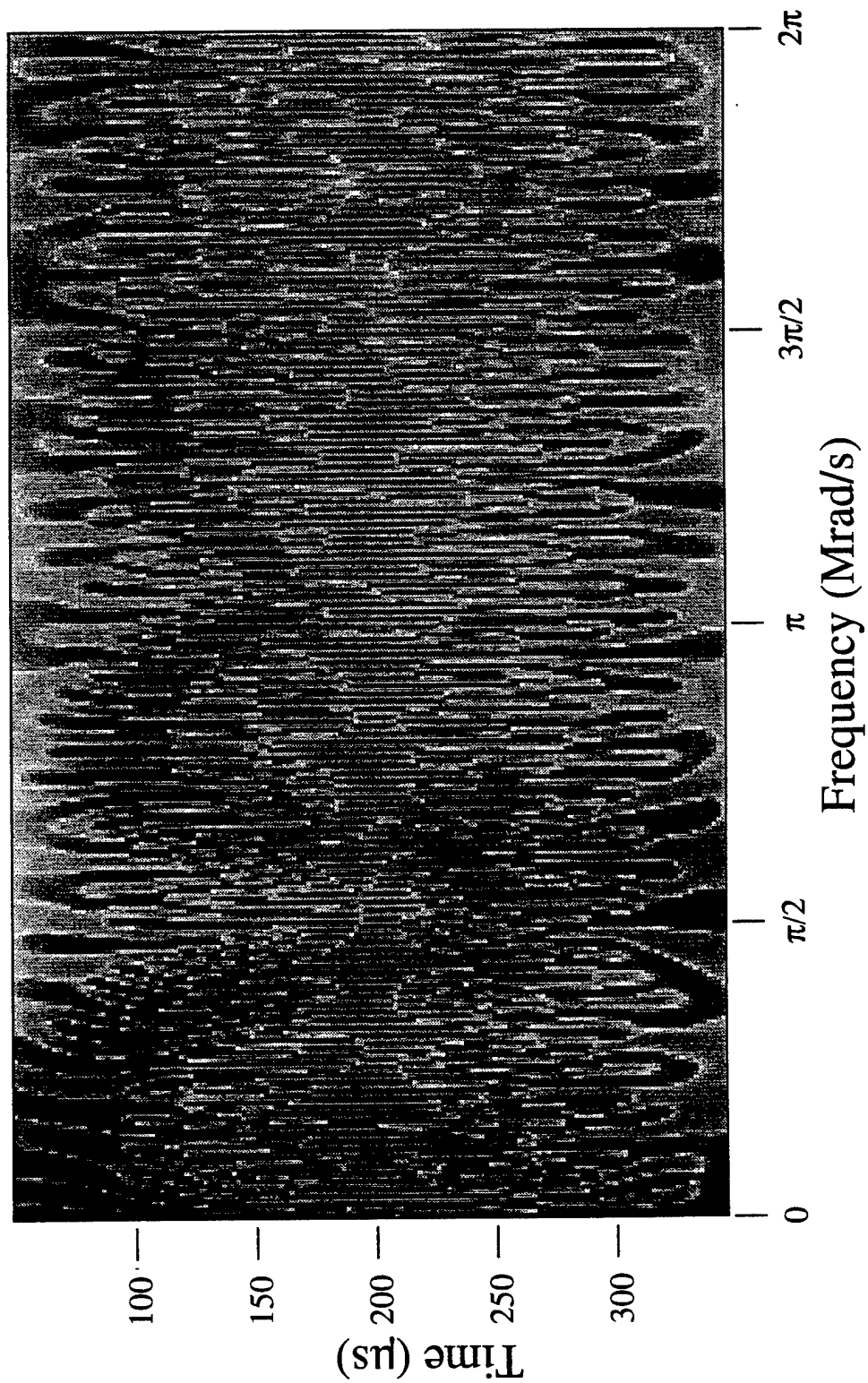
Figure C-1. The real part of C_{mn} derived from the 1/2-inch bar record (Darker regions are positive C_{mn}; lighter regions are negative C_{mn}).
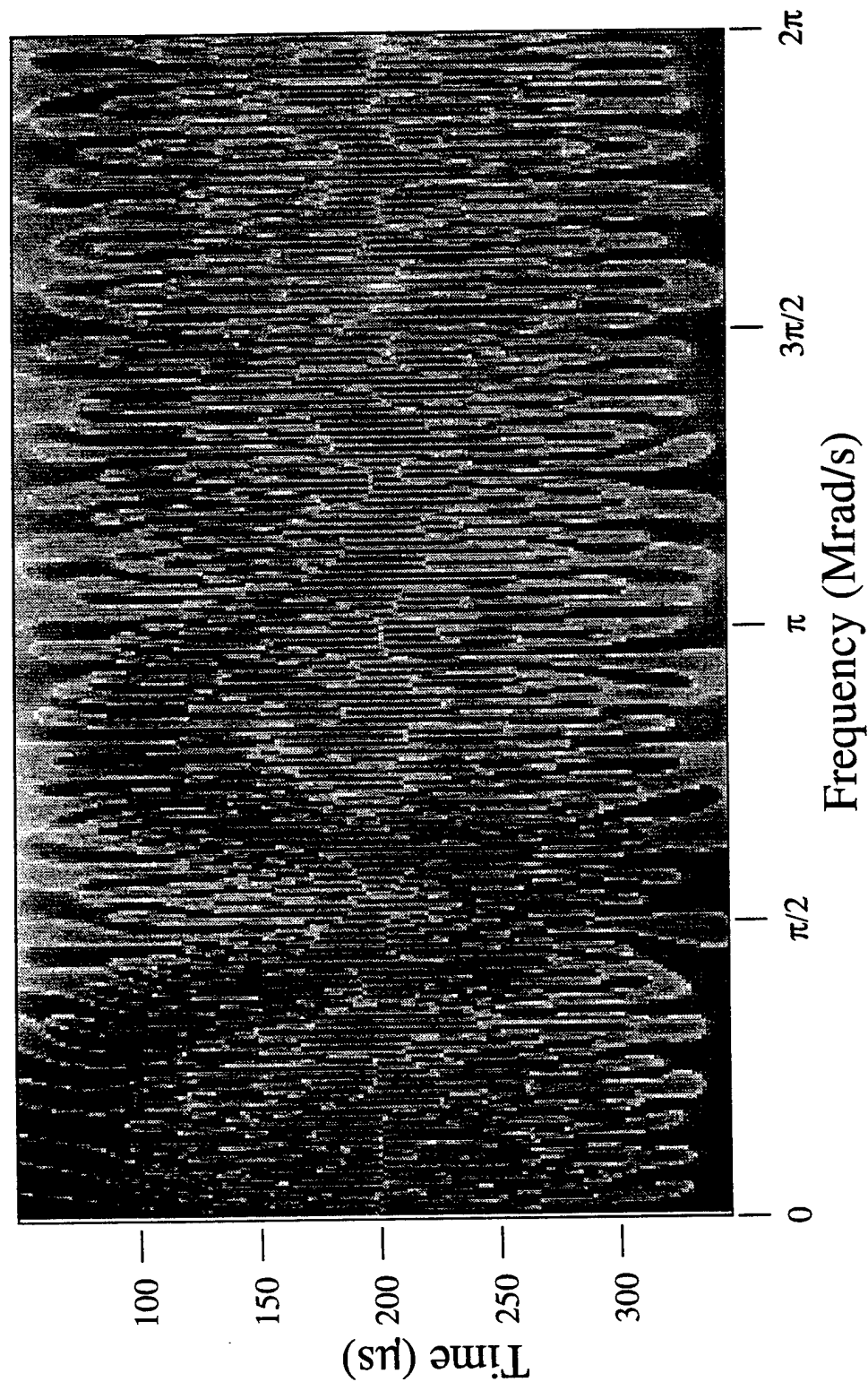
Figure C-2. The imaginary part of C_{mn} derived from the 1/2-inch bar record (Darker regions are positive C_{mn}; lighter regions are negative C_{mn}).
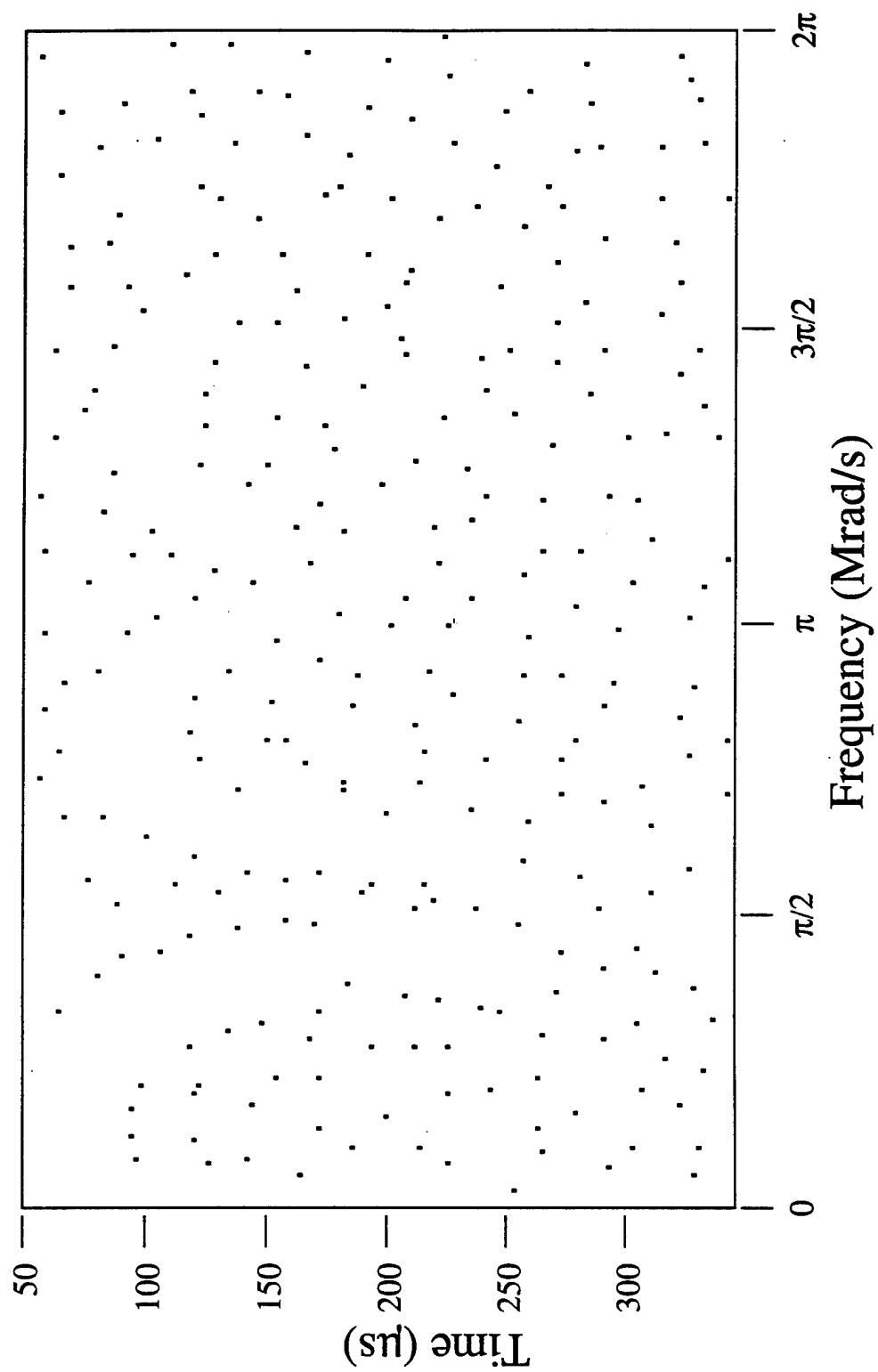
Figure C-3.   The white spots from the gray scale image in Figure 3-3.
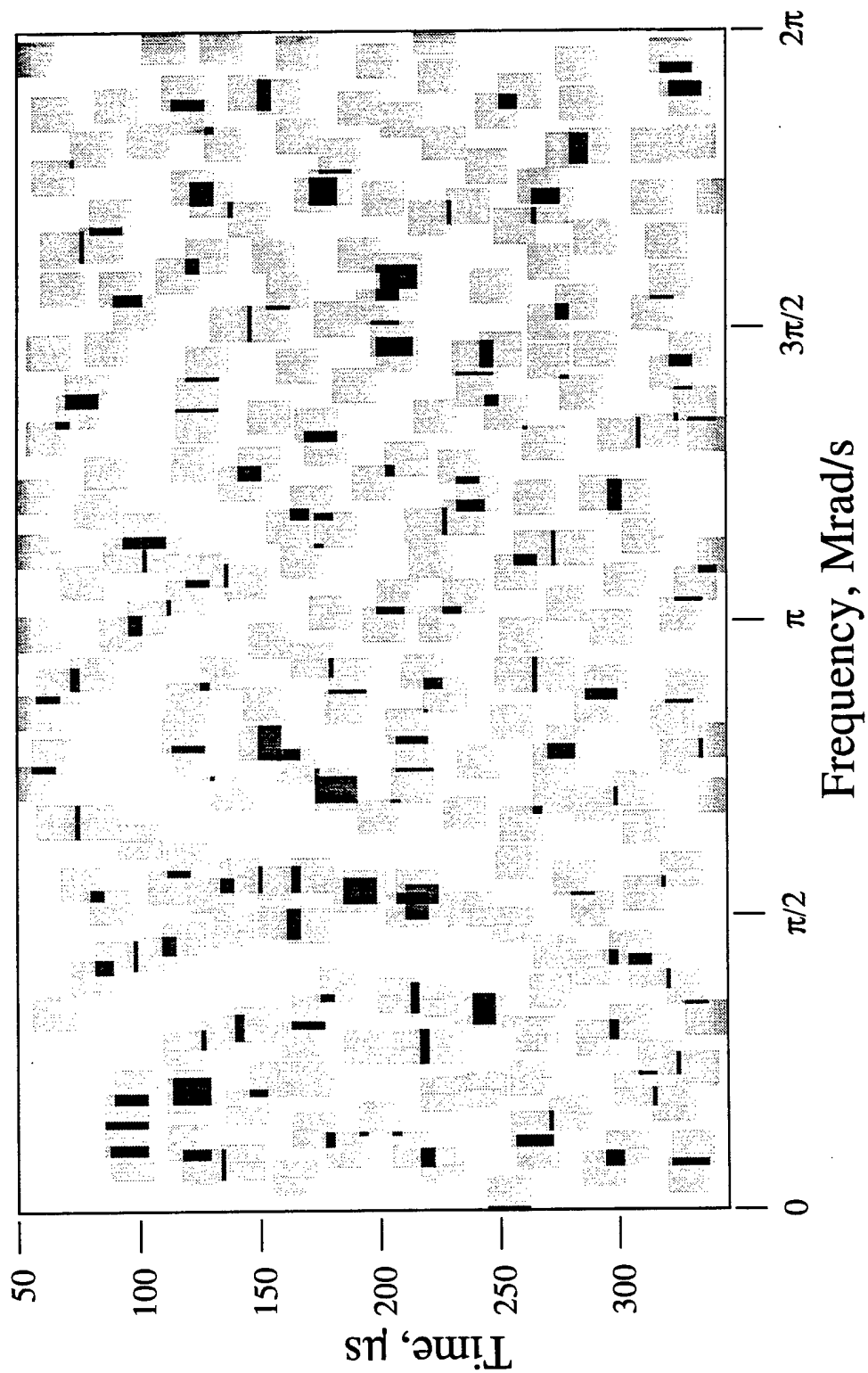
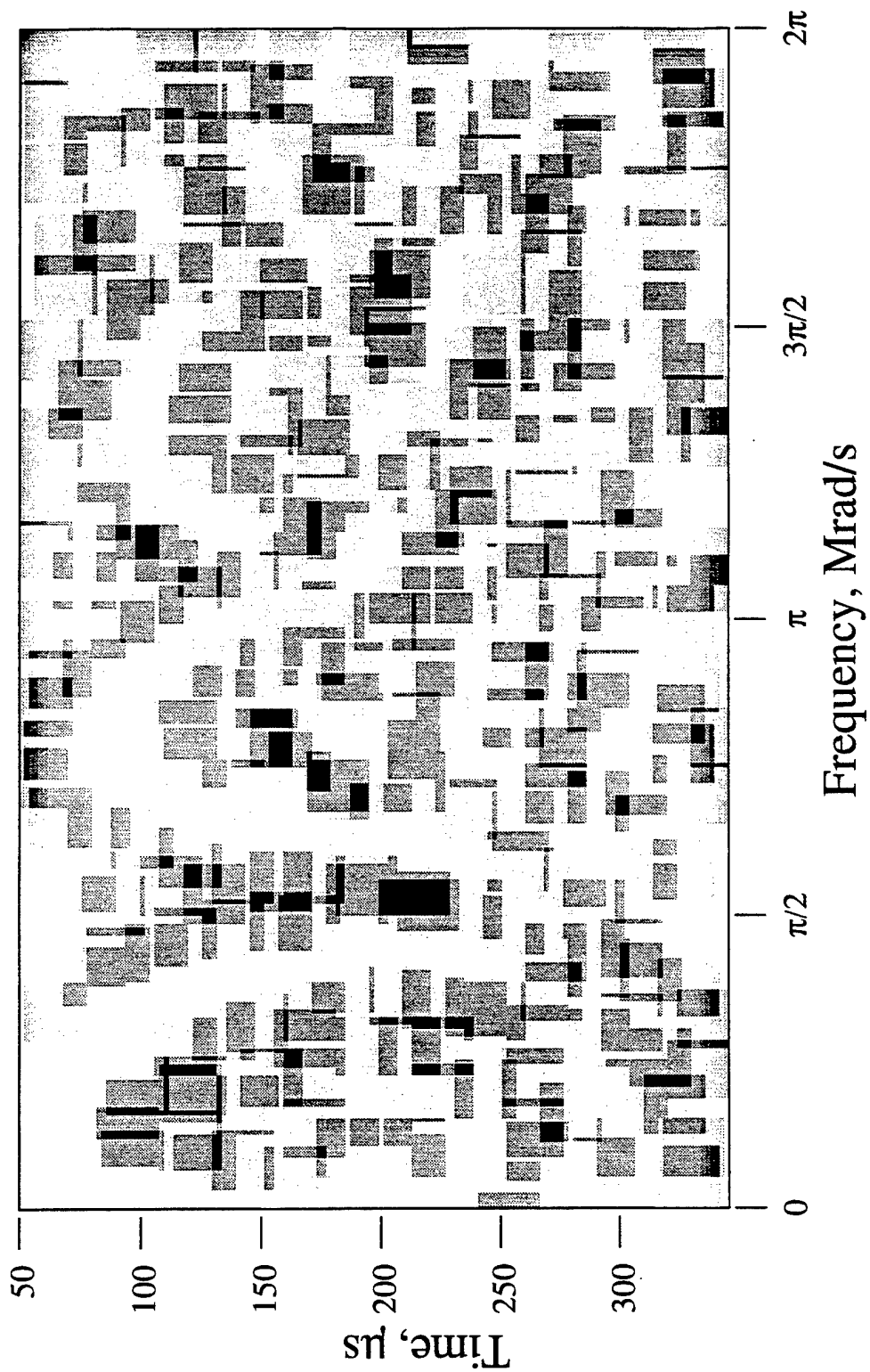Figure C-4.   The enlarged black spots showing the ToA curve.

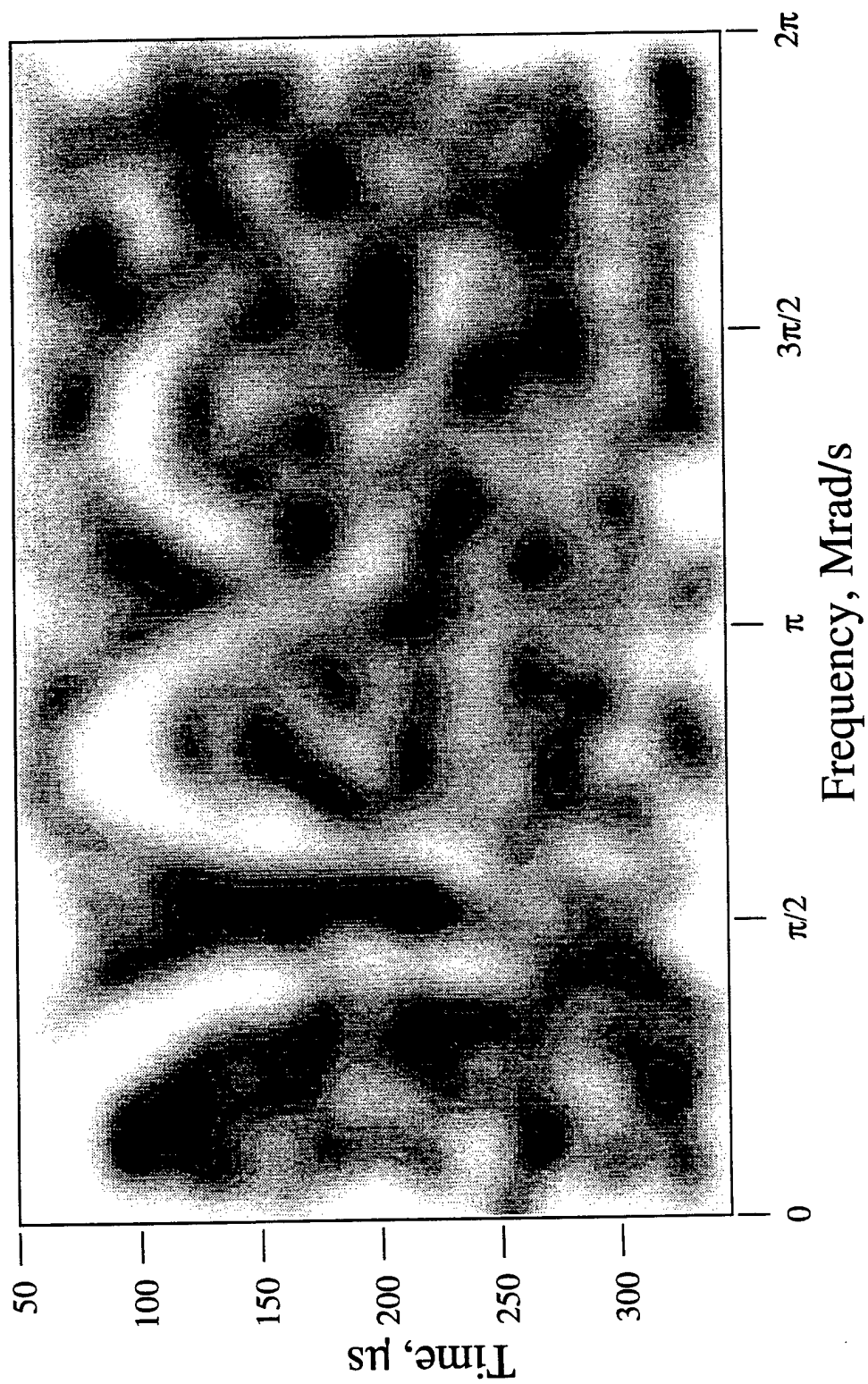Figure C-5.   The further enlarged black spots.

Figure C-6.   Black spots enlarged by a two-dimensional Gaussian with large windows
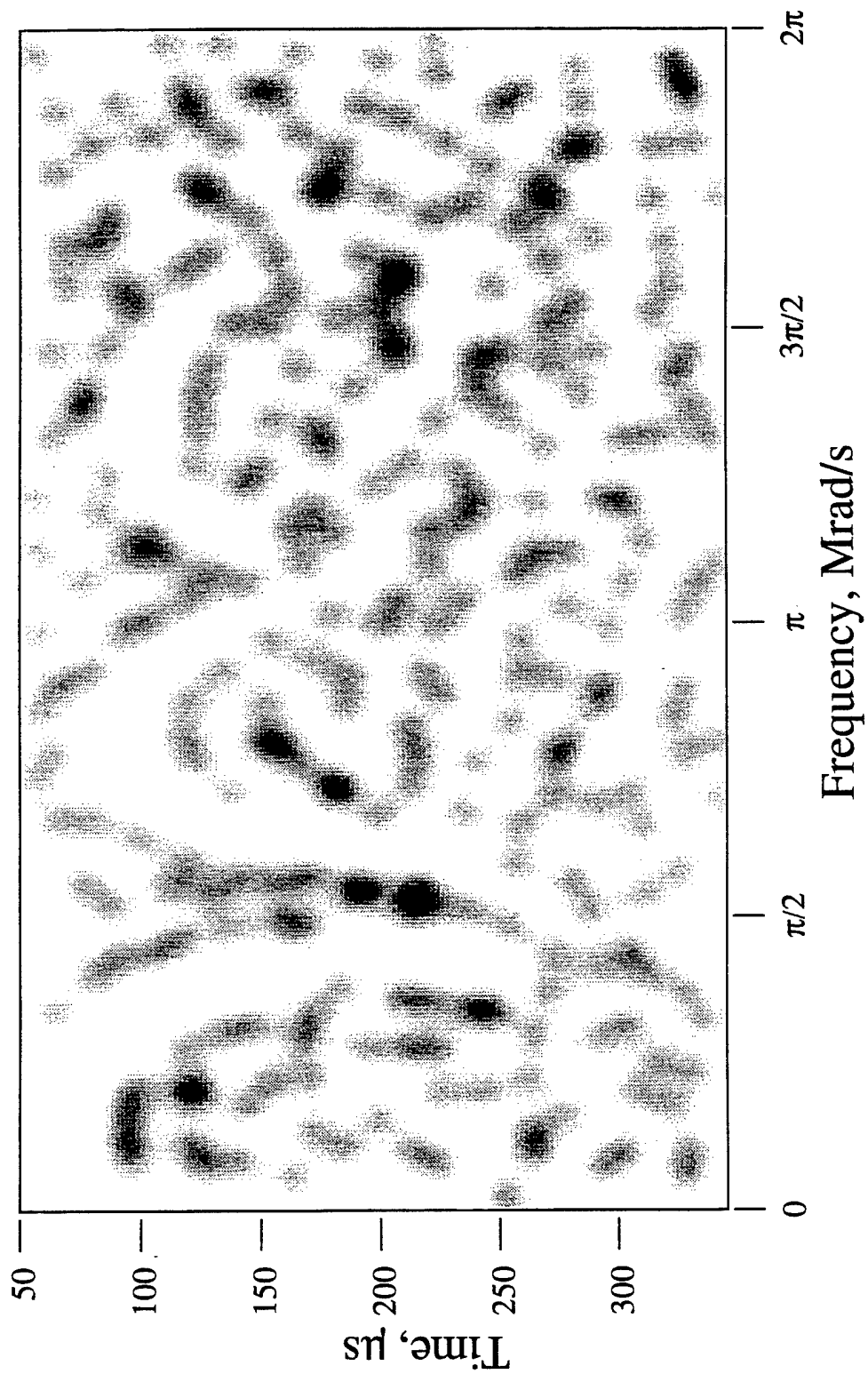
Figure C-7.   Black spots enlarged by a two-dimensional Gaussian with small windows.
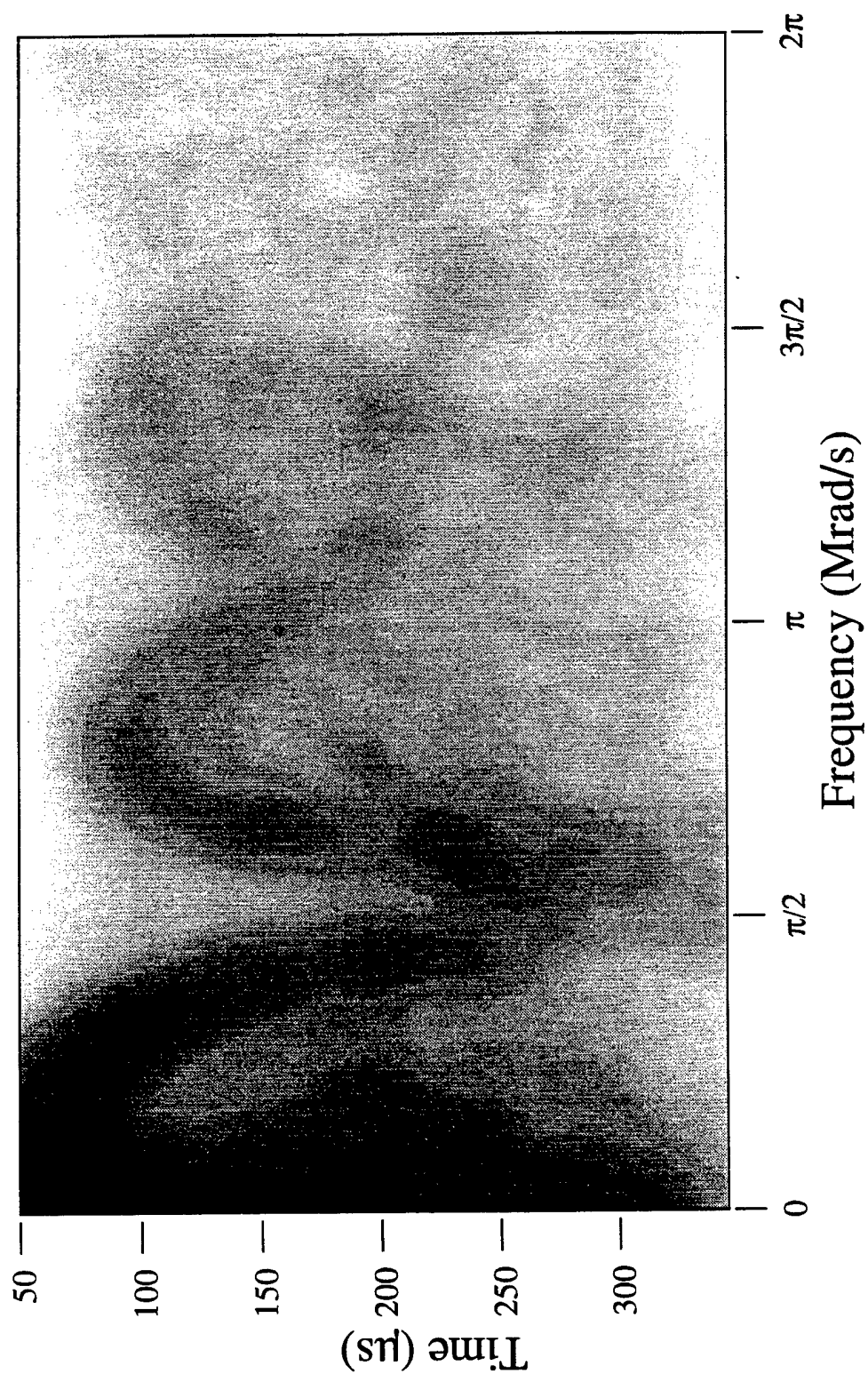
C-8

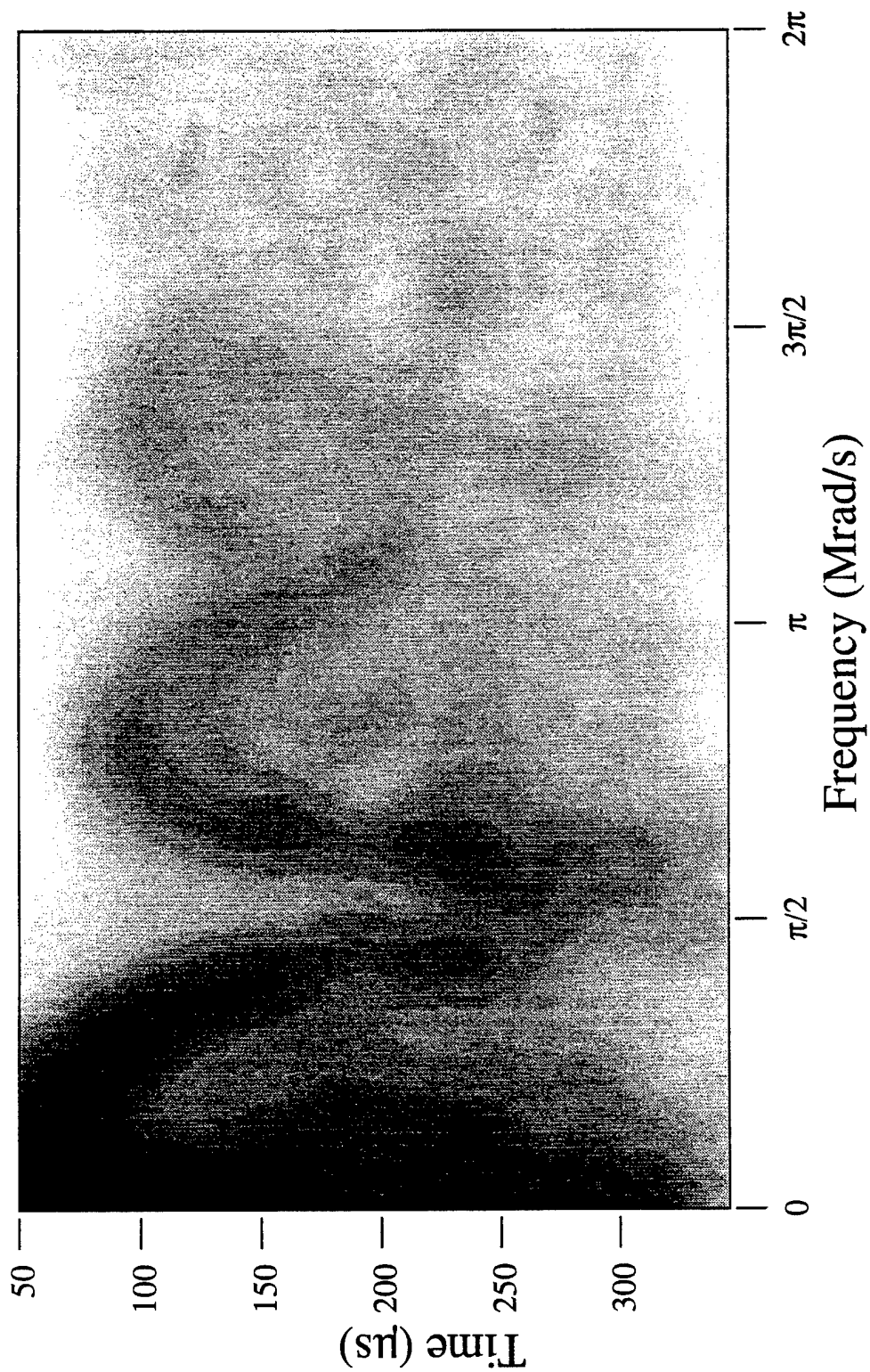Figure C-8.   The sum of the total variation in both directions (real).

Figure C-9.   The sum of the total variation in both directions (imaginary).

DISTRIBUTION LIST

DSWA-TR-95-7

DEPARTMENT OF DEFENSE

DEFENSE INTELLIGENCE AGENCY
    ATTN: DIW-4

DEFENSE SPECIAL WEAPONS AGENCY
  2 CY ATTN: ISST
    ATTN: E TREMBA
    ATTN: P SENSENY
    ATTN: WE
    ATTN: WEL
    ATTN: D PYLE
    ATTN: K KIM
    ATTN: G ULLRICH

DEFENSE TECHNICAL INFORMATION CENTER
  2 CY ATTN: DTIC/OCP

FIELD COMMAND DEFENSE SPECIAL WEAPONS AGENCY
    ATTN: E RINEHART
    ATTN: G S LU
    ATTN: FCTO
    ATTN: DR BALADI
    ATTN: G GOODFELLOW
    ATTN: P RANDLES

DEPARTMENT OF THE ARMY

U S ARMY COLD REGION RES & ENG LAB
    ATTN: CECRL-MAILROOM

U S ARMY ENGR WATERWAYS EXPER STATION
    ATTN: C WELCH
  5 CY ATTN: HOWARD WHITE
    ATTN: TECHNICAL LIBRARY

U S ARMY RESEARCH LAB
    ATTN: TECH LIB

DEPARTMENT OF THE NAVY

DAVID TAYLOR RESEARCH CENTER
    ATTN: CODE 1770

DEPARTMENT OF THE AIR FORCE

AIR FORCE ARMAMENT LABORATORY
    ATTN: A BRINSON
    ATTN: D WATTS

AIR UNIVERSITY LIBRARY
    ATTN: AUL-LSE

HQ 497 IG/INOT
    ATTN: INT

PHILLIPS LABORATORY
    ATTN: EDWARD TAYLOR

DEPARTMENT OF ENERGY

LAWRENCE LIVERMORE NATIONAL LAB
    ATTN: ALLEN KUHL

LOS ALAMOS NATIONAL LABORATORY
    ATTN: J OGLE

SANDIA NATIONAL LABORATORIES
    ATTN: DR PAUL COOPER
    ATTN: RPTS RECEIVING CLRK

OTHER GOVERNMENT

CENTRAL INTELLIGENCE AGENCY
    ATTN: OSWR/NED

DEPARTMENT OF THE INTERIOR
    ATTN: D RODDY

FEDERAL EMERGENCY MANAGEMENT AGENCY
    ATTN: OFC OF CIVIL DEFENSE

DEPARTMENT OF DEFENSE CONTRACTORS

AEROTHERM CORP
    ATTN: J SAPERSTEIN

APPLIED RESEARCH ASSOCIATES
    ATTN: R FLORY

APPLIED RESEARCH ASSOCIATES INC
    ATTN: J KEEFER
    ATTN: N ETHRIDGE

APPLIED RESEARCH ASSOCIATES INC
    ATTN: C J HIGGINS
    ATTN: F E SEUSY
    ATTN: N BAUM

APPLIED RESEARCH ASSOCIATES INC
    ATTN: J SHINN

APPLIED RESEARCH ASSOCIATES INC
    ATTN: R FRANK

APPLIED RESEARCH ASSOCIATES INC
    ATTN: J L DRAKE

BDM FEDERAL INC
    ATTN: E DORCHAK

BOEING TECHNICAL & MANAGEMENT SVCS INC
    ATTN: ROBERT M SCHMIDT

CARPENTER RESEARCH CORP
    ATTN: H J CARPENTER

FLUID PHYSICS IND
    ATTN: R TRACI

GEO CENTERS INC
 ATTN: B NELSON

IIT RESEARCH INSTITUTE
 ATTN: DOCUMENTS LIBRARY

JAYCOR
 ATTN: J STUHMILLER

JAYCOR
 ATTN: CYRUS P KNOWLES

KAMAN SCIENCES CORP
 ATTN: D BRYCE

KAMAN SCIENCES CORPORATION
 ATTN: DASIAC

LOGICON R & D ASSOCIATES
2 CY ATTN: C K B LEE
 ATTN: D SIMONS
2 CY ATTN: K MANN
 ATTN: LIBRARY
2 CY ATTN: R CRAWFORD

LOGICON R & D ASSOCIATES
 ATTN: D CARLSON

LOGICON R & D ASSOCIATES
 ATTN: G GANONG
 ATTN: J RENICK

MAXWELL LABORATORIES INC
 ATTN: C PETERSEN
 ATTN: K D PYATT, JR
 ATTN: P COLEMAN
 ATTN: S PEYTON

MAXWELL LABORATORIES INC
 ATTN: C NEEDHAM

PACIFIC-SIERRA RESEARCH CORP
 ATTN: H BRODE

SCIENCE APPLICATIONS INTL CORP
 ATTN: C HSIAO
 ATTN: G EGGUM
 ATTN: H WILSON
 ATTN: J DISHON
 ATTN: TECHNICAL REPORT SYSTEM

SCIENCE APPLICATIONS INTL CORP
 ATTN: W LAYSON

SCIENCE APPLICATIONS INTL CORP
 ATTN: G BINNINGER

SRI INTERNATIONAL
 ATTN: A FLORENCE
 ATTN: DR JIM GRAN
 ATTN: J SIMONS
 ATTN: M SANAI
 ATTN: MARK GROETHE
 ATTN: P DE CARLI

SUNBURST RECOVERY INC
 ATTN: C YOUNG

TECH REPS INC
 ATTN: F MCMULLAN

THE AEROSPACE CORP
 ATTN: LIBRARY ACQUISITION

TITAN CORPORATION
 ATTN: J ROCCO
 ATTN: J THOMSEN
 ATTN: S BABCOCK

TITAN CORPORATION (THE)
 ATTN: R ENGLAND

TRW INC
 ATTN: T.I.C.

TRW SPACE & DEFENSE SECTOR SPACE
 ATTN: W WAMPLER

WASHINGTON STATE UNIVERSITY
2 CY ATTN: PROF. Y GUPTA

WEIDLINGER ASSOC INC
 ATTN: H LEVINE

WEIDLINGER ASSOCIATES INC
 ATTN: T DEEVY

WEIDLINGER ASSOCIATES INC
 ATTN: M BARON